# EXTRACTION OF COASTAL OCEAN WAVE CHARACTERISTIC PARAMETERS USING OPTICAL REMOTE SENSING AND COMPUTER VISION TECHNOLOGIES

MICHAEL JOHNSON (BSC HONOURS
GEOINFORMATICS)

Research document submitted in fulfilment of the requirements for the degree of

Master of Science (in Geoinformatics) at Stellenbosch University.
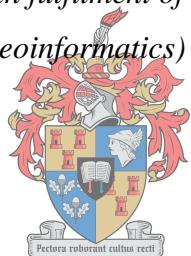
SUPERVISOR: DR M LÜCK-VOGEL

MARCH 2018

DEPARTMENT OF GEOGRAPHY AND ENVIRONMENTAL STUDIES

DECLARATION

By submitting this report electronically, I declare that the entirety of the work contained therein is my own, original work, that I am the sole author thereof (save to the extent explicitly otherwise stated), that reproduction and publication thereof by Stellenbosch University will not infringe any third party rights and that I have not previously in its entirety or in part submitted it for obtaining any qualification.

March 2018

ABSTRACT

Ocean waves are among the most important forces shaping the world's coastlines. They drive environmental processes and human activity that occurs within the coastal zone as well as on the open ocean. The assessment of wave characteristics, such as wave direction, wavelength, wave period and wave velocity, are critical in understanding coastal processes that serve as a baseline for better coastal management. However, the monitoring and assessment of wave characteristics is challenging, given the high complexity of ocean dynamics and large spatial extent. While globally the development of ocean state forecasting models has been fruitful in recent decades, these capabilities are only just being developed in (South) Africa and require ground truth data for model development and validation.

The work presented here assesses whether optical imagery from the RapidEye satellite can be used to extract ocean wave characteristic parameters such as wave direction, wavelength, wave period and wave velocity for the purpose of further developing and validating wave forecasting models. Two techniques were adopted. The first made use of a Fourier transform to extract the directional wave spectrum. The characteristic wave parameters were then calculated from the spectrum. The second approach made use of normalised cross correlation (NCC) to extract the phase velocity field. The techniques identified and developed were tested using RapidEye imagery on four study areas on the South African coast. These included Richards Bay, Durban, East London and Cape Point. Ground truth data in the form of wave measurements captured by wave buoys were used for validating the results.

The results from the Fourier transform show a generally high agreement with the directional spectra derived from the wave buoys. In the context of characteristic parameters extracted from these spectra, two of the four study sites produced highly accurate results with all parameters within 10% deviation of the wave buoy data. The results obtained from the NCC revealed that the shoaling of ocean waves has a positive influence on the reliability of measurements near the shoreline. The directions for two of the study areas had differences of less than 10° from the wave buoy directions. It was also observed that when waves are present with vastly different directions the NCC approach fails.

These results show a promising advance in the use of optical imagery for the monitoring and assessment of near-shore wave conditions. However, it is recommended that further development and validation of these techniques be undertaken before operationalization.

KEYWORDS

Coastal, Ocean Waves, Direction, Period, Wavelength, Phase Velocity, RapidEye, Fourier Transform, Normalized Cross Correlation.

OPSOMMING

Oseaangolwe is een van die belangrikste kragte wat die wêreld se kuslyne vorm. Hulle bepaal omgewingsprosesse en menslike aktiwiteite wat binne die kussone, asook in die oop see omgewing, plaasvind. Die evaluering van golfeienskappe, soos golfrigting, golflengte, golfperiode en golfsnelheid, is van kritieke belang om kusprosesse te verstaan as 'n basis vir beter kusbestuur. Monitering en assessering van golfkenmerke is egter uitdagend, gegewe die hoë kompleksiteit van die oseane-dinamika asook die groot ruimtelike omvang. Terwyl die ontwikkeling van modelle vir oseaanstaatvooruitsigte in die afgelope dekades wêreldwyd baie suksesvol gebruik word, word hierdie vermoëns nou eers in (Suid) Afrika ontwikkel en daarom word grondwaarheidsdata vir modelontwikkeling en -verifikasie benodig.

Die werk wat hier aangebied word, beoordeel of optiese beelde van die RapidEye-satelliet gebruik kan word om golfeienskappe soos golfrigting, -lengte, -periode en -snelheid te onttrek ten einde golfvoorspellingsmodelle verder te ontwikkel en te verifieer. Twee tegnieke is ondersoek. Die eerste het gebruik gemaak van 'n Fourier transform om die golfrigtingsspektrum te onttrek. Die kenmerkende golfparameters is dan uit die spektrum bereken. Die tweede benadering het gebruik gemaak van genormaliseerde kruis korrelasie om die fase snelheids veld te onttrek. Hierdie tegnieke wat geïdentifiseer en ontwikkel is, is getoets met behulp van RapidEye-beelde op vier studieareas aan die Suid-Afrikaanse kus. Dit sluit in Richardsbaai, Durban, Oos-Londen en Kaap Punt. Grondwaarheidsdata van golfmetings wat deur golfboeie vasgevang is, is vir die verifiering van die resultate gebruik.

Die resultate van die Fourier transform toon 'n algemeen hoë ooreenkoms met die rigtingspektra wat van die golfboeie verkry is. In die konteks van kenmerkende parameters wat uit hierdie spektra onttrek is, het twee van die vier studiegebiede hoogs akkurate resultate met alle parameters binne 10% afwyking opgelewer. Die resultate wat verkry is uit die genormaliseerde kruis korrelasie het getoon dat wrywing van die oseaangolwe met die seebodem die betroubaarheid van metings naby die kuslyn laat toeneem. Die rigtings vir twee van die studiegebiede het met minder as 10° van die golfboeirigtings verskil. Dit is ook waargeneem dat hierdie benadering meer geneig om te misluk wanneer golwe teen baie verskillende rigtings teenwoordig is.

Hierdie resultate is belowend vir die gebruik van optiese beelde vir die monitering van golftoestand assessering naby die kus. Daar word egter aanbeveel dat verdere ontwikkeling en verifiering van hierdie tegnieke onderneem word voor operasionalisering onderneem word.

TREFWOORDE

Kuslyn, Oseaangolwe, Rigting, Periode, Golflengte, Fase Snelheid, RapidEye-satelliet, Fourier Transform, Genormaliseerde Kruis Korrelasie.

ACKNOWLEDGEMENTS

I would like to express my sincere appreciation to the following people and institutions who made the completion of this thesis possible:

- My supervisor, Dr Melanie Lück-Vogel for her tremendous contribution – always available to offer her input, guidance and advice;

- The South African National Research Foundation (NRF), for providing funding for this research;

- Wave data supplied by the CSIR, Stellenbosch, which was collected on behalf of the Transnet National Port Authority (TNPA);

- The Council for Industrial and Scientific Research (CSIR) for office space and use of their facilities;

- My parents, for their love, motivation and financial support – without them the study would not have been possible;

- Emma Phillips for her love and continuous support throughout the process of researching and writing this thesis;

- Fellow office mate and masters student, James Burns for his constant encouragement and advice;

- Kirodh Boodhraj for his assistance and help with MATLAB;

- My fellow masters students and friends for always being there to offer support and motivation;

- God, for granting me the strength and knowledge to complete this study.

CONTENTS

TABLES

FIGURES

ACRONYMS AND ABBREVIATIONS

2D	Two-dimensional
CCD	Charge-coupled device
CIAS	Correlation image analysis software
CSIR	Council for Scientific and Industrial Research
CSV	Comma-separated values
DFT	Discrete Fourier transform
DSP	Developer studio project
FFT	Fast Fourier transform
IDL	Interactive data language
IGFR	International Geomagnetic Reference Field
KZN	KwaZulu-Natal
NCC	Normalised cross correlation
NCC-O	Normalised cross-correlation orientation
NIR	Near infrared
OCIMS	Oceans and Coasts Information Management System
Radar	Radio detection and ranging
SAR	Synthetic aperture radar
SSH	Sea surface height
STAR	Center for Satellite Applications and Research
SWIR	Short-wave infrared
TIFF	Tagged image file format
VOS	Voluntary observing ships

SYMBOLS

A	Amplitude (m)
c	Phase velocity (m/s)
E	Energy (J/m^2)
$E(f)$	Frequency spectrum
$E(f,\theta)$	Directional Spectrum
f	Frequency (Hz)
g	Gravitational acceleration (9.8 m/s^2)
k	Wavenumber (1/m)
k_x, k_y	X and Y wavenumber components (1/m)
h	Water depth (m)
H	Wave height (m)
$\bar{H}$	Mean wave height (m)
H_{m_0}	Significant wave height estimated from the wave spectrum (m)
H_s	Significant wave height (m)
$H_{1/3}$	Significant wave height estimated from the wave record (m)
H_v	Significant wave height estimated from visual observations (m)
m_0	Total variance integrated over all frequencies (m^2)
T	Wave period (s)
$\bar{T}_0$	Mean zero-crossing wave period (s)
T_p	Peak spectral period (s)
T_s	Significant wave period (s)
$T_{1/3}$	Significant wave period estimated from the wave record (s)
T_v	Significant wave period estimated from visual observations (s)
λ	Wavelength (m)
λ_p	Peak spectral wavelength (m)
η	Surface elevation (m)
θ_p	Peak spectral wave direction (°)
ρ	Mass density of seawater (1030 kg/m^3)
σ^2	Variance of surface elevation (m^2)
ω	Angular frequency (rad/s)

CHAPTER 1:   INTRODUCTION

The coastal zone occurs at the interface of three major natural systems – the atmosphere, the ocean and the land surface. Continuous interactions between these systems make for an extremely dynamic and complex environment. The driving factors behind many of these interactions include surface winds and ocean waves.

It has been estimated that a large portion of the world's population (40-60%) is concentrated along the coast. This number is constantly on the rise due to the aesthetic appeal and economic opportunities associated with coastal spaces. This results in an increase in population density and associated socio-economic activities within the coastal zone, subsequently exposing more people to the ocean and the impacts of ocean waves. Increasing pressure for coastal development has led to the encroachment of human activities on the natural coastal environment. This, coupled with on-going climate change, results in a loss of coastal functioning, with progressive susceptibility to coastal hazards such as coastal erosion, flooding and sea level rise (Beatley 2009). Coastal authorities, therefore, face the increasingly difficult task of balancing development and managing coastal risks (Marchand 2010).

The avoidance of coastal hazards through better planning is ultimately the most effective and sensible approach to managing future development (Beatley 2009). Detailed, accurate and real time knowledge of near-shore ocean wave conditions has been identified as a pressing need for the development and improvement of current practical and theoretical models. Furthermore, this information is essential for coastal decision making and planning, and would aid in the development of a comprehensive coastal zone management plan. However, collecting such information is challenging given the high complexity of ocean dynamics and large spatial extent. In addition, there is often little funding and manpower available for the task (Luck-Vogel 2016). Currently for the entire length of the South African coastline (2789 km), there are only seven permanent wave buoys deployed to record near-shore ocean wave conditions (WaveNet 2016). The wave buoys provide point data at their predetermined locations and hence do not record more complex, non-uniform coastal waves. This results in a generalised spatial understanding of the highly dynamic near-shore wave conditions, which is not suitable to inform near-shore coastal management.

In recent decades, the development of numerical wave prediction models has been productive, resulting in an increase in the reliability of wave forecasts over the open ocean (Collard, Ardhuin & Chapron 2005a). This was made possible by advancements in wind forecasting and remote sensing of surface winds over the ocean, as well as the inclusions of wave height measurements from space-borne altimeters and wave buoys (Janssen 2004). These models also have their limitations, resulting from the poor availability of spectral wave measurements that could be used to validate choices in model parameterizations (Stopa et al. 2016). In particular, long-period waves that are unrelated to local winds (i.e. swell) are poorly predicted (Rogers, Hwang & Wang 2003). In-situ data are also required to validate the model results. Therefore, near-shore wave observations will not only provide insight into the physical understanding of the complex interactions that take place at the coastal zone interface, but will also have direct applications for driving and validating numerical wave prediction models.

Satellite data and remote sensing technologies hold potential to overcome the limitations associated with buoy data and numerical wave prediction models. Sea surface remote sensing techniques are rapidly being developed worldwide. Scatterometry for the measurement of surface winds, and altimetry for the measurement of offshore sea surface and wave heights, are now well established techniques resulting in recognised operational applications (one such example being the Center for Satellite Applications and Research (STAR) web portal for real time measurements (https://manati.star.nesdis.noaa.gov/datasets/ASCATData.php)). Synthetic Aperture Radar (SAR) measurements (Beal, Tilley & Monaldo 1983; Ardhuin, Collard & Chapron 2004; Collard, Ardhuin & Chapron 2005a) as well as airborne optical imagery (Stillwell 1969; Dugan, Piotrowski & Williams 2001; Gelpi, Schuraytz & Husman 2001) have been demonstrated to hold potential for the extraction of spectral wave information. However, each of these techniques have limitations. Altimetry is restricted to offshore height measurements and thus cannot provide any direct observations of the near-shore wave conditions. SAR measurements are generally limited to very long waves (Collard, Ardhuin & Chapron 2005a) and therefore the capability to extract the directional wave field usually breaks down in near-shore environments, due to the shortening of the wavelength as waves approach shallower water (Johannessen 2000). Airborne optical imagery is limited by low coverage and high cost per unit of ground covered.

Owing to such observations, it has been identified that a technology that delivers spatially continuous data and has the capability to provide wave spectral information in the near-shore environment is required.

1.1   PROBLEM STATEMENT

Globally, human populations and activities are concentrated within the coastal zone. The coastal zone is an extremely dynamic and complex region that constantly evolves over time and space in response to a wide variety of drivers and pressures. Climate change effects such as sea level rise and increased storm frequency and intensity are increasingly putting pressure on growing human population, infrastructure and livelihoods. Furthermore, developments encroaching on the coast weaken the natural environment's buffer function against coastal flooding and erosion.

Protection of the coast and adaptation for climate change requires better understanding and forecasting capabilities of ocean wave characteristics and their impact on coastal processes (such as erosion). However, the ability of such wave forecasting systems depends on ground truth data for model development and calibration. Such data currently only exist in the form of a few isolated wave buoys scattered around the South African coastline. Given the high variability of the South African coast, and the position of the wave buoys, the data are often insufficient to represent local wave patterns closer to the coast.

In order to further develop reliable ocean forecast models (e.g. for the National Oceans and Coasts Information Management System (OCIMS)), it is desirable to have a more extensive and complete coverage of wave observation data as reference and for calibration.

An intense review of current literature revealed that research, based on the use of airborne optical imagery for the assessment of ocean wave characteristic parameters, has been published (Cox & Munk 1954; Gelpi, Schuraytz & Husman 2001). In these studies a modulation transfer function was used to extract a directional wave spectrum. However in comparison the use of optical satellite imagery has experienced limited development. The only publications that could be found included the extraction of wave spectra from Sentinel-2 imagery (Kudrysytsev et al. 2017) and the calculation of a phase velocity field from a single-date SPOT-5 image (De Michele et al. 2012). In comparison to the Sentinel-2 and SPOT-5 sensors, the RapidEye sensor has both a high spatial and temporal resolution. However to

date, there have been no publications on wave characteristics based on the use of the RapidEye sensor.

1.2   RESEARCH QUESTION

Can characteristic wave parameters such as wave frequency, direction and velocity be extracted from multispectral high resolution RapidEye satellite imagery using remote sensing and computer vision technologies?

1.3   AIM

The aim of this work is to evaluate the use of RapidEye multispectral satellite imagery for the spatially continuous determination of near-shore ocean wave characteristic parameters, such as wave direction, wavelength, wave period and wave velocity using remote sensing and computer vision technologies.

1.4   OBJECTIVES

To achieve the research aim, the following objectives have been set:

1. Review literature on techniques used to extract ocean wave characteristic parameters from satellite imagery;
2. Acquire and preprocess the satellite imagery and reference wave buoy data;
3. Extract characteristic wave parameters from RapidEye satellite imagery;
4. Assess the effectiveness of the techniques used for extracting ocean wave characteristic parameters in each study area; and
5. Interpret findings and make recommendations.

1.5   RESEARCH METHODOLOGY AND RESEARCH DESIGN

The research presented in this thesis can be contextualised as a methodological study. Such studies are aimed at developing new methods or validating new instruments through a pilot study (Mouton 2004). In this case, two methodologies for the extraction of characteristic parameters from RapidEye satellite imagery are developed and evaluated. Neither of these methodologies have been used for this purpose on RapidEye imagery and this is the first time that these two methodologies will be applied together in a study in order to gain a more comprehensive description of near-shore waves. The evaluation of this research makes this both a quantitative and qualitative study. Quantitative in the sense that statistical measures are used to validate the derived characteristic wave parameters with wave buoy data, and

5

qualitative in the sense that a visually descriptive comparison is made of the directional wave spectra.

The research design and layout of the report and associated chapters are shown below in Figure 1.1.
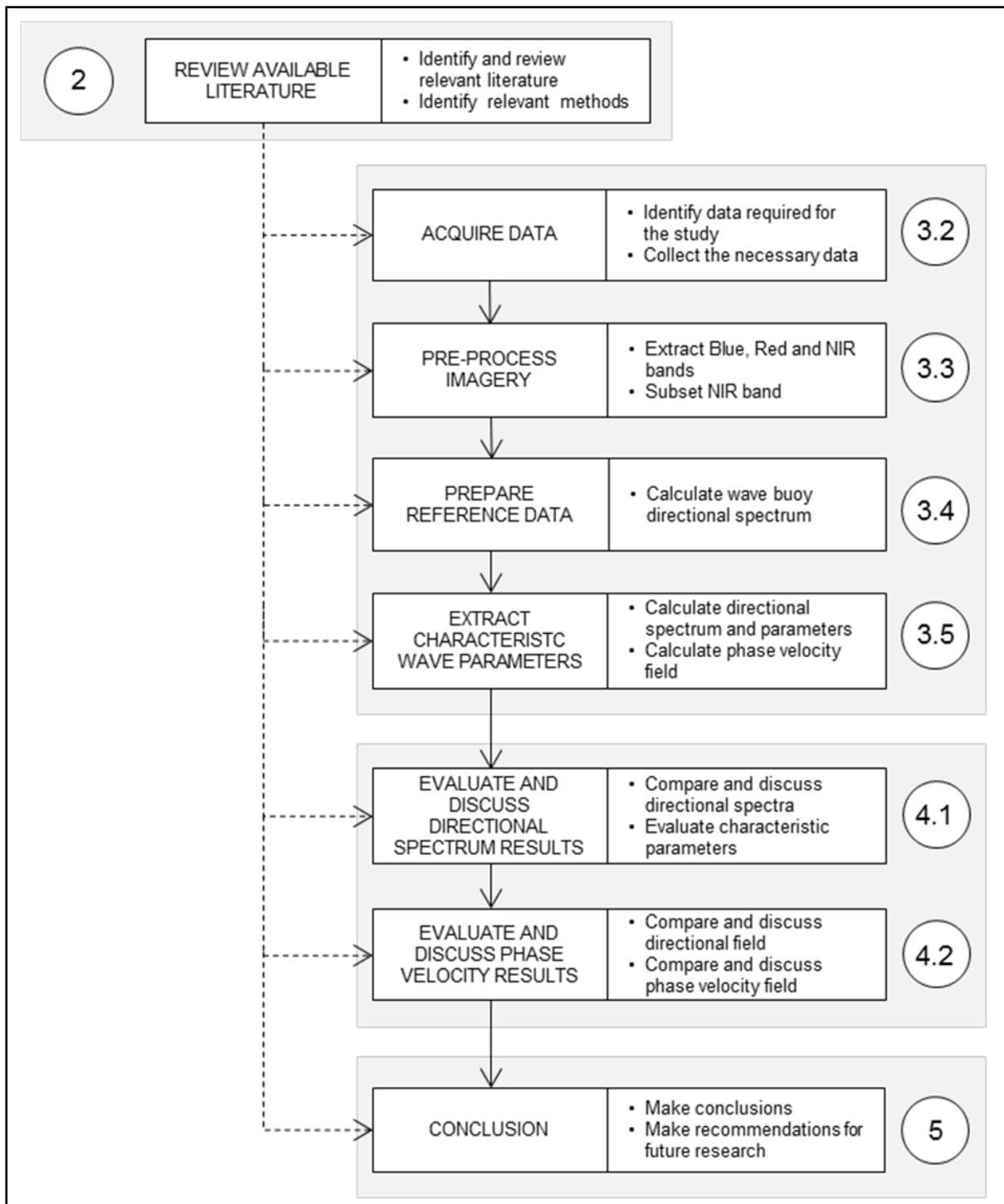
Figure 1.1 Simplified research design and report structure of the thesis. Numbers in the circles refer to the respective section numbers.

1.6   THESIS STRUCTURE

This work is organised into five chapters: Introduction, Theory, Research Methods and Materials, Results and Discussion, and Conclusions. Chapter 1, provides the background to coastal ocean waves, as well as the rationale, aim and objectives of this research. Chapter 2, provides a literature review on the broad theoretical base of coastal ocean waves, a discussion on current remote sensing approaches for the observation and extraction of near-shore ocean wave characteristic parameters and summarises key concepts and algorithms used in this research. Chapter 3, details the data used and specifically outlines the methods applied in this research. Chapter 4, presents the results achieved, as well as a discussion of the results and accuracies thereof, while Chapter 5, summarises the key findings of this research, identifies the current limitations and provides recommendations for future research.

CHAPTER 2:   THEORY

Ocean waves play a vital role in transporting energy around the globe and shaping the world's coastlines. Within the coastal zone, wind-generated waves are the most important suppliers of energy (Davidson-Arnott 2010) and have a direct impact on human activities within the coastal zone. These activities include transportation, fishing, recreation, resource extraction (i.e. gas, oil, etc.) and potential energy extraction through tidal and wave power plants.

Waves have a major physical impact on the shoreline and are responsible for generating near-shore surf zone currents. The angle at which the waves approach the shoreline as well as the type of wave itself, result in the formation of littoral currents and affect major coast shaping forces such as coastal erosion, sediment transportation and sediment deposition (Tinley 1985). These, in combination with wave action, flooding and storm surges, pose a threat to coastal development and human occupancy in the coastal zone (Smith et al. 2013).

Wave dynamics influence the design of ships and coastal structures. They also provide important information about the sea floor topography in shallow water, as the bathymetry directly affects the propagation patterns of waves (Piotrowski & Dugan 2002; Danilo & Melgani 2016).

There is, therefore, the need to collect wave data and use such to support decision making in coastal management and planning. Sundar (2016) has reported the diverse applications of wave data and how these can be used as effective tools in oceanographic and engineering fields. Such applications include:

- Offshore and coastal structure design, site selection criteria, ship design, ship operations and transportation studies, environmental impact assessments, ocean numerical modelling and search-and-rescue;
- Coastal hydrodynamics and sediment movement studies, vessel navigation, harbour surging, recreation and marine facility designs;
- The testing and verification of wave forecasting and hindcasting models; and
- Studies involving the estimation of wave energy potential in different coastal and offshore regions.

2.1 OCEAN WAVES

Waves are disturbances that transfer energy through, or across the surface of, a medium (Brown et al. 2005). While waves have the ability to move over long distances, the movement of the medium through which the wave propagates is limited. They start when matter is disturbed (i.e. there is an initial input of energy). The energy produced propagates in the same direction as the wave. Such energy will cause the wave to travel through the medium until all its energy is transferred. Waves that travel along the ocean surface are referred to as surface waves (Brown et al. 2005). Ocean waves can be generated from several sources and all consist of a crest (the highest point on the wave) and a trough (the lowest point on the wave).

The simplest way to represent a surface wave is to use a sinusoidal function (Bosboom & Stive 2013), known as the linear wave theory (Figure 2.1). These functions represent the regular variation of the water surface at a certain location.
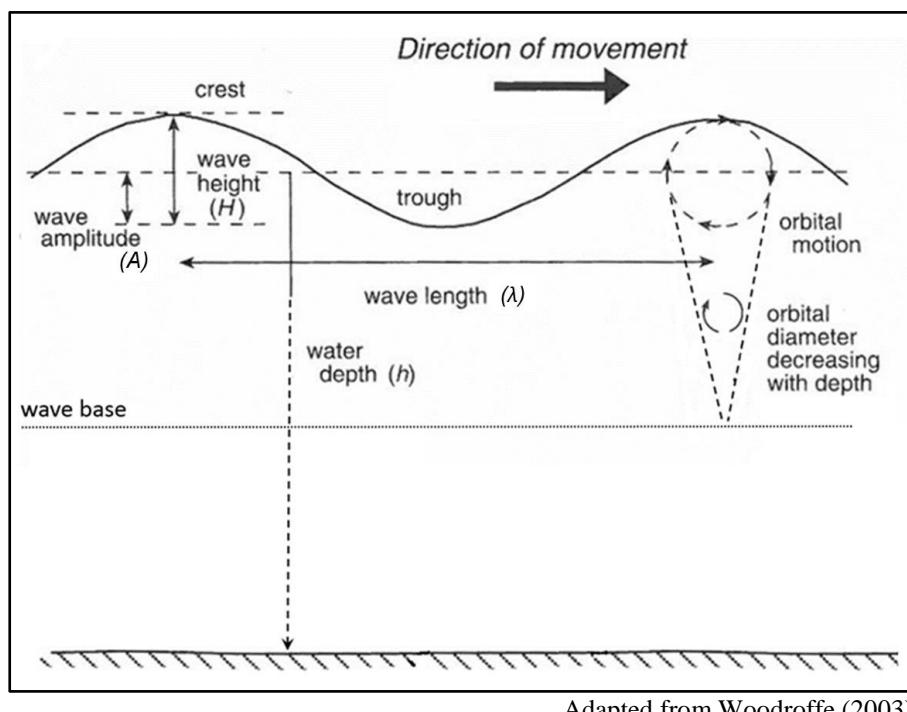
Adapted from Woodroffe (2003)

Figure 2.1 Vertical profile of idealised (sinusoidal) ocean waves.

The vertical distance between a crest and an adjacent trough is known as the wave height (H); which is twice the wave amplitude (A).

Wavelength (λ) is the horizontal distance between two successive wave crests (or wave troughs). The wavenumber (k) is the spatial frequency of the wave (i.e. the number of waves that exist over a specified distance) and is measured in cycles or radians per unit distance. A

complete cycle of a wave is considered to have an 'angular displacement' of 2π radians. The wavenumber can therefore be associated with wavelength ($k = 2\pi/\lambda$).

Wave period (T) is the time it takes for one wavelength to pass a fixed point (i.e. the time interval between the start and end of a single wave) and is measured in seconds (s). Wave frequency (f) is the inverse of wave period and is measured in cycles per second or Hertz (Hz). Additionally, there is a parameter known as the angular frequency (ω), which is measured as the number of cycles or radians per unit time. The angular frequency is thus related to frequency ($\omega = 2\pi f = 2\pi/T$).

Wave phase velocity (c) is the distance travelled by a given point on a wave (e.g. a crest) in a given period of time ($c = \lambda/T = \omega/k$) and is measured in metres per second (m/s). The ratio between the wave height and wavelength (H/λ) is referred to as the wave steepness.

Wave direction is the direction from which the wave originates (e.g. a wave moving from south to north is referred to as a southerly wave). Wave direction is not limited to a single propagation direction. The most common direction should be calculated and is referred to as the 'peak direction'. This is represented in degrees from true north.

Wave propagation is simply the movement of a waveform, and not of water mass (Bosboom & Stive 2013). There is very little net forward motion of water molecules during the passage of the wave. As the waves pass through, the water molecules complete an orbital motion (Figure 2.1). With increasing depth beneath the water surface, the size of the orbits decreases. By a depth of half the wavelength, the orbits are too small to do any significant work. This depth is referred to as the wave base (Gabler et al. 2009).

2.1.1   Wind generated waves

Ocean waves come in various shapes and sizes, ranging from a fraction of a centimetre to half the circumference of the earth. Ocean waves can be classified based on the disturbing force, which generates the wave, and their wavelength (or equivalently wave period or frequency) as seen in Figure 2.2 (Holthuijesen 2007).
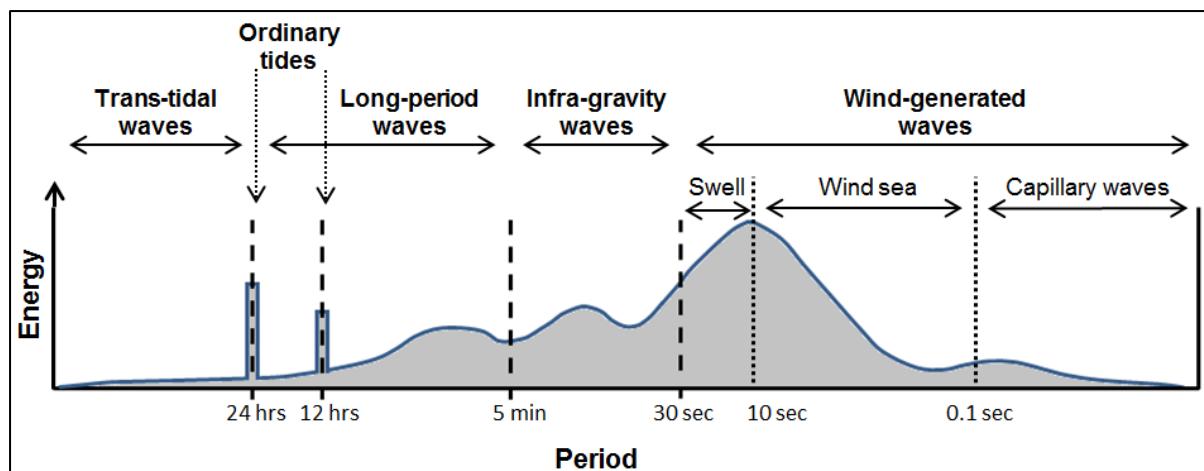
Adapted from Holthuijesen (2007)

Figure 2.2 Schematic energy spectrum of oceanic variability, showing approximate relative energy levels as a function of wave period.

An 'incident wave' is a term used to describe a wave that reaches the shore. Incident waves are the main supplier of energy to the coastal system (Bosboom & Stive 2013) and are generally made up of a combination of wind sea and swell (Woodroffe 2003). Such waves have a period of less than 30 seconds and are generated by the wind. These incident waves will be the main focus of this research.

Incident waves observed at the coast do not conform to the simple sinusoidal (ideal) form seen in Figure 2.1. This is due to a number of reasons (Woodroffe 2003). First, as waves approach the shore, they undergo significant transformations due to interactions with the seafloor. Second, incident waves are rarely generated from a single storm or wind event and even when they are generated from a single storm, the wave train stills contain a variety of waves with different wavelengths and wave heights. Thirdly, as waves travel, their character changes due to interferences with waves originating from different areas and waves of different sizes.

Waves that have similar frequencies combine to give an irregular surface. When waves of similar frequencies combine they can either add up or cancel each other out. This property is referred to as superposition. When two waves are in phase with one another, the wave height increases. This is referred to as constructive interference. When the waves are out of phase their combined height decreases, resulting in destructive interference. This results in variations in water-level, occurring at infragravity frequencies, known wave groups (Figure 2.3). This phenomenon can often be observed in the surf zone, where it is referred to as surf beat.
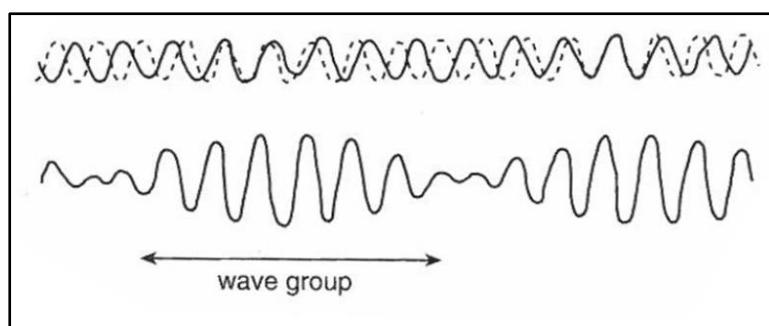
Source: Woodroffe (2003)

Figure 2.3 The superposition of two wave trains to form wave groups.

During generation, local winds cause irregular and short crested waves, known as wind waves (Holthuijesen 2007). The height of these wind waves depends on the strength of the winds, the fetch (which is the distance that the wind blows over the sea) and the time duration of the wind (Woodroffe 2003). An increase in any of these factors will cause an increase in wave height. When these factors are significantly high, the sea reaches a fully developed state. At this point, the energy received by the wind is equal to the energy dissipated by the waves.

When waves travel out of the generation area or if the wind dies down, the waves become more orderly as they sort themselves into groups of similar wave speed and wavelength. These more orderly waves are known as swell, and it is these waves that arrive at the coastline, even in the absence of coastal winds (Gabler et al. 2009). In the generation area there is a broad spectrum of wave periods, ranging from 0.1 to 15 seconds or larger (Figure 2.4A). Over short distances, the smaller waves disappear as they group together to form larger waves (Woodroffe 2003). Thus, swell waves (Figure 2.4C) show a smaller range of periods than a full developed sea (Figure 2.4B). The wave velocity and period are related to the wavelength (the larger the wave, the faster it travels). The further swell waves travel across the ocean, the more time there is for the smaller waves to be absorbed (Woodroffe 2003). Therefore, by the time these waves reach the shore, the spectrum of wave periods is relatively small (Figure 2.4D).
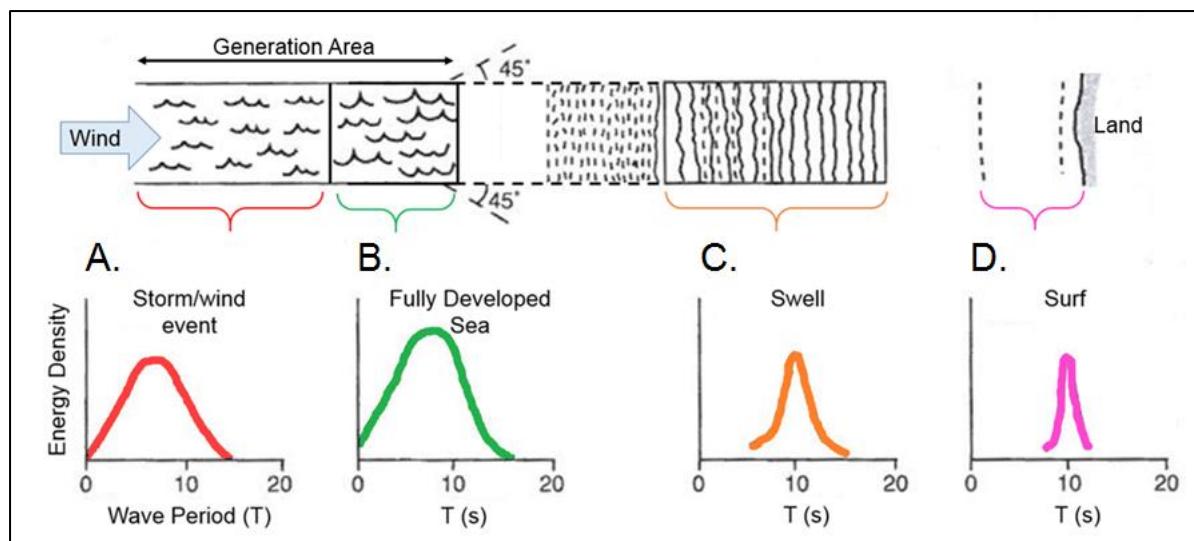
Adapted from Woodroffe (2003)

Figure 2.4 The transformation of ocean waves from the generation area to the coastline.

As waves travel, they lose little energy, due to friction and the spreading of the wave crest caused by the curvature of the Earth. However, they are a very efficient means of transporting energy (Gabler et al. 2009). As the wave group travels, the wavelength and wave period are generally maintained, but wave height may decrease slightly. Waves propagate in a radial direction from the point of generation. Ninety percent of the energy is contained within a 45 degree angle of the generation area. In deep water, the velocity at which the wave group travels, known as the group velocity, is half the speed of the individual waves, known as phase velocity (Woodroffe 2003).

2.1.2   Near-shore wave transformations

As waves approach the shore, and move into shallow water, they are transformed as they interact with the seafloor and other physical objects. These transformations result in the complex spatial patterns associated with near-shore waves. The way in which these waves are transformed can be described by shoaling, refraction, reflection and diffraction.

2.1.2.1   Shoaling

When waves enter water that is shallower than the wave base, they start to interact with the seafloor. Friction causes a decrease in wave velocity and wavelength (i.e. causing the waves to 'bunch' together). In order to maintain a constant energy flux, the wave height increases (Bosboom & Stive 2013). This process is known as shoaling and is illustrated in Figure 2.5.
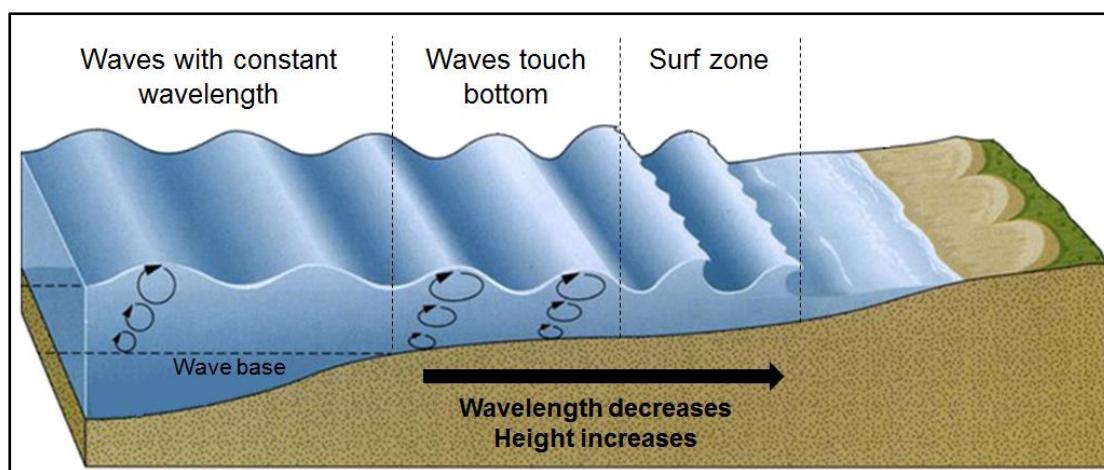
Figure 2.5 Cross section of shoaling waves in the near-shore environment.

As the wave height increases and the wavelength decreases, the wave steepness (H/λ) increases. At a wave steepness value of 1/7, the wave will become unstable and start to break (Bosboom & Stive 2013). In doing so, the energy which was originally obtained in the generation area, is dispersed.

2.1.2.2   Refraction

Wave refraction is the bending of waves as they approach the shore as illustrated in Figure 2.6 (Bosboom & Stive 2013). Offshore waves may approach from directly offshore or at an angle to the trend of the coastline; however, they change direction relative to the coastline as they enter shallow water. Consider an 'angular' wave approaching a beach that has straight and parallel seafloor depth contours. Wave refraction occurs when part of a wave reaches shallow water before the rest of the wave. The part of the wave that enters shallow water first slows down due to friction with the seafloor, while the other parts of the wave will continue at their speed in deep water. The net result of the deceleration of the wave front causes the wave front to bend, thereby converting the wave front from a straight line to a curve that increasingly resembles the shape of the shoreline as it approaches land (Gabler et al. 2009).
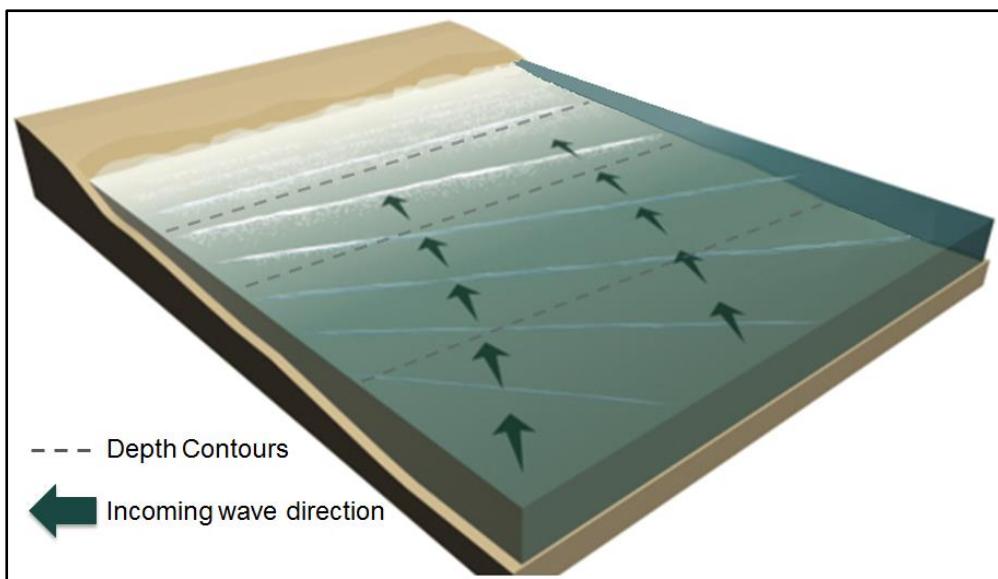
Figure 2.6 Waves refracting as they approach the shore.

2.1.2.3   Reflection

When an ocean wave strikes a barrier such as a seawall, breakwater or even a coastal cliff face, the wave energy can be partially absorbed depending on the type of material (i.e. if the material in porous or resilient). The energy that is not absorbed is reflected (McCormick 2007). When the barrier is vertical, flat, smooth and impermeable, all the incident wave energy is reflected. When an incoming crest crosses a reflected crest or an incoming trough crosses a reflected trough, constructive interference occurs and the wave height increases. When an incident crest crosses a reflected trough, destructive interference occurs as they cancel each other, thus resulting in a decrease in wave height.

2.1.2.4   Diffraction

If obstructions to the wave propagation (e.g. offshore island, breakwater or headland) are present, there is a large initial variation in the wave energy and propagation pattern along the wave crests (Bosboom & Stive 2013). Diffraction is the process that describes the passage of wave energy into calm water, referred to as shadow zones, on the leeward side of wave obstructing obstacles (Bosboom & Stive 2013). Figure 2.7 illustrates the diffraction of an ocean wave as it comes into contact with a headland. Part of the wave front is reflected seaward. The remainder of the wave front clears the barrier and becomes circular in the shadow zone and appears to radiate from the end point of the headland.
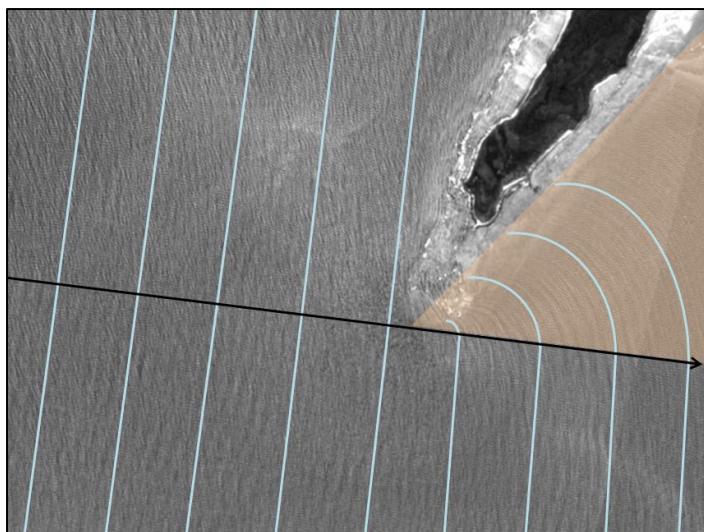
Source: Own design

Figure 2.7 Wave diffraction of an incident wave train.

2.2   MEASUREMENT OF OCEAN WAVES

Routine measurements for the monitoring of near-shore ocean waves have only become available in the past 20-30 years. The first wave buoy in South Africa was installed in July 1969 off the coast of Mossel Bay (WaveNet 2016). Although there are currently seven wave buoys along the South African coast, the number is still much smaller than, for example, gauging stations on rivers. In recent years, there have been advances in remote sensing approaches to ocean wave measurements, thus providing a much larger spatial coverage.

2.2.1   Time scales

When measuring and describing waves in the coastal environment, it is important to consider the spatial and temporal scales that are relevant to the particular application. There are four spatio-temporal scales that should be considered (Holthuijesen 2007).

Small-scale measurements deal with the description of a few wave periods or wavelengths. At this scale, it is possible to describe the motion of water surface, the velocity of the water particles and the wave induced pressures. These measurements have resolutions of a small fraction of the wavelength or period of the waves being observed. An example of this scale is Figure 2.1.

Medium scale measurements are those in the order of a hundred to several hundred wave periods or wavelengths. This relates to the measurement on the temporal scale of a few minutes to about half an hour. The equivalent on a spatial scale is in the order of a few kilometres, which is short enough for conditions to be considered homogenous and long

enough to provide reliable statistical results. This is the reason why data from wave measuring instruments such as wave buoys, are often broken into 30 minute parcels. At this scale, one can characterise statistic properties of waves and can therefore compare these to similar recordings at different locations or at the same location at different times. Statistical properties can be calculated for characteristics such as wave height or wave period for all the waves measured during the interval. Similarly, one can examine the wave spectrum, which depicts the amount of energy associated with each frequency during the interval considered.

Large scales are those covering time intervals of tens of hours or spatial distances of several hundred to a few thousand kilometres. At this scale, the spatial or temporal variability of the wave spectrum can be described. Such scale would be considered if one were interested in tracking waves across large distances, such as from the generation areas, across oceans, to the shore.

The final scale is that of a number of years. At these scales, long-term average wave conditions can be calculated. Measurements at these scales are important for the prediction of the effect of wave processes on coastal evolution as well as the generation of a wave climate and the monitoring of long-term changes.

2.2.2   Instrumentation

The first wave data were collected by the voluntary observing ships (VOS) program. The VOS program was set up to train crew members on board VOS to make weather observations while at sea by visually estimating and reporting wave height, wave period and wave direction. However, this form of manual ocean wave observation presented many limitations. For example, ships avoid heavy seas and storm conditions; therefore, such conditions would seldom be recorded or represented in the statistics of wave observations. Furthermore, observations are always subjective which can lead to the under- or overestimation of the true wave conditions (Holthuijesen 2007).

To avoid the problems associated with visual observations, measurements taken with in-situ wave observation instruments are generally preferred. Such instruments include wave buoys, wave poles, pressure transducers, inverted echo-sounders and current meters (Figure 2.8).
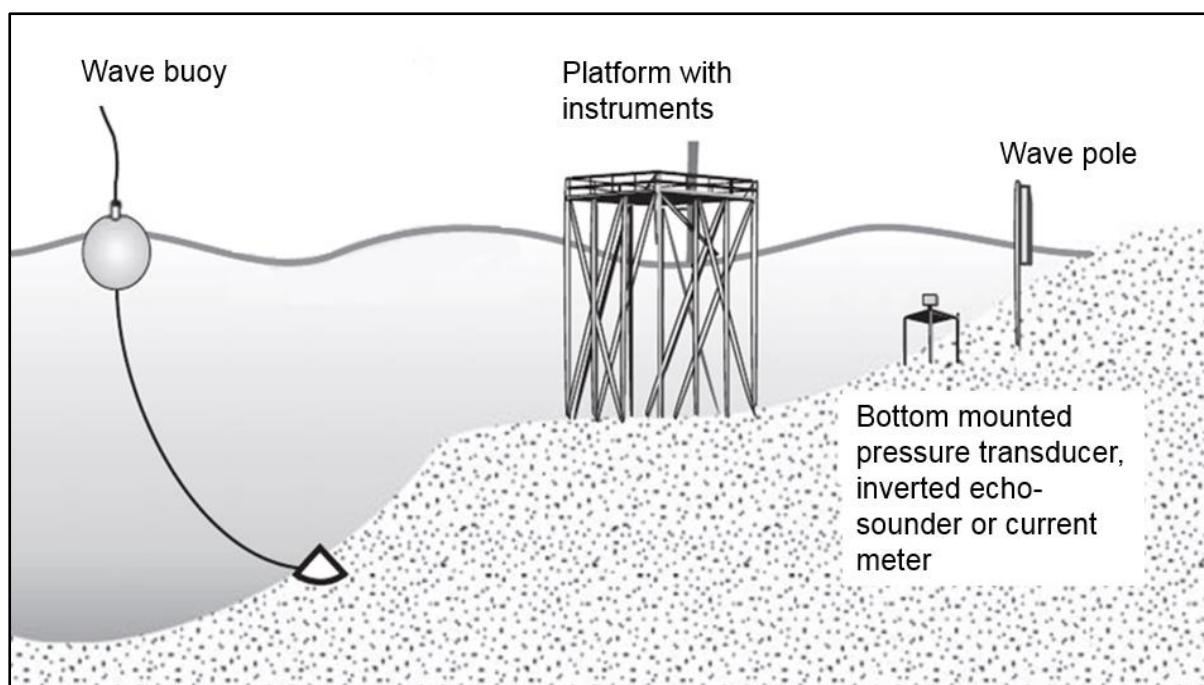
Adapted from Davidson-Arnott (2010)

Figure 2.8 In-situ wave observation instruments.

However, these instruments have limitations as well (Holthuijesen 2007). First, there are limitations associated with the basic principle of the instrument (e.g. a weather buoy may swerve around or capsize in heavy seas). Second, instruments are impacted by processes in the marine environment. These include mechanical impacts, marine fouling and corrosion. Third, the data collected by such instruments is point data, which means it only provides information for waves at a distinct location. Often such data are not representative over large areas.

2.2.3   Analysis of wave records

A wave record (Figure 2.9) is a record of water-level variation captured by measurement instrumentation. Real ocean waves do not conform to a simple sinusoidal shape (as described in Section 2.1.1). Therefore, wave records have complex patterns consisting of a range of superimposed components of wave periods, heights and directions (Reeve, Chadwick & Fleming 2004). Although wave records seem erratic, if one describes short-term variations (i.e. a wave record spanning a short period of time) statistically by using average parameters, it appears that the statistics can be considered stationary (i.e. the wave statistics remain constant for the duration of the wave record). On the other hand, a record should also be long enough to produce reliable averages. A commonly used recording period of ocean waves is 15-30 minutes (Bosboom & Stive 2013).
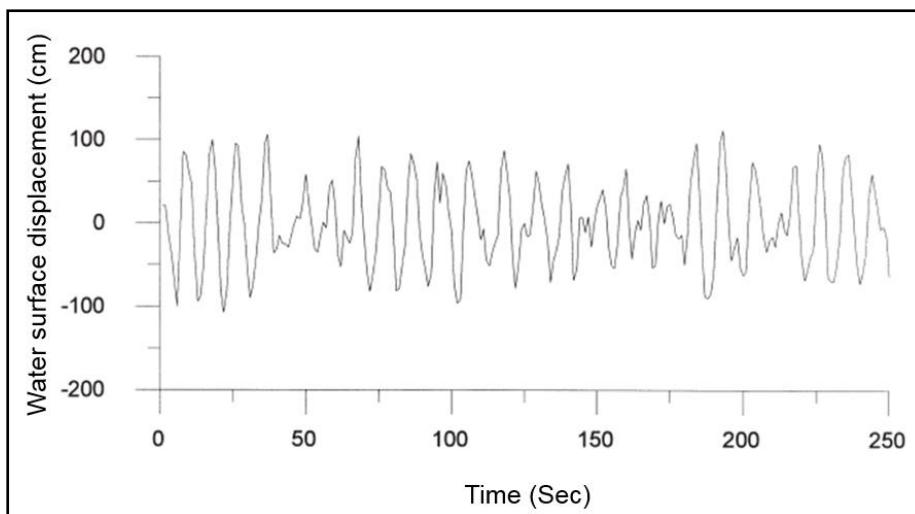
<div align="right">Source: Kuo, Leu & Kao (1999)</div>

Figure 2.9 Example of a wave record.

Wave records can be analysed via two different techniques in terms of short-term statistics. The first approach is a wave-by-wave analysis and the second approach is a spectral analysis.

2.2.3.1   Wave-by-wave analysis

When the short-term record is considered as a series of individual waves with their own wave height and period, statistical parameters based on the measurement of all waves can be used to characterise the record. This is known as wave-by-wave analysis.

In the context of a wave record, surface elevation, $\eta(t)$, is the term used to describe the instantaneous elevation of the sea surface (i.e. at any one moment in time) relative to some reference level. A wave is defined as the profile of the surface elevation between two successive downward zero-crossings or two successive upward-zero crossings of the elevation as illustrated in Figure 2.10. Wave height and period for a wave record are defined with respect to zero-crossings, where zero is equal to the mean of surface elevations. In this context, a wave is defined as having a crest that lies above the zero surface elevation and a trough that lies below it.
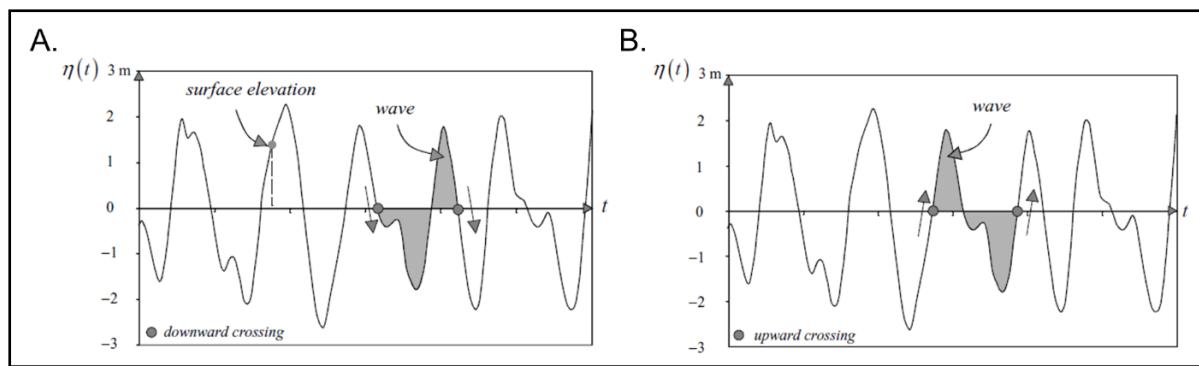
Figure 2.10 A) Downward zero-crossing and B) Upward zero-crossing. The shaded area represents one wave.

Although the height and length properties of the individual waves in the record will differ depending on the type of zero-crossing used, the statistics will remain the same upon analysing the whole record (Holthuijesen 2007).

By analysing a wave record it is possible to calculate a number of statistics that represent the characteristics of the wave height (H) and period (T) (Holthuijesen 2007). The simplest statistics to derive are the mean wave height ($\bar{H}$) and mean zero-crossing wave period ($\bar{T}_0$).

Wave energy is proportional to the square of the wave height; therefore, larger waves often have the greatest significance (Holthuijesen 2007). There are a number of definitions for wave height and period. The most frequently used are the significant wave height (H_s) and significant wave period (T_s) (Holthuijesen 2007). In terms of the wave record, the significant wave height (H_s) is defined as the mean of the highest one-third of the waves and is calculated using the following equation:

$$H_{1/3} = \frac{1}{N/3} \sum_{j=1}^{N/3} H_j \qquad \text{Equation 2.1}$$

where $H_{1/3}$ is the significant wave height;

              N is the number of waves in the wave record;

              H is the wave height; and

              j is the rank number of the wave, based on wave height (i.e. 1 would be the highest wave, 2 would be the second highest wave etc.

Similarly, the significant wave period is defined as the mean period of the highest one-third of the waves in the record:

$$T_{1/3} = \frac{1}{N/3} \sum_{j=1}^{N/3} T_{0,j}$$

Equation 2.2

where $T_{1/3}$ is the significant wave period;

              N is the number of waves in the wave record;

              T_0 is the zero-crossing wave period; and

              j is the rank number of the wave, based on zero-crossing wave period.

Visual estimates of wave height tend to focus on the largest waves in a series and the height derived from them. This is also termed the significant wave height but denoted as H_v. The visually estimated period associated with these waves is termed the significant wave period and denoted as T_v.

2.2.3.2 Spectral analysis

Ocean waves, which at first can appear very random, can be analysed on the assumption that they consist of a collection of simple sinusoidal wave components with different frequencies, amplitudes and directions as illustrated in Figure 2.11 (Goda 2000). The spectral analysis method determines the distribution of wave energy and average statistics for each wave frequency by converting the wave record into a wave spectrum (U.S. Army Corps of Engineers 2008). A wave spectrum is the distribution of energy plotted against frequency and direction. When the wave energy distribution is expressed as a function of the frequency alone, it is known as the frequency spectrum ($E(f)$). When expressed as a function of both frequency and direction, it is termed the directional wave spectrum ($E(f, \theta)$) (Goda 2000). The conversion of the wave record to the wave spectrum is achieved through the use of the Fourier transform (U.S. Army Corps of Engineers 2008).
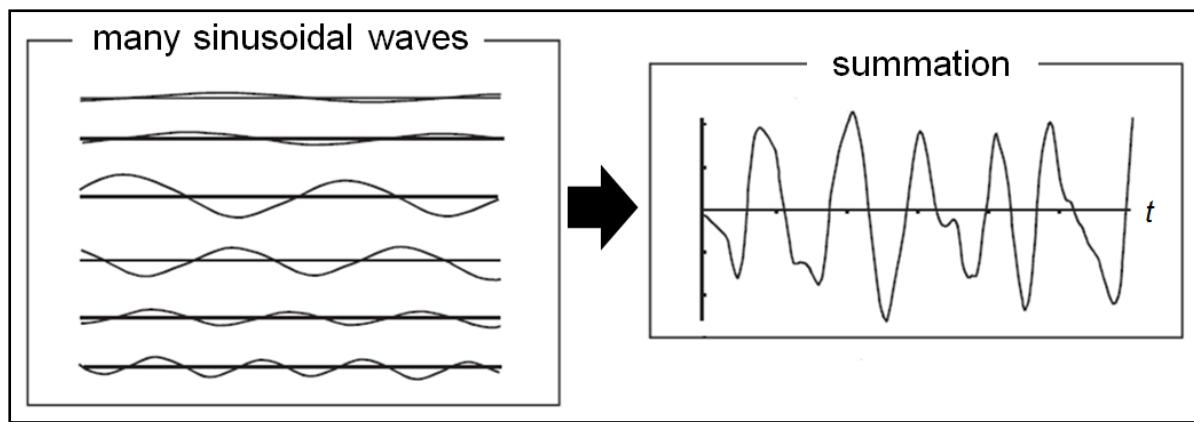
Source: Holthuijesen (2007)

Figure 2.11 The summation of many sinusoidal waves creates a random sea surface.

Fourier theory is based on the transformation of data from the spatio-temporal domain to the frequency domain which allows for the subsequent extraction of component frequencies from sinusoidal signals. The functional forms within the Fourier theory are continuous. A Fourier transform transforms a spatio-temporal domain signal of infinite duration into a continuous spectrum composed of an infinite number of sinusoids (Kulkarni 2002). However, ocean waves are discretely sampled by wave observation instruments, usually at constant intervals and of finite duration. For such data, only a finite number of sinusoids are required. Therefore, a discretised form of the Fourier transform is used to computationally process the data (Kulkarni 2002). This form is known as a Discrete Fourier Transform (DFT) and can be computed using the fast Fourier transform algorithm (FFT). Figure 2.12A illustrates a simple sinusoidal signal, with a single frequency. Once analysed with a FFT, the result has a single peak at the frequency of the signal. Figure 2.12B illustrates a signal with two distinct peak frequencies as well random noise.
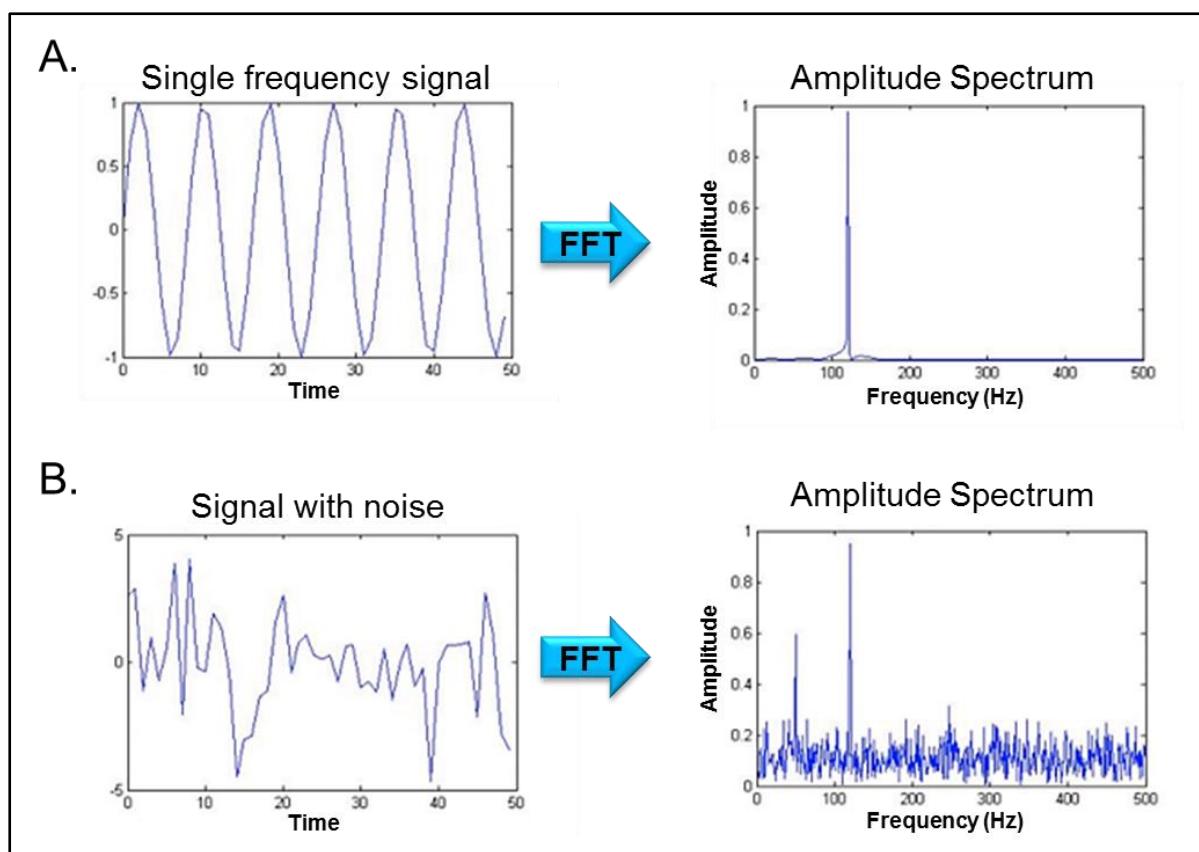
Adapted from MATLAB (2016b)

Figure 2.12 A) Fourier transform of a single frequency signal and B) Fourier transform of a double frequency signal with noise.

The amplitude (A) of the sinusoidal waves plotted against their frequencies is known as the amplitude spectrum (Figure 2.13A). Using trigonometry, it has been shown that the variance of a single sinusoidal wave is equal to $\frac{1}{2}A^2$. The variance for each sinusoidal wave can be calculated and plotted against frequency. This is known as the variance spectrum (Figure 2.13B). The amplitude and variance spectra are based on discrete frequencies; however, in reality, all frequencies are present at sea. Therefore, the variance is distributed over a frequency interval to calculate the variance density spectrum (Figure 2.13C). This spectrum provides the variance per unit frequency interval. The continuous variance density spectrum (Figure 2.13D) can then be obtained by having the width of such frequency interval approach zero (i.e. smoothing the spectrum) (Holthuijesen 2007).
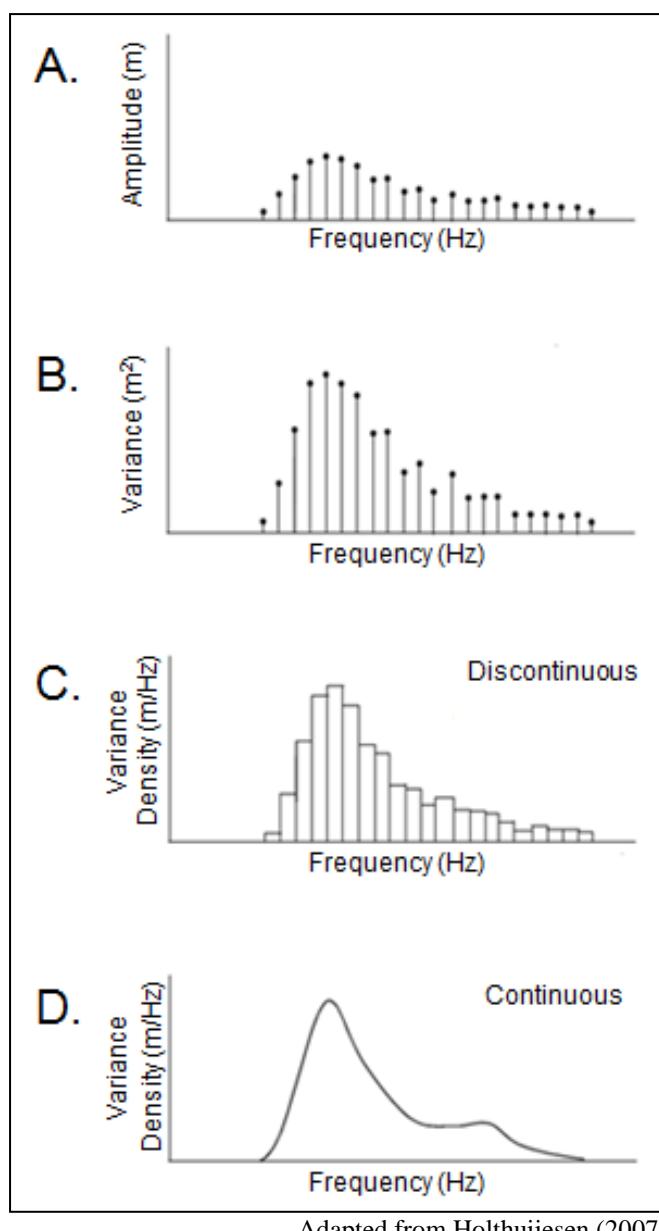
Adapted from Holthuijesen (2007)

Figure 2.13 A) Amplitude spectrum, B) Variance spectrum, C) Discontinuous variance density spectrum and D) Continuous variance density spectrum.

From the variance density spectrum, the energy density spectrum can be obtained as the variance and energy are related by the following equation:

$$E = \rho g \sigma^2$$

Equation 2.3

where E is the energy;

ρ is the mass density of sea water (1030 kg/m³);

g is the acceleration due to gravity (9.8 m/s²); and

σ^2 is the variance of surface elevation.

From the frequency spectrum, the dominant frequencies occurring in the wave record can be seen. The most energy occurs at the spectral peak. The wave period corresponding to the spectral peak is known as the peak spectral period (T_p) and is an important parameter for coastal engineering applications. The significant wave height can also be estimated from the wave spectrum using the following equation (Holthuijesen 2007):

$$H_{m_0} = 4\sqrt{m_0} \hspace{4cm} \text{Equation 2.4}$$

where H_{m_0} is the significant wave height estimated from the wave spectrum; and

           m_0 is the total variance integrated over all frequencies (i.e. the area under the spectrum).

The wave spectra described above are one-dimensional spectra. However, the sea state observed at any given location consists of component sinusoidal waves of various frequencies and amplitudes, approaching from different directions. Therefore, a complete description of the sea state needs to include all directional information. The directional spectrum is a way to describe this irregular and unpredictable surface.

Figure 2.14A represents a simple sinusoidal wave on a two dimensional surface. The wavelength, amplitude, phase and direction define the plane sinusoidal wave. Alternatively, this information can be plotted as seen in Figure 2.14B, where the distance from the centre represents the angular frequency and the direction from the centre indicates the direction from which the waves are coming. If plotted using the square of the amplitude as a third dimension, it would resemble the directional spectrum.
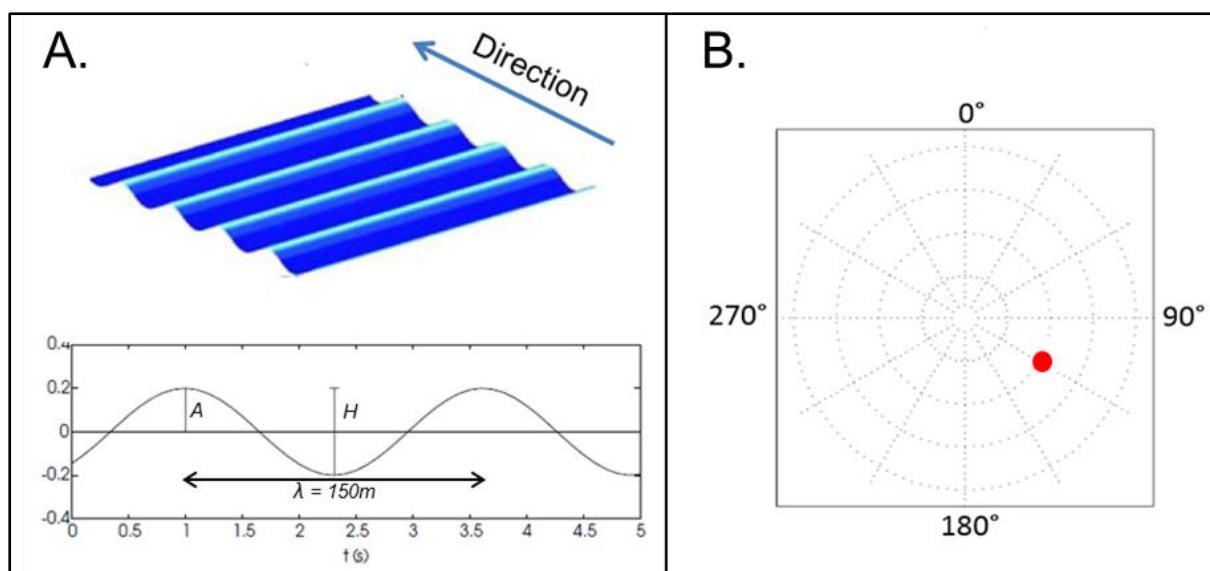
Figure 2.14 A) Sinusoidal wave propagating from a direction of 120° with a wavelength of 150 m. B) Directional spectrum of the single sinusoidal wave frequency (scale circles correspond to approximately 300 m, 150 m, 100 m and 50 m wavelengths).

In the directional spectrum, the variance density is a function of the frequency and direction, as seen in Figure 2.15. In this case, the wave is non-sinusoidal. The frequency scale circles correspond to approximately 300 m, 150 m, 100 m and 50 m wavelengths, as one moves away from the centre. From the directional spectrum, the peak direction, wavelength and period can be extracted.
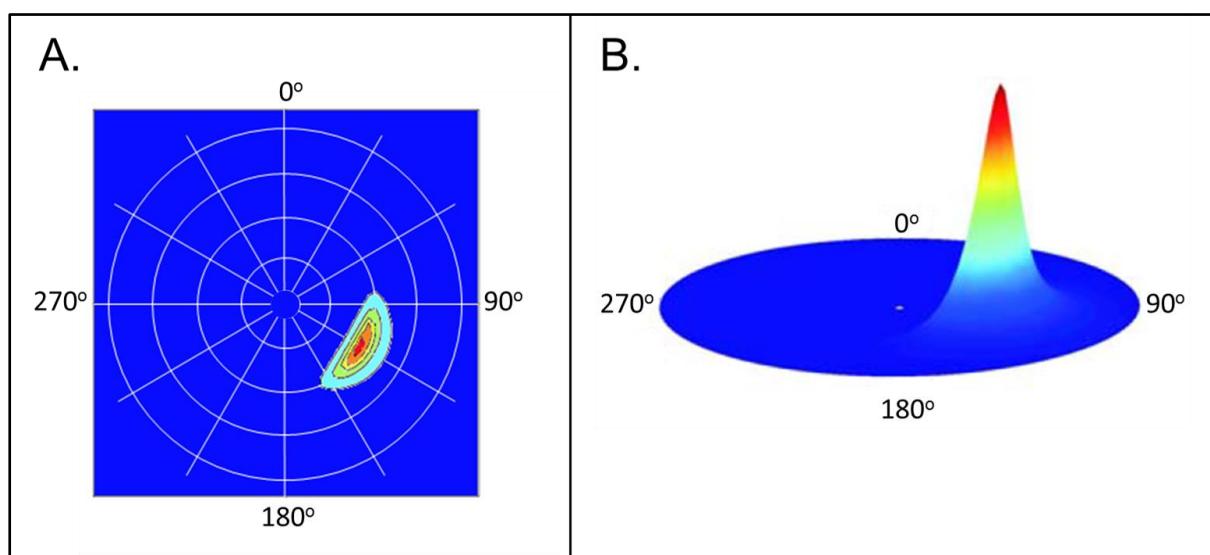
Figure 2.15 A) Directional wave spectrum of ocean waves propagating from a direction of 120°. B) Linear perspective of the directional wave spectrum viewed from the south.

2.3   REMOTE SENSING OF OCEAN WAVES

Remote sensing refers to the practice of acquiring information about the Earth's surface, without coming into contact with it. This is achieved by sensors mounted on overhead (aerial or space-borne) platforms that make use of electromagnetic radiation, in one or more regions of the electromagnetic spectrum, to capture images of the Earth's surface (Campbell 2007). Remotely-sensed data is acquired through the use of two main types of instruments, known as active and passive sensors. Both sensors measure energy reflected or emitted by objects on the Earth's surface. Active sensors emit energy towards an object, and measure the portion of energy that is reflected from the object back to the sensor, whereas passive sensors measure energy originating from sources other than the sensor, such as reflected sunlight (Campbell 2007).

Satellite-based remote sensing techniques offer a synoptic view of large areas of the ocean's surface, thus providing an opportunity for the observation of complex coastal waves over a large spatial extent nearly instantaneously or within a short period of time (Brown et al. 2005). Remote sensing techniques have been demonstrated to be complimentary to traditional in-situ approaches as they overcome a number of limitations associated with the collection of in-situ measurements (Brown et al. 2005; Collard, Ardhuin & Chapron 2005a; de Michele et al. 2012; Kudryavtsev et al. 2017).

2.3.1   Active remote sensing techniques

Active remote sensing techniques used for the observation and measurement of ocean waves include satellite radar altimetry and synthetic aperture radar (SAR). These techniques make use of radio detection and ranging (Radar) sensors operating in the microwave region of the electromagnetic spectrum. Radar sensors emit electromagnetic pulses, which interact with the Earth's surface, whereafter a portion of the pulse is backscattered to the sensor. As an active sensor, all information regarding the emitted pulse is known. Therefore, changes between the emitted and backscattered signal can be analysed. The strength of the backscattered signal is measured to discriminate between different targets. The time delay between the emitted and reflected signals determines the distance to the target. Two primary advantages of radars are that they can function during inclement weather and that they are independent of solar radiation (i.e. daylight).

2.3.1.1   Satellite Radar Altimetry

Satellite radar altimetry is an important remote sensing technique that can be used to directly assess along-track sea state parameters. Such parameters include sea surface height (SSH), wave height and wind speed (Fu & Cazenave 2001).

Satellite altimeters are non-imaging, nadir looking radar instruments that emit an electromagnetic pulse and measure the satellite-to-surface round trip as well as the amplitude and waveform of the returning pulse (Figure 2.16A). The satellite-to-surface round trip time can be used to calculate SSH. Changes in the shape and amplitude of the returning pulse, over time, can be used to measure the wave height (Brown et al. 2005). If the sea surface is flat, the return signals amplitude increases rapidly from the moment the signal's leading edge makes contact with the surface. If the sea surface is rough, the signal's leading edge would strike the crest of one wave and then a series of other crests which would cause the reflected signals amplitude to increase more gradually. Therefore, the slopes of the curves in the returning pulses are proportional to the wave height (Figure 2.16B).
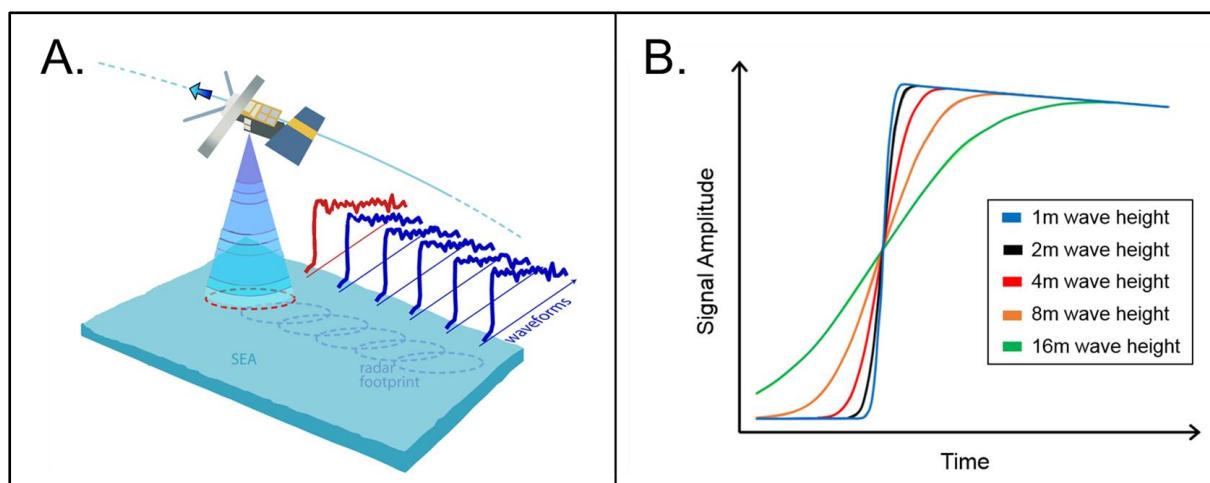
Adapted from ESA (2017) and ESA & CNES (2017)

Figure 2.16 A) Simplified representation of altimeter recording principle. B) Relationship between the wave height and slopes of the leading edge of the return pulses.

Although highly accurate (to within centimetres) (Brown et al. 2005), satellite altimeters only provide a distribution of elevations (i.e. wave and surface heights). These measurements do not resolve waves as no wave spectrum can be calculated. In addition, given the wide orbits and narrow swath width of the altimeter satellites, only isolated, along-track strips of the ocean are assessed. Furthermore in the near-shore environment, data retrieval and interpretation pose some specific difficulties due to the approximation of land (Vignudelli, Berry & Roblou 2008).

2.3.1.2   Synthetic Aperture Radar

SAR systems are imaging radars, mounted in a side-looking geometry (commonly between 15º and 60º), installed on a moving overhead platform (Figure 2.17). Such systems transmit microwave radiation towards the Earth's surface and record the amplitude and phase of the backscattered signal.
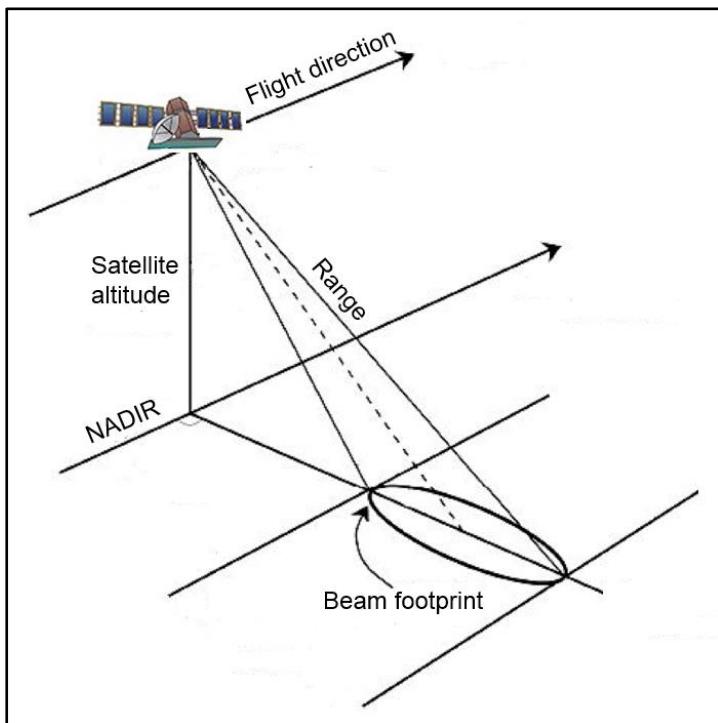
Source: Own Design

Figure 2.17 Simplified representation of the SAR imaging geometry.

A radar system with a synthetic aperture simulates a longer antenna length in order to increase the azimuth resolution. This is achieved by recording signal backscatter from observed objects over time. The movement of the satellite by some distance over the target, simulates a longer antenna. This overcomes the low resolution inherent with real aperture systems. Thus, SAR systems are unique in their capability to provide high resolution images.

SAR backscatter is influenced by a number of factors relating to the sensor type, imaging geometry and conditions on the Earth's surface. The most influential factors that affect backscatter include surface roughness, incidence angle, dielectric constant, wavelength, polarization and scattering mechanism. If the target is wet, the depth of penetration of the microwaves is low and in the case of salinity, the penetration depth is only a fraction of the microwaves wavelength (Gade 2015). Thus, SAR systems operating over the ocean provide information of the backscatter properties of the ocean surface roughness. Ocean surface

roughness is influenced by wind and waves, currents, surface slicks and is often different in the open ocean, as opposed to coastal areas.

At oblique incidence angles, the SAR backscatter arising from the ocean surface is caused by ocean surface waves in the order of the radar wavelength (Ager 2013). These ocean surface waves are modulated in their orientation, energy and motion by longer ocean waves. Thus, imaging of ocean waves using SAR can be described on the basis of a two-scale model: waves shorter than the pixel size and which contribute to the scattering mechanism, ride on a sea of much longer waves. SAR measurements are, therefore, limited to the recording of these longer waves (i.e. swell waves).

It has been demonstrated in a number of studies that under certain conditions, SAR systems can correctly evaluate the wavelengths, periods and directions of swell waves (Lyzenga 1987; Collard, Ardhuin & Chapron 2005a; Shao et al. 2016). However, waves moving along the line of sight are displaced from actual locations and require complex processing. Studies have also focused on the extraction of swell phase velocity (Chapron Collard & Kerbaol 2004; Chapron, Collard & Ardhuin 2005b; Johannessen et al. 2008). This was achieved through the analysis of the Doppler shift of radar echoes that occur during the synthetic aperture. However, this technique produces Doppler velocities at spatial resolutions of two kilometres for narrow swath SAR and hence does not yield spatially detailed information near the shore.

2.3.2 Passive remote sensing techniques

Passive sensors typically utilise the optical regions of the electromagnetic spectrum for imaging the Earth's surface. These include visible, near infrared (NIR) and short-wave infrared (SWIR) energy emitted or reflected from the Earth's surface.

Under favourable conditions for remote sensing (i.e. clear weather conditions with minimal cloud cover), optical sensors can capture fine contrast modulations on the ocean's surface. These modulations are caused by specular reflection of incident solar radiation on the multiple facets of the ocean surface and are known as sun glint. This allows for fine scale structures and patterns, such as those from ocean waves, to be delineated (Figure 2.18).
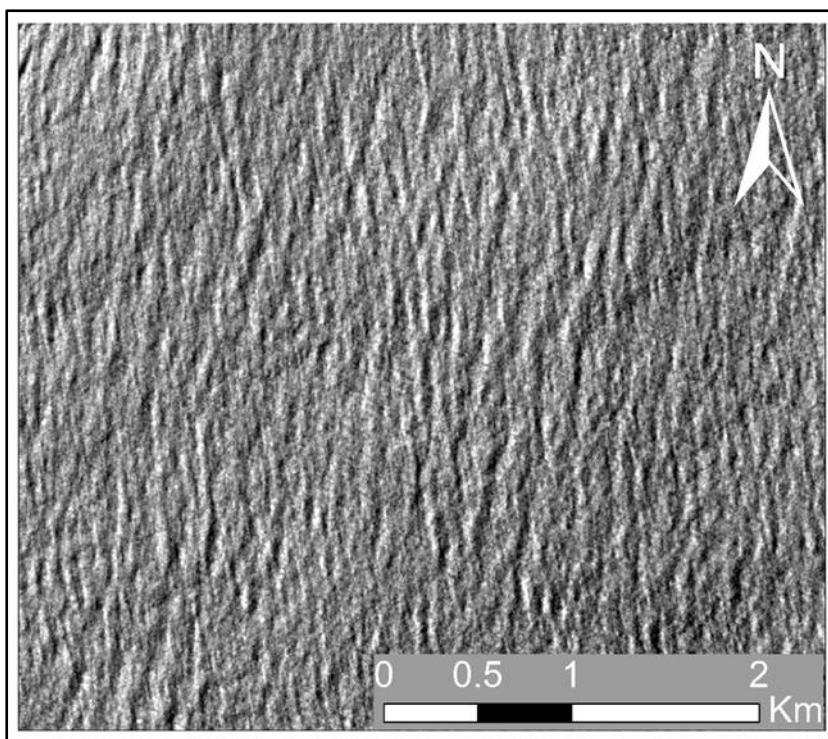
Figure 2.18 Sun glint modulations visible in a NIR RapidEye subset.

Sun glint modulations are the fundamental principal behind optical remote sensing of upper ocean dynamics. This has been exploited in a number of studies on non-linear internal waves (Apel et al. 1975; Jackson 2007), surface slicks (Hu et al. 2009; Kudryavtsev et al. 2012a) and ocean currents (Emery et al. 1986; Garcia & Robinson 1989; Crocker et al. 2007; Kudryavtsev et al. 2012b; Rascla et al. 2014).

Using airborne imagery, Cox & Munk (1954) were the first to demonstrate that sun glint modulations contained valuable information about the directional statistical properties of surface waves. Since then, a number of studies have demonstrated the potential of both airborne (Stilwell 1969; Dugan et al. 1996; Gelpi et al. 2001) and spaceborne (Populus et al. 1991; de Michele et al. 2012; Kudryavtsev et al. 2017) optical imaging systems for studying ocean waves.

Extraction of the directional spectrum from airborne imagery containing sun glint is achieved with a modulation transfer function (Cox & Munk 1954). Gelpi et al. (2001) extended the Cox and Munk (1954) model to define the transfer function and found a very good agreement between the directional wave spectra and in-situ measurements.

There has been limited development of techniques that use optical satellite imagery for studying ocean waves. Current publications include the extraction of wave spectra from Sentinel-2 imagery (Kudrysvetsev et al. 2017) and the extraction of a phase velocity field from a single-date SPOT-5 image (de Michele et al. 2012). To date, there are no applications based on the use of the RapidEye sensor for this purpose.

2.3.2.1 Wave Spectra

Kudrysvtsev et al. (2017) proposed a practical method for the retrieval and validation of the directional wave spectrum from multispectral Sentinel-2 imagery. The approach converted sun glint modulations into sea surface elevations to perform directional spectral analysis. This approach makes use a Fourier transform to derive the directional spectrum from the imagery.

Fourier theory (as explained in Section 2.2.3.2) states that any signal can be expressed as the sum of a number of sinusoidal signals (Lehar 2010). In the case of imagery, these are sinusoidal variations in brightness across the image. Brightness is used as a proxy for slope and aspect, at a given solar elevation and azimuth which are assumed constant over the entire image. Images can be captured in a Fourier term that encodes the spatial frequency, the magnitude and the phase. The spatial frequency is the frequency across which the brightness modulates, the magnitude corresponds to its contrast (i.e. the difference between the darkest and brightest pixel) and the phase represents how much the wave has shifted relative to the origin. In the frequency domain, pixel location is represented by its x- and y- spatial frequencies (wavenumber components) and its value is represented by amplitude.

An image is a two-dimensional (2D) array of pixel values and thus a 2D FFT must be used to transform the data to the frequency domain. The 2D FFT computes the DFT for each column followed by each row of pixels, and encodes all of the spatial frequencies present in the image that range between the zero and 'nyquist' frequencies (MATLAB 2016b).

The zero frequency corresponds to a 'DC term' that represents the average brightness across the image. A zero DC term would indicate that the average brightness across the image is zero, which would mean the sinusoid would alternate between positive and negative values in the brightness image. However, there is no such thing as negative reflectance. Hence all reflectance images have a positive DC term. The Nyquist frequency is the highest frequency that can be encoded in the image and is related to the spatial resolution (pixel size) of that image.

A signal that contains a single frequency is plotted as a single peak on the frequency axis. The location on the axis would correspond to the frequency of the signal and the value of its peak would correspond to the amplitude, or contrast of the signal (i.e. the higher the contrast in the image, the brighter the peaks will be in the Fourier image). For mathematical reasons, the Fourier transform plots the mirror of the peak across the origin (DC Term), resulting in two identical peaks (Figure 2.19).
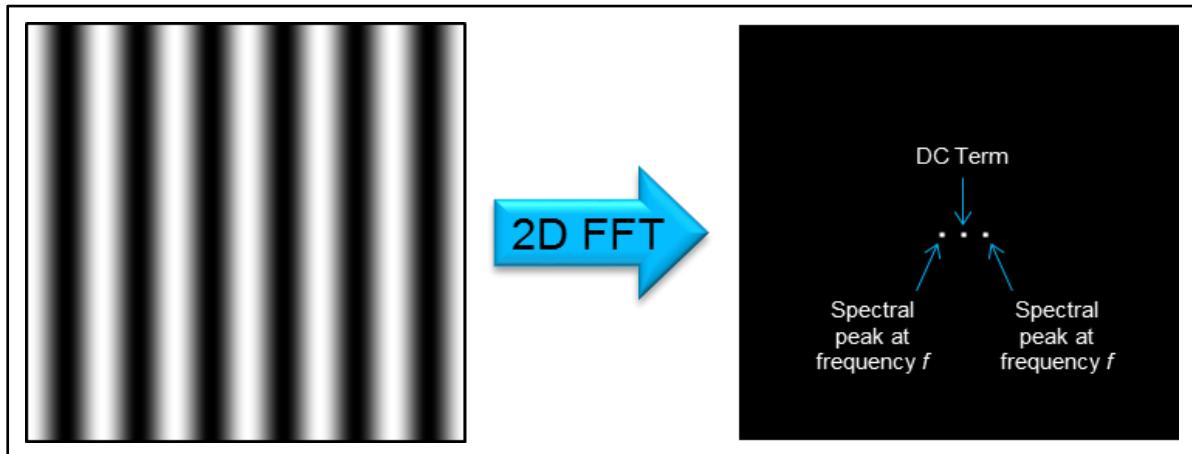
Adapted from Lehar (2010)

Figure 2.19 2D FFT of a single frequency sinusoidal frequency image illustrating the reflection of the spectral peak at frequency *f* across the origin (DC term).

Figure 2.20 illustrates the 2D FFT of four single frequency images. The higher the frequency signal, the further the peaks are plotted from the DC term. The angle of orientation is also plotted by the 2D FFT and is illustrated by Figure 2.20A to D.
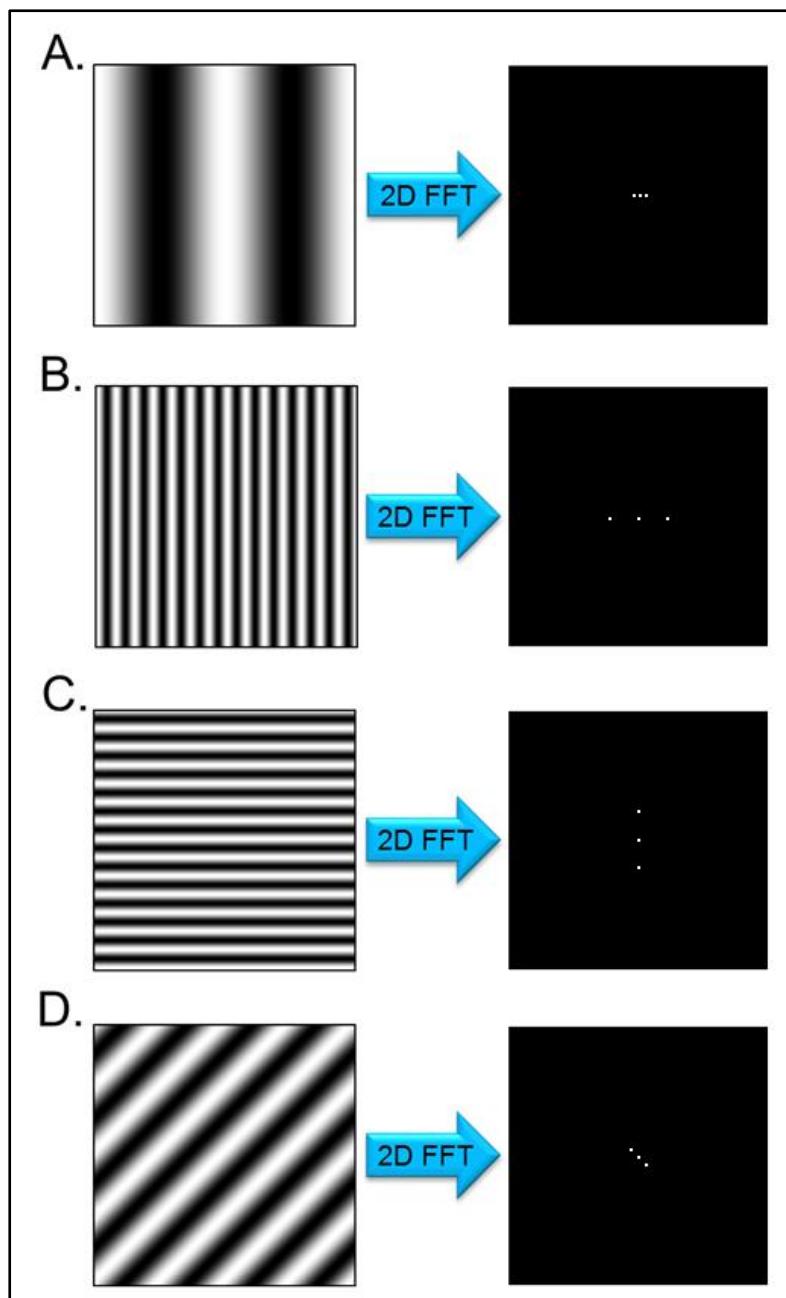
Adapted from Lehar (2010)

Figure 2.20 Four sinusoidal brightness images and their respective outputs after undergoing a 2D FFT.

2.3.2.2   Phase Velocity Field

De Michele et al. (2012) proposed an approach that uses the panchromatic and multispectral imagery of a single SPOT-5 dataset to directly measure the ocean surface velocity field. This approach is based on two observations. Firstly, there exists a temporal lag between the "simultaneous" acquisitions of the panchromatic and multispectral data. This is due to the geometry of the SPOT-5 sensor. Therefore moving objects will appear at slightly different locations in the two images. Secondly, the relative displacements of objects between images can be measured using well established image-matching techniques.

De Michele et al. (2012) made use of the 2.04 second time lag between the panchromatic and multispectral acquisitions between the SPOT-5 bands and a subpixel phase cross-correlation image matching technique, implemented in the COSI-Corr software package (Leprince et al. 2007), to directly measure the surface velocity field. The idea of airborne and spaceborne time lags in the order of milliseconds to minutes has been used in a few other studies with specific applications to cars (Reinartz et al. 2006), ships (Takasaki, Sugimura & Tanaka 1993), river ice debris (Kääb & Prowse 2011; Kääb, Lamare & Abrams 2013; Beltaos & Kääb 2014) and sun glint (Matthews & Awaji 2010).

Image matching refers to techniques that are used to identify and measure corresponding features or patterns on overlapping images that are captured at different viewing angles, at different times or by different sensors. Image matching has been used for a number of applications including image co-registration, DEM generation and displacement measurements (Brown 1992; Zitová & Flusser 2003). Existing image matching techniques can be divided into area-based matching, feature-based matching and relation-based matching. Due to its simplicity, the area-based matching technique is the most commonly used method (Zitorá & Flusser, 2003).

Area-based matching makes use of moving correlation windows to determine the correspondence (i.e. the similarity of their grey level values) of two image areas. Such windows consist of a local neighbourhood of pixels. This technique makes use of the characteristics of these windows to match feature locations in one image to features in another. The reference window in the first image remains in a fixed location. Search windows in the second image are evaluated with relevance to the reference window. During the correlation process, many different search windows are evaluated until a location is found that best matches the reference window.

Normalized cross-correlation (NCC) is the most commonly used area-based matching method due simplicity, reliability and robustness (Lewis 1995). The features considered in this method include brightness and contrast. Due to the fact that the image windows are normalized, it is not necessary to balance the contrast or brightness prior to running the correlation. NCC calculates the normalized cross-correlation coefficient of the reference window and search template (Figure 2.21). This value is then assigned to the centre pixel of the search template. This process is iterated, shifting the search template by one pixel after each iteration until the entire search window has been covered. Once complete, the pixel in

the search window with the highest correlation coefficient is considered as the best match for the centre pixel in the reference window. The Euclidean distance between the coordinates of the two centre pixels is considered as the horizontal displacement magnitude.
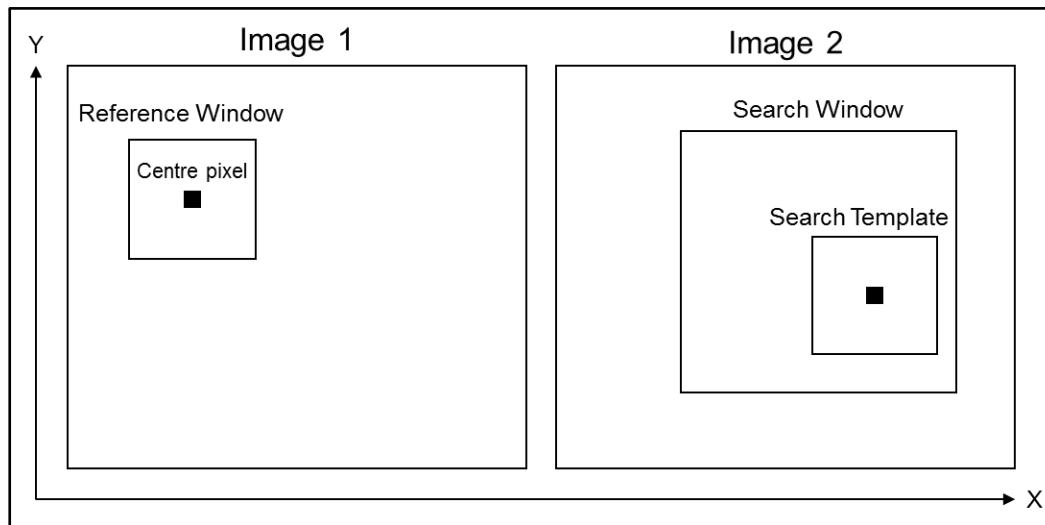
Adapted from Debella-Gilo et al. (2011)

Figure 2.21 Simplified representation of NCC image pairs together with the reference window, search window, search template and central pixel.

Correlation Image Analysis Software (CIAS) is a free and stand-alone piece of software that can be downloaded from the University of Oslo's Department of Geosciences website (http://www.mn.uio.no/geo/english/research/projects/icemass/cias/). It was originally written by Andreas Kääb and Mark Vollmer (Kääb & Vollmer 2000) and was further developed by Andreas Kääb. CIAS implements NCC and normalised cross-correlation orientation (NCC-O).

CIAS takes two signal band (grey scale) images of an area which are separated by a time lag, as input. Both images must have the same spatial resolution and must have square image pixels. If the images are not co-registered, there is an option for the co-registration of the images using Helmert transformation. The overall movement is, by default, derived in metres but this may vary depending on the reference system of the input images. Other important outputs include the direction of movement, given in degrees and the corresponding correlation parameters including average correlation coefficient and the maximum correlation coefficient. Process parameters and settings are recorded in a log file.

CHAPTER 3: RESEARCH METHODS AND MATERIALS

3.1 STUDY AREA

South Africa is located at the southern tip of the African continent. Its' coastline extends for 2798 km (CIA 2014), from the Orange River (28° 38' S, 16° 27' E) on the west coast to the Mozambique border on the east coast (26° 51' S, 32° 53' E) (Tinley 1985).

The majority of the South African coastline has a moderate (1-2 m) to high (2-3 m) wave energy environment, dominated by south and south-westerly swells that are generated within the westerly gale zone known as the roaring forties (Heydorn & Tinley 1980; Roussouw, Terblanche & Moes 2013). Along the east coast, the swell is refracted and thus approaches from a south-south-east to a south east direction. The largest inshore wave heights occur at exposed areas along the south-west and south coasts and gradually decrease northward along the west and east coasts (Rossouw & Theron 2009; Joubert & van Niekerk 2013; Theron 2016). Wave periods along the South African coastline typically range between 8 and 16 seconds, although waves with larger maximum peak periods can be generated by the wind (South Africa 2004).

This study was conducted at four locations along the coast of South Africa (Figure 3.1). The selection of multiple locations allowed for the techniques to be tested under varying wave conditions (i.e. different heights and directions etc.). Each location was selected based on availability of RapidEye satellite imagery as well as directional wave buoy data. At each location, a study area of 4x4km surrounding the wave buoy was selected (Figure 3.2). Richards Bay was used as a pilot site for establishing the methods; thereafter, the methods were applied to Durban, East London and Cape Point.
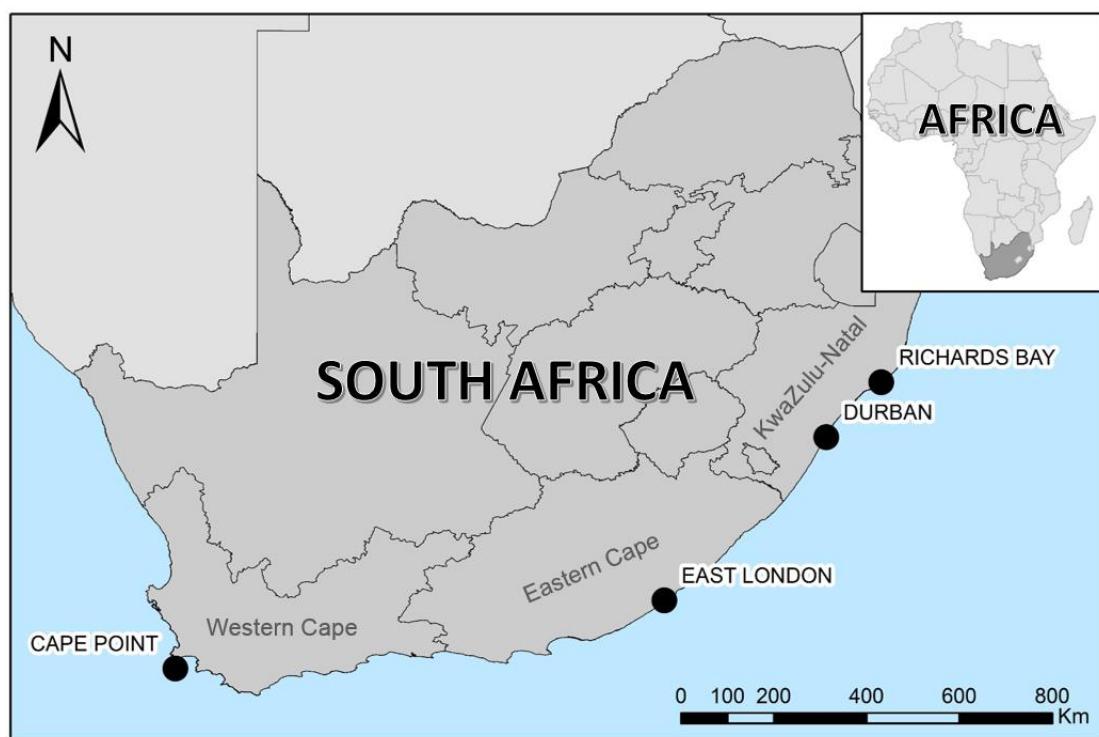
Figure 3.1 Location of the four study sites along the coast of South Africa.
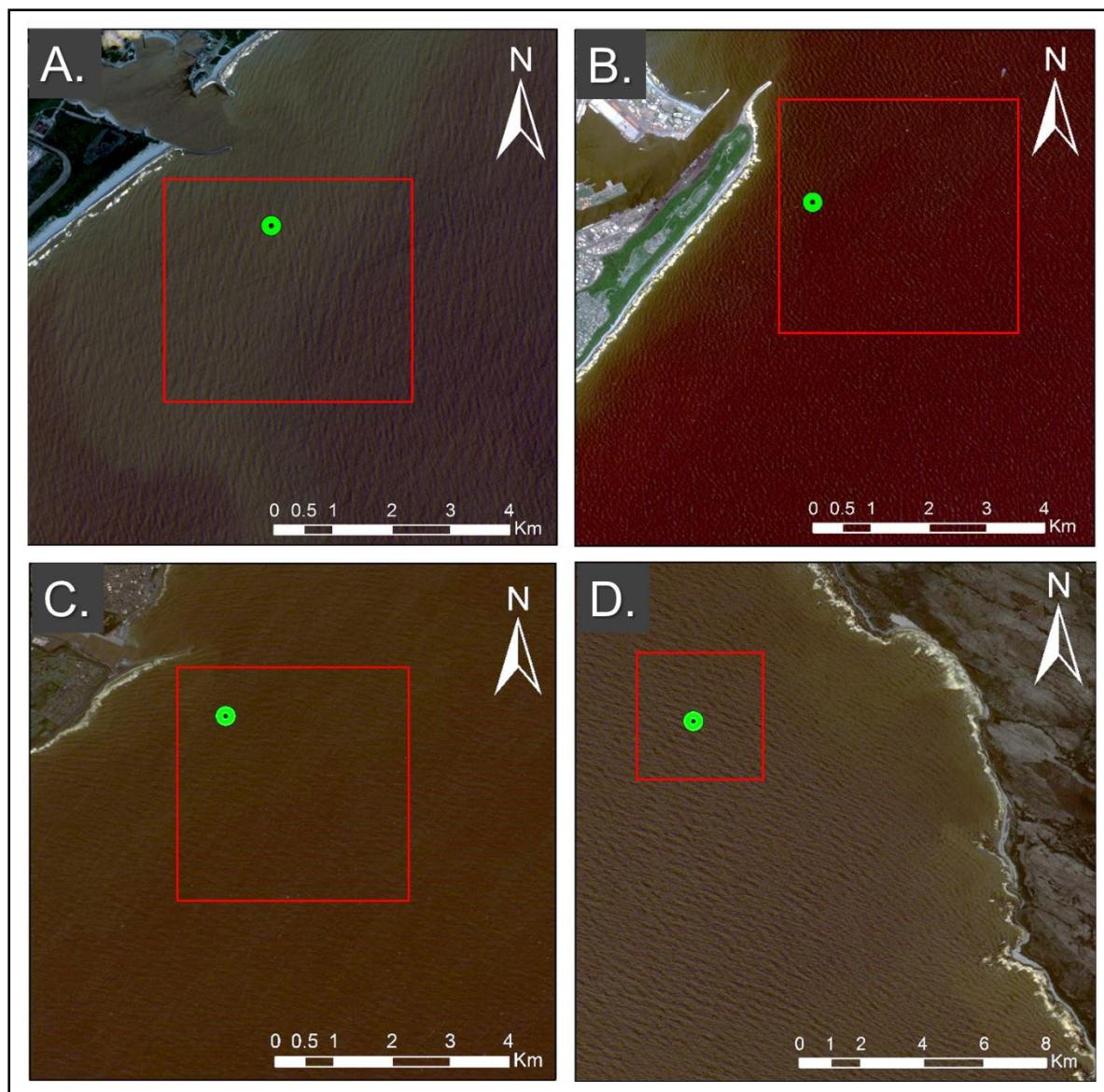
Figure 3.2 4x4km areas, surrounding the wave buoys (green dots), selected for the extraction of ocean wave characteristic parameters. A) Richards Bay, B) Durban, C) East London and D) Cape Point.

3.1.1   Richards Bay and Durban

Durban and Richards Bay are located in the subtropical coastal zone of KwaZulu-Natal (KZN) on the east coast of South Africa. The coast is generally linear with a few bays and is comprised of sandy beaches with intermittent rocky outcrops (Palmer et al. 2011). The presence of sandy beaches along with a high-energy, swell dominated coast and an average tidal difference of two metres, make this stretch of South Africa's coastline particularly vulnerable to erosion (Mather 2010; Smith et al. 2010).

The warm climate and aesthetic scenery make the KZN coastline a popular destination for tourist and leisure activities (Gobel & Mackay 2013). This has resulted in a high population

density along the KZN coast (322 people/km^2) (Statistics South Africa 2001) and a high concentration of infrastructure.

Durban and Richards Bay are the main centres of commercial and industrial activity in the province. Durban hosts South Africa's premier multi cargo port and is among the busiest ports in Africa, while Richards Bay has the continent's deepest port, handling a greater volume of cargo than any other port in Africa (Transnet National Ports Authority 2010).

The KZN coastline is dominated by large amplitude swells, which move from a southerly direction. These swells are generated by eastward moving low pressure cells that pass to the south of South Africa (Rossouw 1984). Such swells generally approach from a southerly to south-westerly direction (Rossouw 1984) but refract, when they enter the shallower waters (<100 m) over the continental shelf, to a south-south-easterly direction.

The Richards Bay wave buoy is located at 28° 49' 35.40" S, 32° 06' 14.40" E, in 22 m of water, approximately 1.4 km off the point of the port's southern breakwall (Figure 3.2A). The Durban wave buoy is located at 29° 53' 02.40" S, 31° 04' 14.40" E in 30 m of water, about 1.7 km from the shore (Figure 3.2B).

The combined average peak period for both sites is 10 s, the average significant wave height is 1.65 m and the average wave direction is 130° (Corbella & Stretch 2012).

3.1.2   East London

East London is situated in the Eastern Cape Province, on the south eastern coast of South Africa. The East London port is located at the mouth of the Buffalo River, making it the only river port in South Africa. East London has a temperate oceanic climate, influenced by both the warming and cooling effects of the ocean. Equally strong north-easterly and south-westerly winds occur throughout the year (Stone, Weather & West 1998). The coastline is oriented to the north-east and characterised by rocky shores with occasional sandy beaches (Lubke 1998). This area is exposed to predominant waves approaching from southerly to north-easterly directions (Theron 2004). The coastline has very few headlands that provide protection from swell waves and thus is considered an exposed high-energy coast.

As with KZN, the Eastern Cape is dominated by swell generated to the south of South Africa. However, in the Eastern Cape, the swells approach from a south-westerly direction. The south-westerly and north-easterly winds also contribute to the wave climate off East London.

South-westerly winds generate waves that move from a south-westerly direction against the Agulhas current and north-easterly winds generate north-easterly waves, although less frequent, which travel with the Agulhas current (Theron 2004).

As these swells approach the shore, they refract and approach from a south-easterly to south-south-easterly direction. Van der Merwe (2017) reported the near-shore wave climate of East London as having an average significant wave height of 1.6 m, an average peak period of 13 s and an average direction on 140°.

The East London wave buoy is situated 33° 02' 16.80" S, 27° 55' 50.99" E in 27 m of water, about 1.2 km to the south-east of the harbour breakwall (Figure 3.2C).

3.1.3   Cape Point

Cape Point is located on the south-east corner of the Cape Peninsula, at the extreme south-western tip of South Africa. The Cape Point location falls on South Africa's diverse south-west coast which is characterised by rocky cliffs interspersed by pocket beaches (Element Consulting Engineers 2014). The Cape Point region has a Mediterranean climate, indicating warm dry summers and cool, wet winters.

The offshore wave climate is dominated by swell waves from the south-west with periods ranging between 9 and 18 seconds. Locally generated wind waves primarily move from a south-east direction and have periods extending up to four seconds (Element Consulting Engineers 2014). During the winter months of May through September, slightly larger waves occur. These coincide with storm events that occur over the ocean during this period. In Spring, the mean direction shifts about 15° in an anti-clockwise direction in response to locally generated waves as opposed to being dominated by swell waves (Element Consulting Engineers 2014).

The Cape Point wave buoy is located at 34° 12' 14.40" S, 18° 17' 12.01" E about 5.4 km off the eastern shore of Cape Peninsula at a depth of 70 m (Figure 3.2D).

3.2   DATA

3.2.1   RapidEye imagery

RapidEye is a constellation of multispectral earth observation satellites that has been in operation since February 2009. Currently, RapidEye is owned and operated by Planet Labs.

The constellation consists of five identical pushbroom sensors on the same orbital plane which are calibrated equally to each other (RapidEye 2012). This means that an image from one RapidEye sensor will be identical in characteristics to an image from any of the other four sensors.

The RapidEye constellation operates on a sun-synchronous 630 km altitude orbit with a daily repeat cycle. These sensors record spectral information in five bands. Each of these bands has a spatial resolution of 5x5m and 12 bits of dynamic range (RapidEye 2012). Table 3.1 provides an overview of the spectral bands captured by the RapidEye sensor.

Table 3.1 RapidEye spectral bands.

Bands	Wavelength (micrometres)
Band 1 - Blue	0.440 - 0.510
Band 2 - Green	0.520 - 0.590
Band 3 - Red	0.630 - 0.685
Band 4 - Red Edge	0.690 - 0.730
Band 5 - Near Infrared (NIR)	0.760 - 0.850

The approach used in this study makes use of bands 1, 3 and 5. The data were acquired from the Council for Scientific and Industrial Research (CSIR). The dates of capture range from December 2009 to January 2010. The images selected for this study are listed in Table 3.2. Due to the limited budget available for this thesis, only one acquisition date per study area from an existing data archive could be used. While this has implications on the statistical error quantification of the results, for a pilot study which is testing the general concept of applicability, the mono-temporal coverage of the study sites was assumed sufficient.

Table 3.2 List of RapidEye scenes per study area.

Area	Scene	Acquisition Date	Local Acquisition Time
Richards Bay	IMG_MS5_031E_51_028S_58_100114_084646	2010/01/14	10:46:46 am
Durban	IMG_MS5_030E_48_030S_09_091222_084402	2009/12/22	10:44:03 am
East London	IMG_MS5_027E_35_032S_55_091229_091133	2009/12/29	11:11:33 am
Cape Point	IMG_MS5_018E_25_034S_08_100116_095015	2010/01/16	11:50:16 am

Most pushbroom scanners consist of multiple charge-coupled device (CCD) lines, often one for multispectral acquisition and another for panchromatic acquisition. The RapidEye sensors have separated CCD lines for the individual multispectral channels. Each CCD is mounted in

a different location in the focal plane assembly of the instrument, thus the acquisition of each spectral channel at a given point on the ground is not simultaneous. During the initial processing of such satellite data, the bands are co-registered on the same ground level (either on a specific ellipsoid height or on a digital elevation model). This results in the different bands spatially matching each other within 0.2 pixels (RapidEye 2012). However, if objects, such as waves, are moving significantly between the short acquisition time gap, they would appear at different locations in the different spectral bands (Figure 3.3). With the knowledge of this acquisition time offset, the speed at which they are travelling can be retrieved by the measurement of the relative distances of these objects between bands.
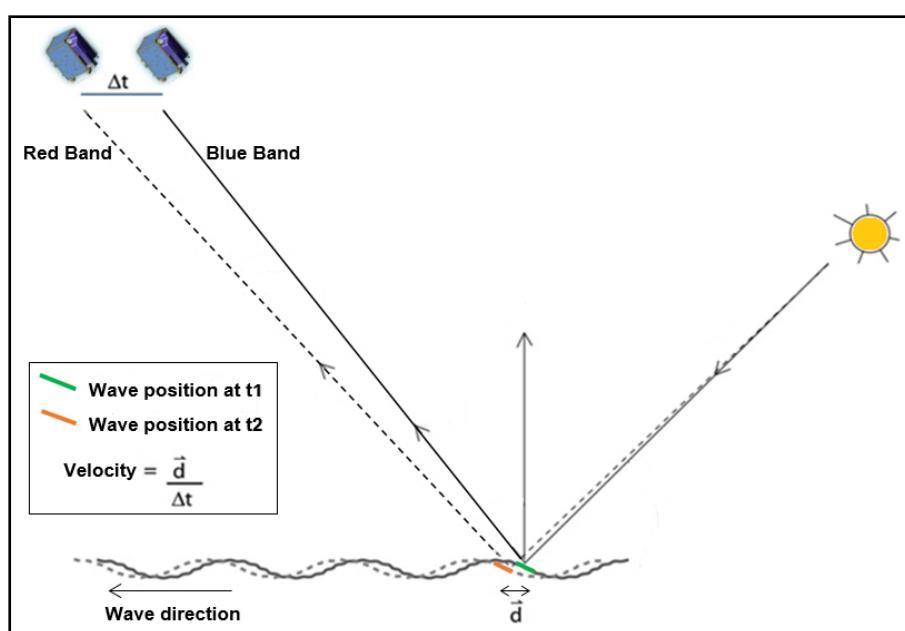
Adapted from De Michele et al. (2012)

Figure 3.3 Simplified representation of wave tracking principle.

The focal plane assembly of each RapidEye sensor consists of five separate CCD lines (i.e. one for each band) that are grouped in two mounts (Figure 3.4). One mount consists of the blue and green bands and the other of the red, red edge and NIR bands. The largest gap is found between the blue/green and red/red edge/NIR bands. Krauß et al. (2013) calculated a time lag of 3.06 s between the blue and red bands.
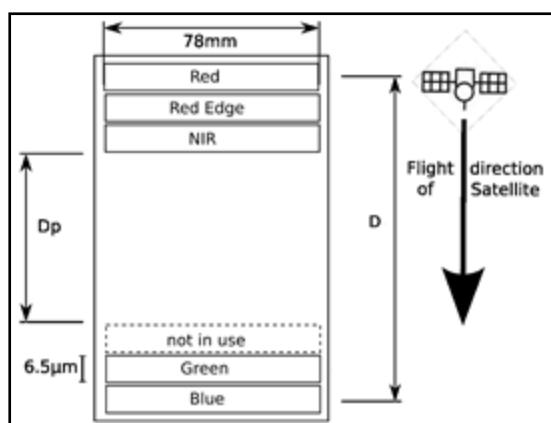
Source: Krauß et al. (2013)

Figure 3.4 RapidEye focal plane assembly, Dp: distance between the mounts, D: maximum distance between lines (red–blue).

3.2.2 Wave buoy data

The CSIR, on behalf of Transnet, continuously monitors ocean wave activities at various locations along the South African coastline. The majority of the data is measured by moored wave buoys. The buoy transmits the recorded data to a shore station where a comprehensive analysis is performed. Once analysed, the data is uploaded in near-real time to a database at the CSIR in Stellenbosch. The directional wave buoy data were necessary for validation of the results in this study.

The directional wave buoy data acquired from the CSIR consisted of two datasets for each study site. The first dataset contained characteristic wave parameters (in the form of a text file) such as wave height, wave period, wave direction and spreading. The second dataset contained a matrix of directional frequency data (in the form of a developer studio project (DSP) file), which included the energy (in mm^2/Hz) per direction (ranging from 1˚-360˚) along the x axis (horizontal) and frequency (118 frequencies ranging from 0.005 Hz-0.59 Hz at 0.005 Hz intervals) along the y axis (vertical). Both datasets were calculated at 30 minute time intervals for the same date that each RapidEye image was captured. The exact 30 minute interval used for each study site is listed in Table 3.3.

Table 3.3 Local acquisition time interval of the wave buoy data that were used for validation of the results.

Area	Acquisition Date	Local Acquisition Time of RapidEye images	Local Acquisition Time Interval of Wave Buoy Data
Richards Bay	2010/01/14	10:46:46 am	10:30 am - 11:00 am
Durban	2009/12/22	10:44:03 am	10:30 am - 11:00 am
East London	2009/12/29	11:11:33 am	11:00 am - 11:30 am
Cape Point	2010/01/16	11:50:16 am	11:30 am - 12:00 am

3.2.3   Wind data

Offshore winds are the primary driving force in the generation of wind sea and swell waves. Therefore, wind data in terms of wind speed and wind direction, captured at three hourly intervals, were obtained (in the form of a text file) from the CSIR to assist with the analyses of the results. For each study site, data were acquired for the date of acquisition as well as for the two days prior to acquisition. For Richards Bay, Durban and East London the data were captured by the port control weather stations located at the Richards Bay, Durban and East London ports. Unfortunately, for the Cape Point study site, the nearest available weather station is the table bay port control weather station, located roughly 36 km to the north east.

3.3   PREPROCESSING OF RAPIDEYE DATA

3.3.1   Multispectral to grey scale

The rate of absorption of electromagnetic energy as it passes through water is wavelength-dependant. Energy with the shortest wavelengths can penetrate water the deepest. At NIR wavelengths, energy is absorbed very strongly by water (Mobley 1994). NIR imagery over the ocean is, therefore, composed only of a specular reflection component (i.e. sun glint) and a spatially constant NIR water component. Therefore over the ocean, the only features that influence the brightness of the NIR band are ocean waves as they modulate the sun glint. When performing a Fourier transform on an image, all features that are visible in the image will be represented in the output. This study is only interested in ocean waves. Therefore, the NIR band was selected for the extraction of the wave spectrum.

Visible bands penetrate water deeper than the NIR band and could thus reveal subsurface features, such as seafloor features and changes in water colour. These bands are therefore considered less suitable than the NIR band for extraction of the wave spectrum using an FFT, as subsurface features may influence the result. However, the approach used for the calculation of the phase velocity field measures the displacement of features between two

images. Visible subsurface features would remain stationary between the acquisition of the blue and red band and are therefore not likely to affect the result. The blue and red bands, and the associated maximum time lag between them, were therefore used for the extraction of the phase velocity field.

For each RapidEye image, the blue, red and NIR bands were extracted and stored as individual (grey scale) images. This procedure was performed in ERDAS IMAGINE (Version 15.1) using the spatial modeller.

3.3.2   Subsetting the NIR band

Prior to extraction of the directional spectrum, the NIR bands were subsetted in ERDAS to the 4x4km extent of the study area (Figure 3.2). The size of the area was considered large enough to contain adequate coverage (i.e. contain enough waves) for a comparison with the wave buoy data (30 minute interval), while not too large to render it computationally inefficient. Furthermore if there area is too large, there would be an increased influence of near-shore wave transformations (Section 2.1.2) which would affect the characteristic parameters that are being extracted. Therefore, if the area is too large the RapidEye subset could possibly include waves with different characteristic parameters as compared to the wave buoy. This would result in a misleading comparison.

The blue and red bands were not subsetted as the area of interest for the phase velocity field was selected manually in while running CIAS (Section 3.5.2.1).

3.4   PREPROCESSING OF WAVE BUOY DATA

For each study area, the DSP files were processed to a useable data format (Comma-separated values (CSV) file). The MATLAB (version R2016a) programming language was used to calculate the directional wave spectrum for the buoy data. The code that was written to achieve this can be seen in Appendix A.

The MATLAB *PolarContour* function creates a polar plot for the presentation of directional data and was originally designed to plot the directional spectrum of ocean waves. The *PolarContour* function accepts two inputs. The first is a matrix of the directional data, with the frequency on the x axis and the direction on the y-axis. It was therefore necessary to transpose the input data.

The second input is an index of frequency intervals. For this, the same intervals as in the DSP file were defined (i.e. 0.005 Hz – 0.59 Hz at 0.005 Hz intervals).

The wave buoys record directional measurements relative to magnetic north; however the RapidEye imagery is relative to true north. Therefore, before the *PolarContour* function could be used, the transposed matrices of directional data were corrected for the magnetic declination. The magnetic declination values that were used for each study site can be seen in Table 3.4. These values were calculated with the International Geomagnetic Reference Field (IGRF) model (https://www.ngdc.noaa.gov/IAGA/vmod/igrf.html) and rounded to the nearest degree.

Table 3.4 Magnetic declination for each study site.

Area	Magnetic Declination
Richards Bay	23° West
Durban	24° West
East London	27° West
Cape Point	25° West

3.5   EXTRACTION OF CHARACTERISTIC WAVE PARAMETERS FROM RAPIDEYE

In this study, two approaches were performed on the RapidEye imagery. The first aimed at extracting the directional wave spectrum and characteristic wave parameters including wavelength, wave period and wave direction. This methodology is explained in Section 3.5.1. The second process aimed at extracting the phase velocity field of ocean waves and is explained in Section 3.5.2.

3.5.1   Extraction of the directional spectrum

MATLAB code was developed to extract the directional wave spectrum and characteristic wave parameters from RapidEye imagery. The full MATLAB script can be seen in Appendix B and follows the basic process flow outlined in Figure 3.5.
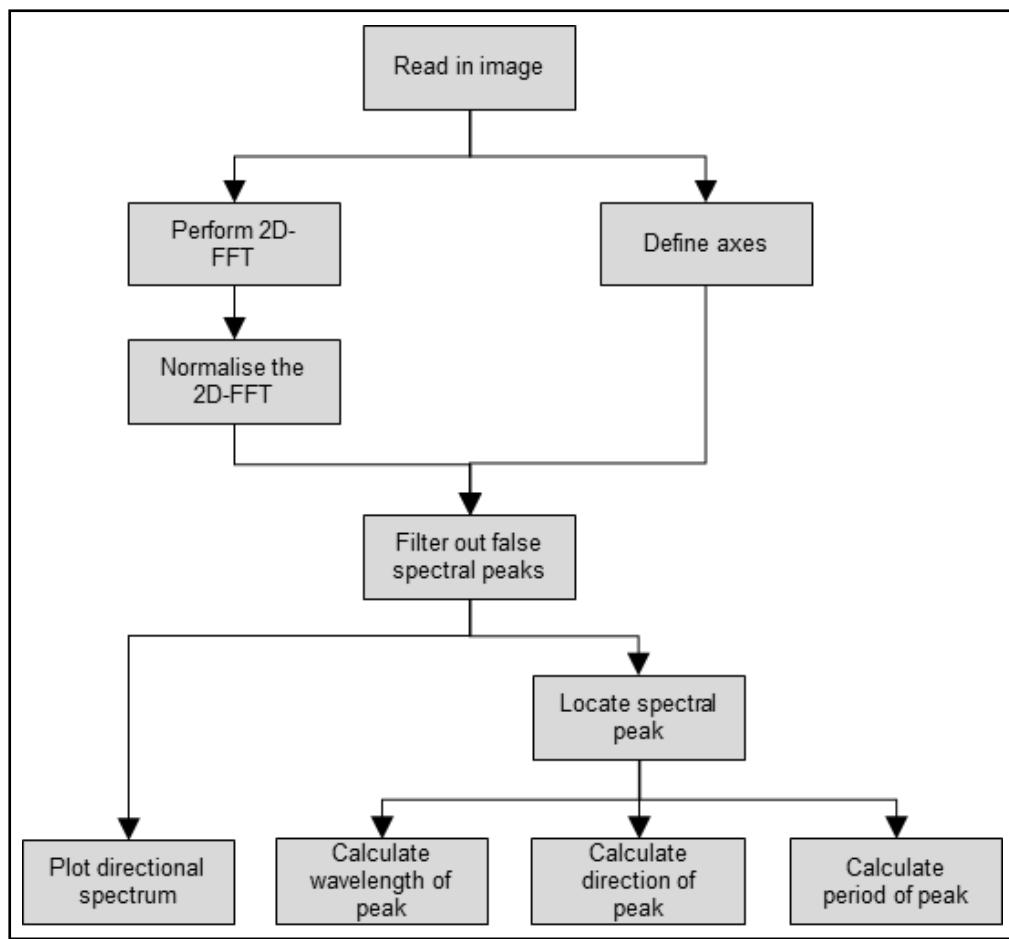
Figure 3.5 Workflow diagram for the extraction of the directional spectrum and characteristic wave parameters using MATLAB.

3.5.1.1   Two-Dimensional Fast Fourier Transform (2D FFT)

A 2D FFT was performed on the subset NIR grey scale image (tagged image file format (TIFF)) for each study area. This was achieved using the *fft2* MATLAB function. The *fft2* function produces the 2D Discrete Fourier transform (DFT) of each image (MATLAB 2016b). 2D DFT is a DFT over one dimension followed by a DFT of the second dimension of the data.

In addition to the *fft2* function, the *fftshift* function was used to shift quadrants of the Fourier transformed image so that the lowest frequency components were in the centre of the plot. As the output of the FFT is a complex number, the *abs* function was used to plot its magnitude.

3.5.1.2   Normalisation

When using a Fourier transform, the size of the input data affects the total energy represented in the Fourier plot. In the context of images covering the ocean, an image with a larger spatial extent will contain a higher number of waves than an image with a smaller spatial extent.

Therefore, the larger image will have a higher total energy represented in the Fourier plot even if the waves have the same characteristic parameters in each image. In order to produce directional wave spectra from the RapidEye images that are comparable to each other, the spectra were normalised by the size (i.e. the number of pixels) of the input image.

3.5.1.3   Define axes

MATLAB plots the spectra on axes representing the number of pixels in the x direction, as the x axis, and the number of pixels in the y direction, as the y axis. However, the normalised spectrum is a function of spatial frequency (i.e. x component (k_x) and y component (k_y) wavenumbers). Therefore, spatial frequency axes had to be computationally defined.

As mentioned in Section 2.1, the wavenumber is measured in cycles per unit distance, where the complete cycle of a wave is considered to have an angular displacement of 2π radians. Wavenumber (k) is, therefore, related to wavelength (λ) by $k = 2\pi/\lambda$.

The largest wavenumber that could exist in an image is, therefore, related to the smallest possible wavelength. In the context of imagery, the resolution of the image determines the smallest detectable wave. Due to this and the fact that the origin was shifted to the centre of the plot, the axes were defined from $-\frac{\pi}{res}$ to $\frac{\pi}{res}$, where res is the resolution of the imagery (in this case 5 m).

3.5.1.4   Filter to remove false central spectral peaks

A filter was run on the directional spectra to remove unreliable spectral peaks that were not related to the observed ocean waves. The spectral peaks occur at low frequencies in the directional spectra and are a result of inherent computational difficulties associated with the input data and current methodology.

The low frequency peaks occur because the four outer edges of the images are identified as parts of a sinusoidal signal. This results in strong spectral peaks, scaled to these dimensions, being plotted on the directional spectra. Therefore, the low frequency central group of peaks, that were unrelated to the ocean waves, were removed. This was achieved by setting all values to zero in the directional spectra that correspond to having a wavelength of more than 400 m, thereby making the spectral peaks related to visible ocean waves the most prominent (Figure 3.6).
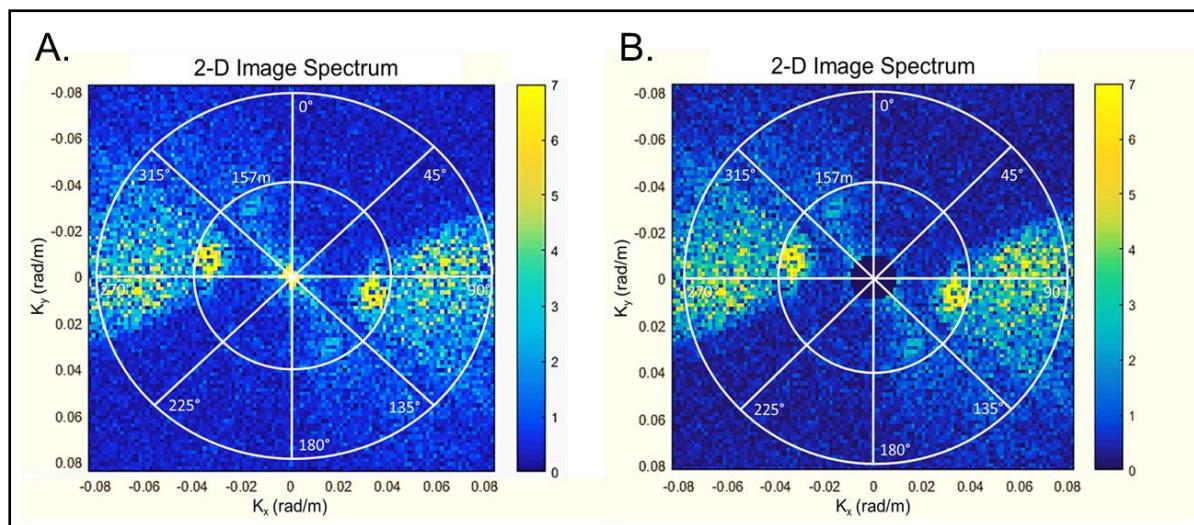
Figure 3.6 A) Directional spectrum before filter has been applied and B) Directional spectrum after filter has been applied.

3.5.1.5   Calculation of characteristic wave parameters

The location of the spectral peak (k_{x_peak}, k_{y_peak}) was found in order for the wavelength, wave period and direction associated with the spectral peak to be calculated.

Once the location of the spectral peak was known, the peak wavelength (λ_p), peak wave period (T_p) and peak wave direction (θ_p) were calculated using the following equations:

$$\lambda_p = \frac{2\pi}{\sqrt{k_{x\_peak}{}^2 + k_{y\_peak}{}^2}}$$

Equation 3.1

where λ_p is the peak wavelength extracted from the directional spectrum;

k_{x_peak} is the x component wavenumber of the spectral peak; and

k_{y_peak} is the y component wavenumber of the spectral peak.

$$T_p = \sqrt{g \cdot \sqrt{k_{x\_peak}^2 + k_{y\_peak}^2} \cdot \tanh\left(\sqrt{k_{x\_peak}^2 + k_{y\_peak}^2} \cdot h\right)}$$

Equation 3.2

where T_p is the peak wave period extracted from the directional spectrum;

g is the acceleration due to gravity (9.8 m/s^2); and

h is the water depth.

$$\theta_p = \tan^{-1}\left(\frac{k_{y\_peak}}{k_{x\_peak}}\right)$$

Equation 3.3

where θ_p is the peak wave direction extracted from the directional spectrum.

3.5.2   Extraction of the phase velocity field

Normalised cross correlation (NCC) was identified as a potential technique to extract directional phase velocity of near-shore ocean waves. The methodology used for generating a phase velocity field of near-shore ocean waves follows Figure 3.7.
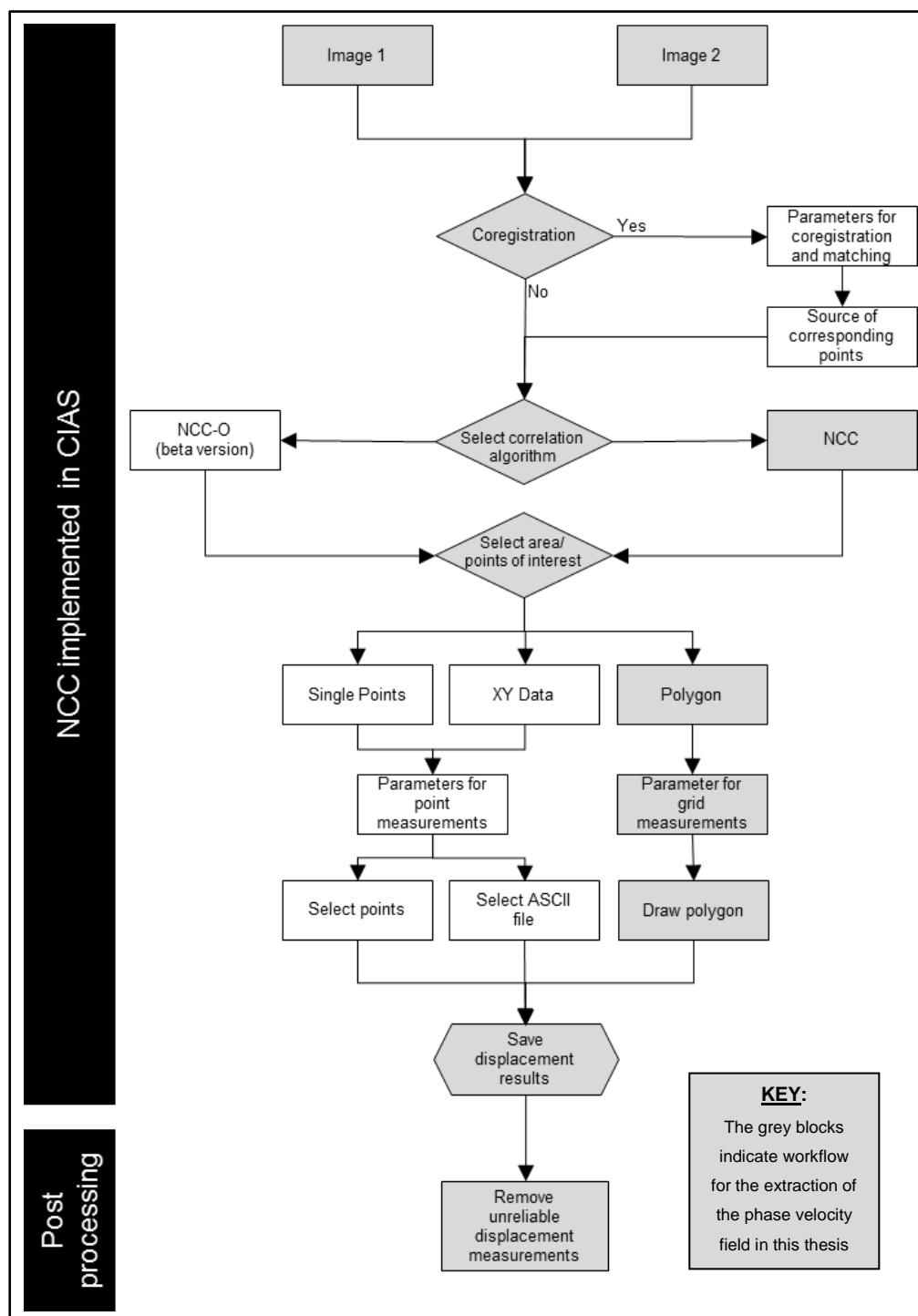
Figure 3.7 Workflow diagram for CIAS.

3.5.2.1   Normalised Cross Correlation using CIAS

The Interactive Data Language (IDL) virtual machine is used to run CIAS. For the analysis of near-shore ocean wave phase velocity, the blue band was used as input image one and the red band was used as input image two. As stated in Section 3.2.1, these bands cover the same area, spatially match each other within 0.2 pixels and differ in acquisition time by 3.06 s. The optional co-registration in CIAS was thus not necessary.

The NCC algorithm was selected as the correlation algorithm. A polygon was used to identify the measurement points. The NCC grid parameters were defined before the polygon was digitised on screen. These parameters included the reference window size (in pixels), the search area size (in pixels) as well as the grid distance (in meters) and are important considerations when using NCC. The reference window size should be large enough to maximise the signal-to-noise ratio and small enough to minimise velocity gradients, the search area should be large enough to measure the furthest moving window and small enough to limit memory usage and the grid distance should equal the raster resolution.

The CIAS help documentation advises that the search area size must at least be double the maximum expected displacement. In this study, the reference window was set to 40 pixels (200 m), the search area size set to 50 pixels (250 m) and the grid distance set to 5 m. Polygons were digitised on screen and where made up of an area extending from the shore to just beyond the wave buoy at each study site.

The various outputs were saved as text files.

3.5.2.2   Post-processing of output

The resulting displacement measurements cannot be assumed to represent the final wave movement statistics. Post-processing is necessary to assess the reliability of the results. This is performed by analysing the correlation coefficient values of the results and removing invalid correlations.

Correlation coefficient values range between -1 and 1, where -1 indicates matching entities which are the inverse to one another, 0 indicates no correlation and 1 indicates entities that match. It should be noted that in some cases there may not be a true correspondence between the images. However, there will still be a set of correlation coefficients calculated and the highest value will be chosen as a match. It is, therefore, important to set a threshold for the correlation coefficient, below which the matched results must be rejected.

For the purpose of this study, all displacement measurements that had a correlation coefficient less than 0.6 were considered unreliable. The NCC outputs were imported into ArcMap (version 10.3) and saved as a point shapefile, where-after all displacement measurements with a correlation coefficient of less than 0.6 were removed.

CHAPTER 4:   RESULTS AND DISCUSSION

The results have been divided into Directional Wave Spectrum Results (Section 4.1) and Phase Velocity Field Results (Section 4.2). The Directional Wave Spectrum Results present the wave spectra and characteristic parameters produced by the 2D FFT of the RapidEye imagery. The Phase Velocity Field Results present the phase velocity field that was extracted using NCC implemented in CIAS. To validate these approaches, test areas were specifically chosen to include an in-situ directional wave buoy. A comparison between the directional wave buoy data and RapidEye derived results are provided in both cases.

4.1   DIRECTIONAL WAVE SPECTRUM RESULTS

4.1.1   Characteristic wave parameters

Table 4.1 provides the characteristic wave parameters extracted from the RapidEye derived directional wave spectra as well as the wave buoy characteristic parameters captured for each study area. Wavelength is related to the period and should, therefore, show similar accuracies with the buoy measurements.

Table 4.1 Characteristic wave parameters extracted from the RapidEye directional spectra and the wave buoys.

Study Area	Peak Direction (°)		Peak Wavelength (m)		Peak Period (s)	
	RapidEye	Wave Buoy	RapidEye	Wave Buoy	RapidEye	Wave Buoy
Richards Bay	105°	112°	197.1	193.3	14.4	14.2
Durban	103°	94°	114.2	102.3	8.8	8.3
East London	186°	206°	137.6	114.2	10.2	9
Cape Point	196°	227°	257.2	258.4	13.8	13.3

For Richards Bay and Durban, the satellite derived wave directions were both within 10° of the buoy measurements. The wave periods differed from the buoy measurements by 0.2 s (1.4%) at Richards Bay and 0.5 s (5.7%) at Durban. The satellite derived wave direction for East London differed from that of the buoy by 20° and the period differed by 1.2 s (11.8%). Cape Point yielded results with a difference in direction of 31° and a difference in period by 0.5 s (3.6%). This indicates that the algorithm performed better for the Richards Bay and Durban images than it did for the East London and Cape Point images.

4.1.2   Analysis of the 2D FFT results

There are two types of waves that contribute to directional wave spectra. These include longer swell waves and shorter wind waves. Swell waves are mostly generated offshore, whereas wind seas are generated by local wind events. In order to assist in the analysis of the results, wind direction and wind speed preceding the time of image acquisitions have been analysed.

4.1.2.1   Richards Bay

From Table 4.1, it is evident that the approach produced the most accurate results for Richards Bay. Figure 4.1 displays the result of the 2D FFT algorithm for Richards Bay. The figure displays A) the RapidEye NIR band subset which was used to produce the directional wave spectrum, B) the resulting directional wave spectrum and C) the directional wave spectrum calculated from the wave buoys data for comparative purposes. Bright colours in B and outlined areas in C represent the spectral peaks. The strength of the spectral peaks are represented by the brightness of the colour. The location of these peaks were used to describe the characteristic wave parameters associated with the measured sea state.
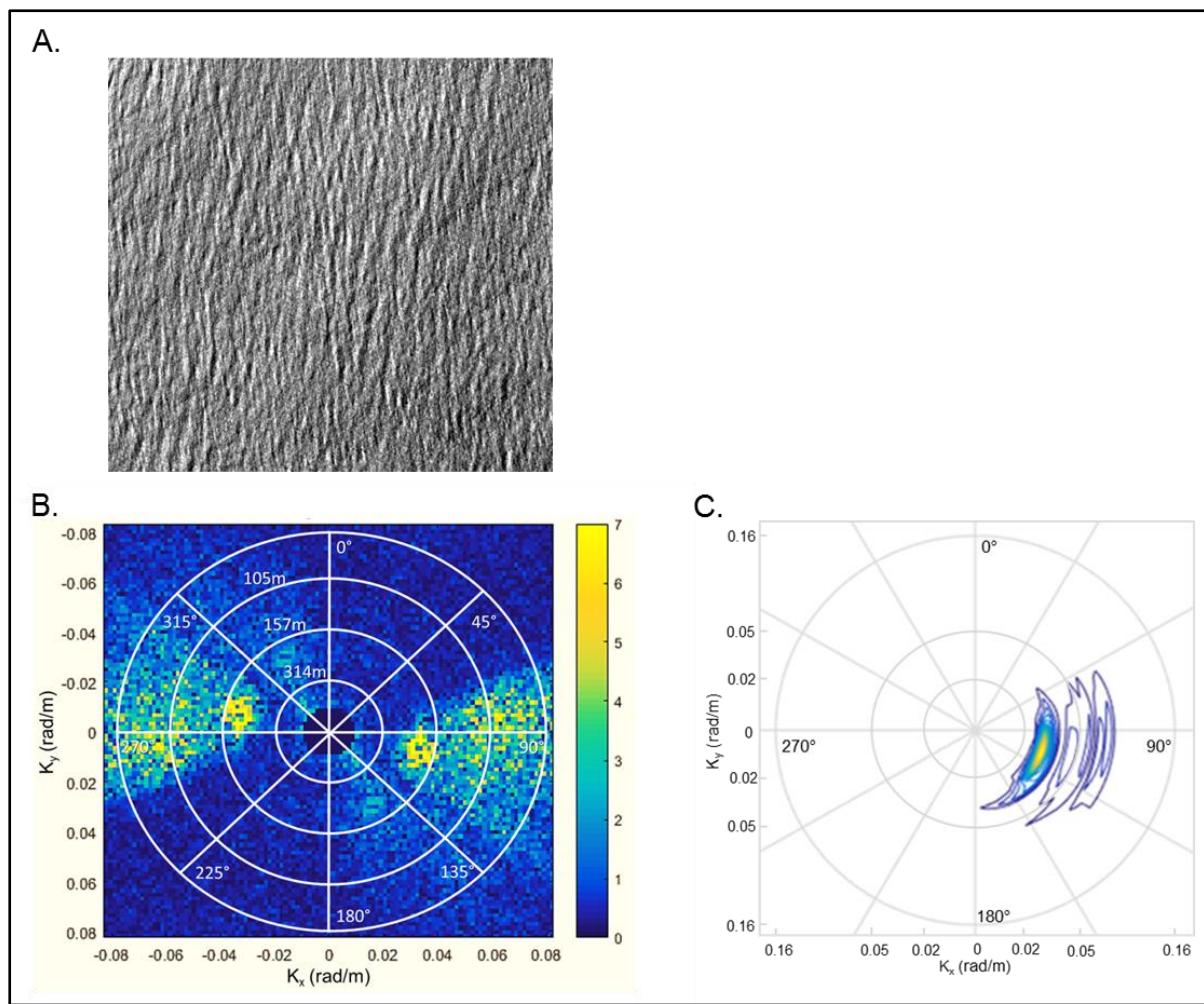
Figure 4.1 Richards Bay spectral analysis results. A) RapidEye NIR band subset, B) RapidEye derived directional spectrum and C) Wave buoy derived directional spectrum.

Wind data for Richards Bay (Figure 4.2) indicate low wind speeds (2-4 m/s) 24 hours prior to image acquisition. Wind started to increase in speed and changed direction two hours prior to acquisition, reaching a speed of around 9 m/s and a direction of 65° at the time of acquisition.
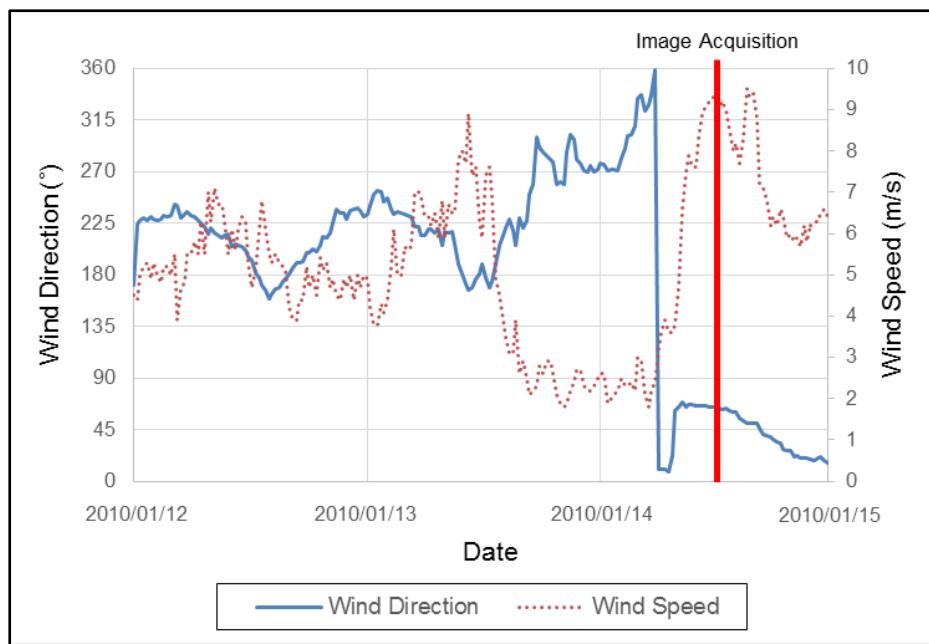
Figure 4.2 Wind speed and direction experienced at Richard Bay prior to acquisition.

Upon evaluation of the buoy spectrum (Figure 4.1C), it was found that there was no wind sea present. This indicates that the duration of the increased wind speed was not sufficient to produce a wind sea by the time of acquisition. Therefore both spectra (Figure 4.1B and C) exhibit a spectral peak around 90° as a result of swell.

Interestingly, a second peak at 155° exists in the RapidEye spectrum (Figure 4.1B) and not in the buoy spectrum. It was, therefore, surmised that this peak was the result of features other than ocean waves. In the RapidEye imagery (Figure 4.1A), a set of unique linear features, parallel to the wind direction at the time of acquisition can be observed. From this information, it was concluded that the directionally ambiguous peak around 155° is the result of local winds with a direction of 65° at the time of acquisition.

4.1.2.2 Durban

For the Durban study site, the RapidEye derived spectrum exhibits multiple spectral peaks (Figure 4.3). Two main peaks are visible in both the RapidEye derived spectrum and the wave buoy derived spectrum.
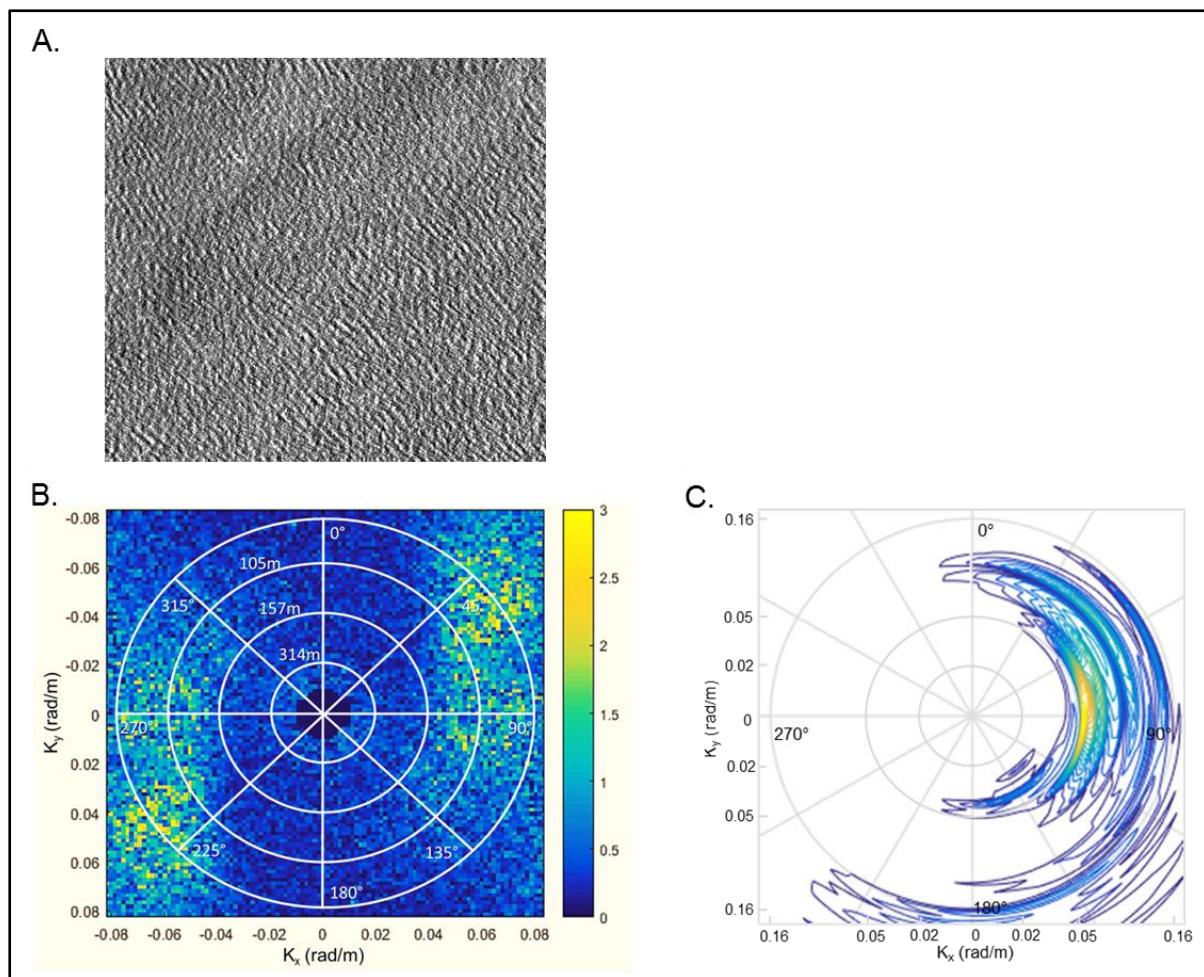
Figure 4.3 Durban spectral analysis results. A) RapidEye NIR band subset, B) RapidEye derived directional spectrum and C) Wave buoy derived directional spectrum.

The first peak (occurring around 90°) is likely due to swell waves refracting and reaching the near-shore environment. The second peak (occurring around 45°) coincides with wind conditions (45°; 4-11 m/s) present the day prior to image acquisition (Figure 4.4).
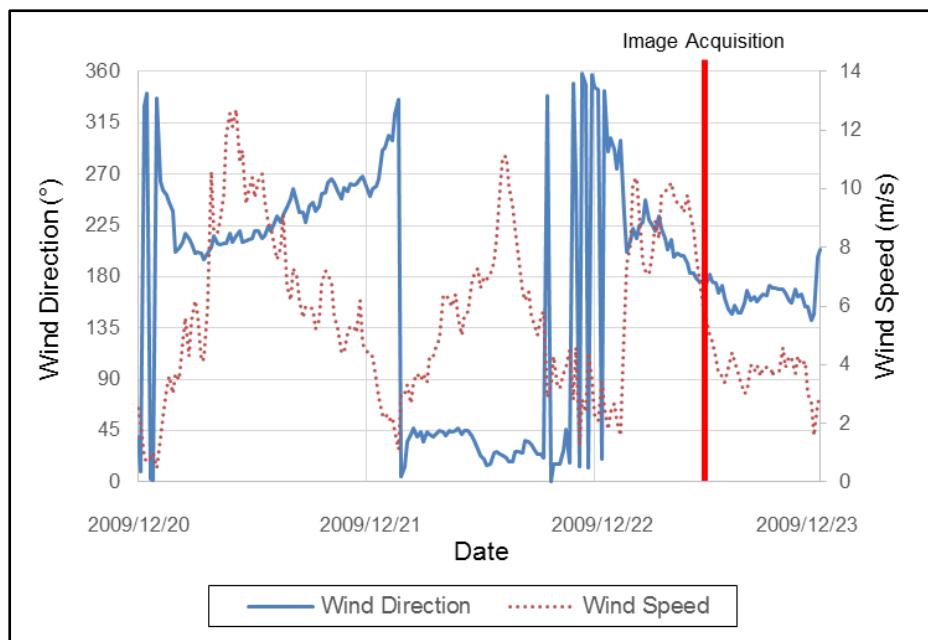
Figure 4.4 Wind speed and direction experienced at Durban prior to acquisition.

Although the wind direction did change greatly between 20h00 and 01h00 prior to acquisition, the speed dropped to 2-4 m/s and therefore during that time, it had an insignificant effect on the wave conditions. A few hours prior to acquisition the wind speed increased to 7-10 m/s with a direction between 180° and 270°. This caused the formation of small wind waves that are represented by the low spectral peak occurring between 90° and 225° in the wave buoy spectrum. These waves are not visible in the RapidEye derived spectrum possibly due to their size not being significant enough to render sun glint modulations in the RapidEye imagery.

4.1.2.3   East London

The East London study site produced the least accurate period deviation and also produced a poor directional difference. The RapidEye spectrum (Figure 4.5B) for East London indicates a spectral peak around 190° as well as another peak around 130°. The peak at 190° closely matches the peak in the buoy spectrum (Figure 4.5C). The peak formed at 130° does not feature in the buoy spectrum. Contributing features for the peak at 130° appear in the RapidEye image for East London. These are seen as diagonal linear features in Figure 4.5A running from the bottom left hand side to the top right hand side of the image.
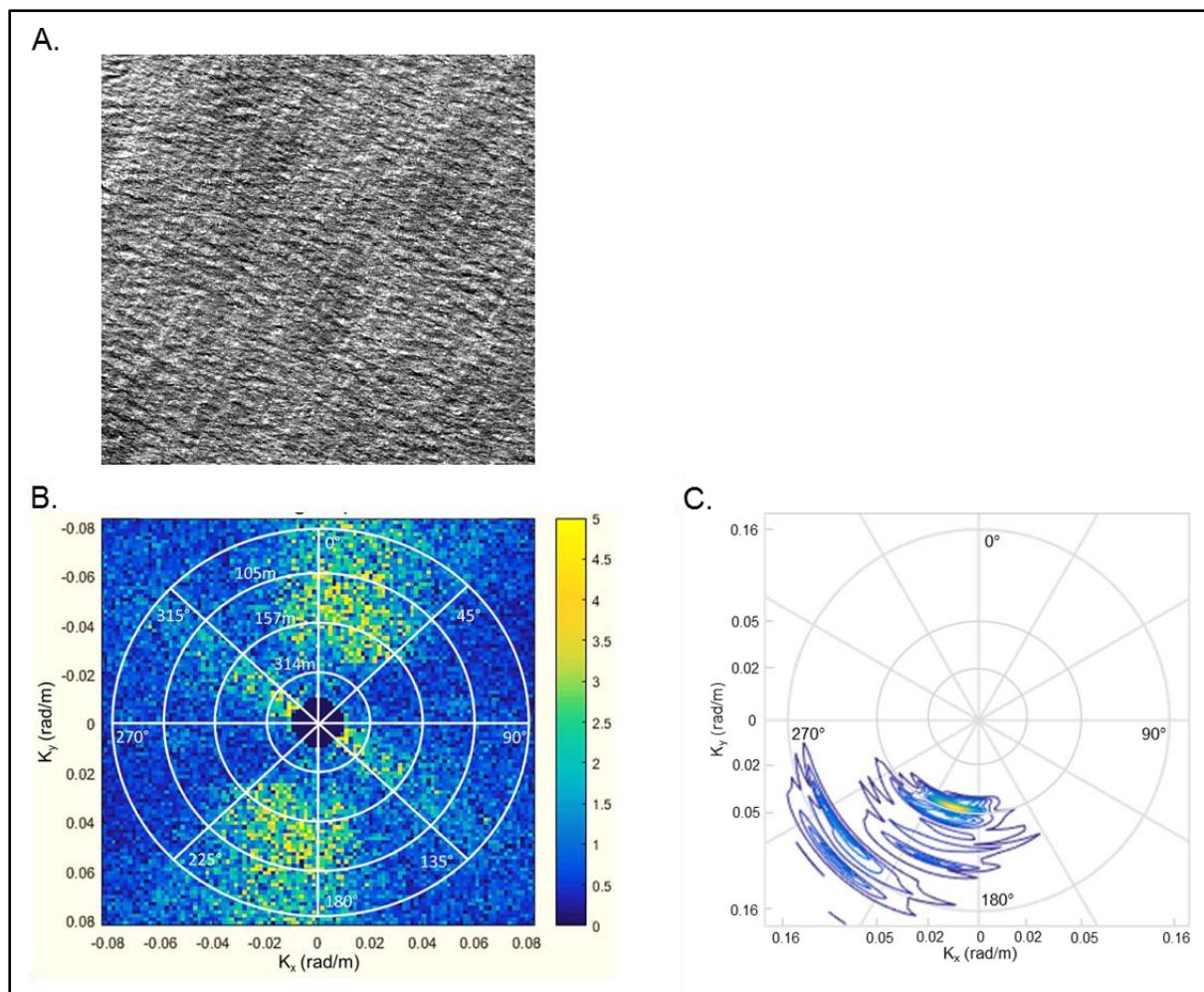
Figure 4.5 East London spectral analysis results. A) RapidEye NIR band subset, B) RapidEye derived directional spectrum and C) Wave buoy derived directional spectrum.

Wind data (Figure 4.6) indicate a direction of 220° at 12 m/s, which is parallel to these features. This follows a similar trend to Richards Bay. It is, therefore, believed that these features are the result of local wind conditions. This assumption can be further supported by the second spectral peak in the buoy spectrum occurring around 225° as a result of wind waves caused by these local winds.
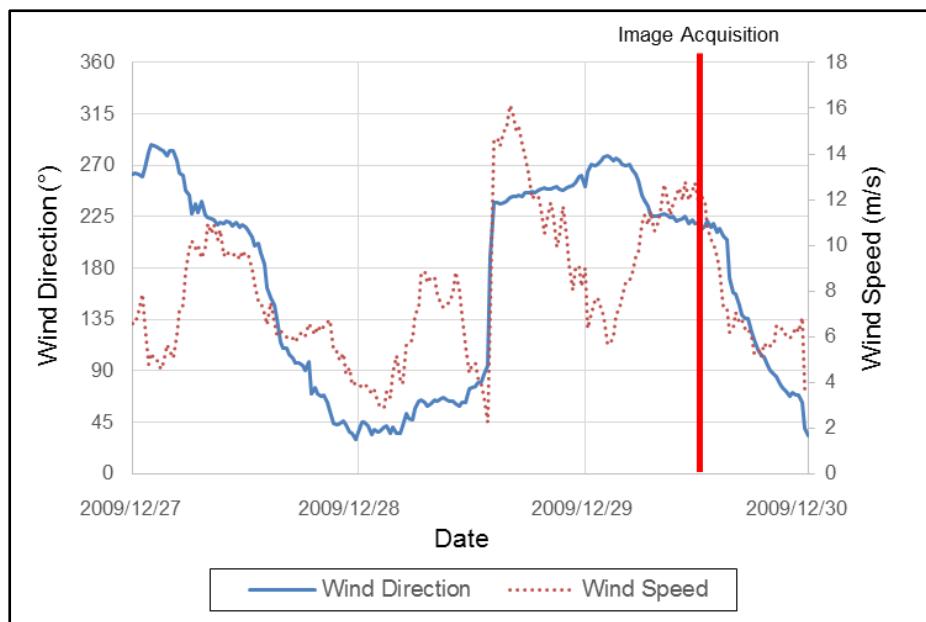
Figure 4.6 Wind speed and direction experienced at East London prior to acquisition.

4.1.2.4   Cape Point

Visually the RapidEye directional spectrum closely matched that of the wave buoy directional spectrum (Figure 4.7) and produced an accurate period that only differed from the buoy by 3.6%. However, it produced the least accurate results in terms of peak wave direction (difference of 31°).
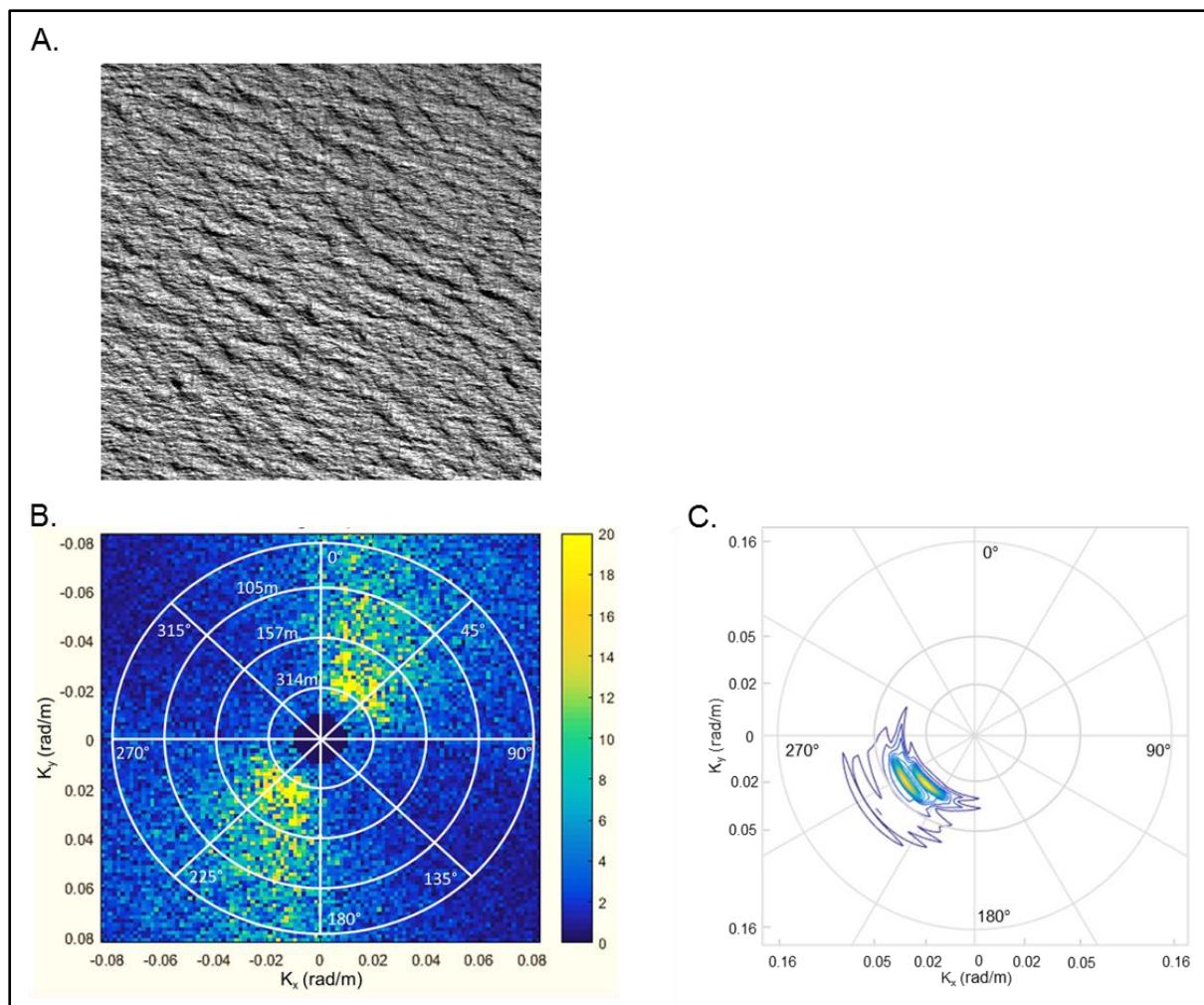
Figure 4.7 Cape Point spectral analysis results. A) RapidEye NIR band subset, B) RapidEye derived directional spectrum and C) Wave buoy derived directional spectrum.

Wind data for Cape Point indicate gusty southerly (180°) winds, ranging in speeds from 3-13 m/s, present 36 hours prior acquisition (Figure 4.8). The wind direction remained constant until six hours prior to acquisition; thereafter, no reliable wind measurements were captured. It is, therefore, difficult to support any observations made about possible wind generated surface features that may have been present at the time of acquisition.
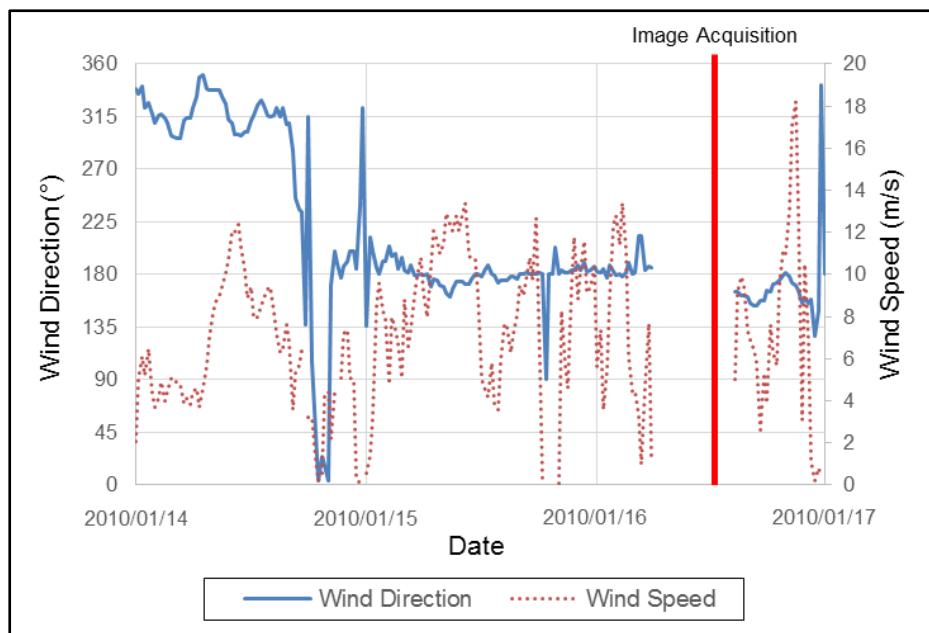
Figure 4.8 Wind speed and direction experienced at Cape Point prior to acquisition.

4.1.3   General discussion on the directional wave spectra

The results above clearly show an agreement between the RapidEye derived directional spectra and the wave buoy derived directional spectra. However, slight visual differences do occur. Many of these differences are not related to the actual characteristic wave parameters present in the imagery but are a result of the approach that has been adopted.

The first and most noticeable difference is that the satellite derived directional spectra exhibit directional ambiguity whereas the wave buoy derived spectra do not. This is expected and is due to the fact that the Fourier transform plots the mirror of the peak across the origin (as stated in Section 2.3.2.1) (Lehar 2010).

Secondly, the directional resolutions differ. Kudryavtsev et al. (2017) reported a higher directional resolution in the satellite (Sentinel-2) derived spectrum than the buoy derived spectrum. A similar trend is observed in the results of this study. The most significant example are the spectra derived for Durban (Figure 4.3). On analysis of these spectra, it was found that the wave buoy derived spectrum (Figure 4.3C) illustrates that waves occurring at the same wavelength, but with potentially different directions, are merged into a single peak with a widely spread directional distribution. In comparison, the RapidEye derived spectrum (Figure 4.3B) produces distinct peaks (i.e. bright dots in the spectrum), each with a single direction and wavelength.

Thirdly, the wave buoys capture data at one point location, whereas the satellite approach in this case analyses data over a 4x4km area. Small spatial variations in characteristic wave parameters are expected due to near-shore wave transformations caused by local bathymetry. However, even though the waves measured vary slightly, the satellite derived directional spectra visually correlate well with the spectra derived from the wave buoys.

4.2 PHASE VELOCITY FIELD RESULTS

The results of the NCC implemented in CIAS consisted of a point shapefile with a single point for each RapidEye pixel. Each point contains feature attributes which include, the direction and distance of movement and the correlation coefficient. The distance attribute allows for the velocity calculation and the correlation coefficient is a value calculated to describe how closely the algorithm has matched the pixels between the two images.

4.2.1 Phase Velocities

Figure 4.9-4.12 display the resulting phase velocity fields calculated by dividing the distance attribute of the CIAS results by the time lag between the acquisition of the blue and red band (3.06 s) of the RapidEye imagery.

It is clearly visible across all four figures that the velocity of the waves decreases as they approach the shore. This is expected and is a result of friction with the seafloor, known as shoaling (Section 2.1.2.1).
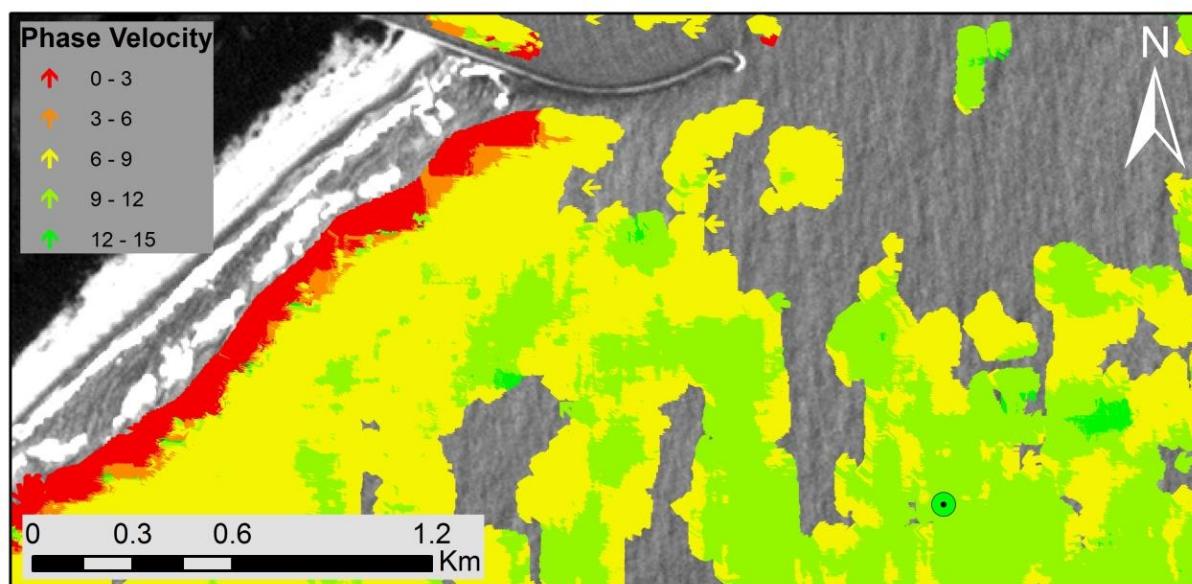
Figure 4.9 Phase velocity (m/s) for Richards Bay.
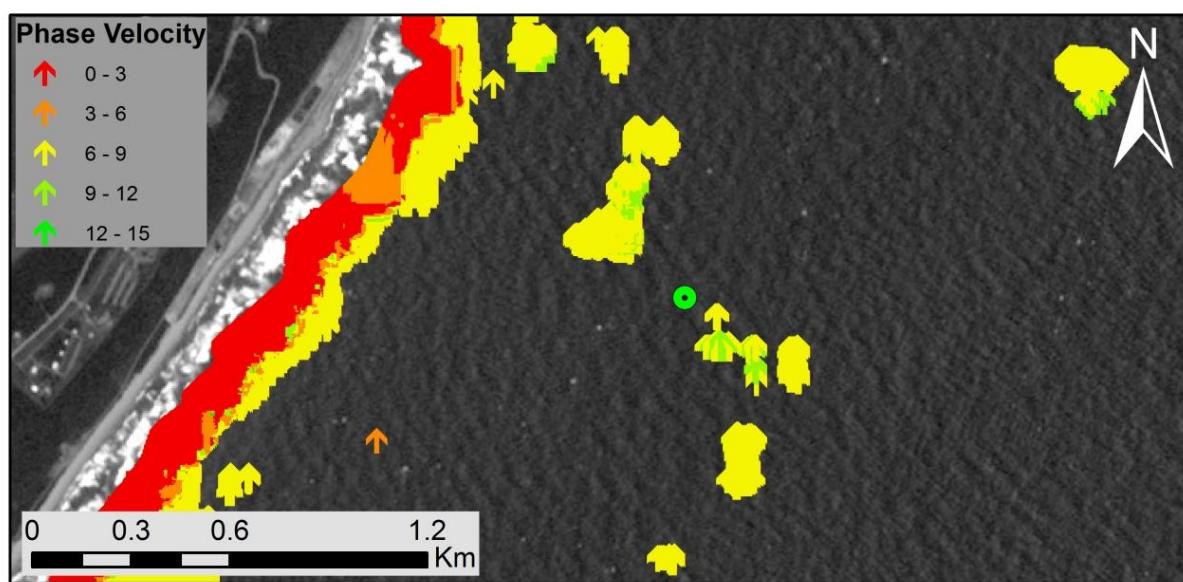
Figure 4.10 Phase velocity (m/s) for Durban.
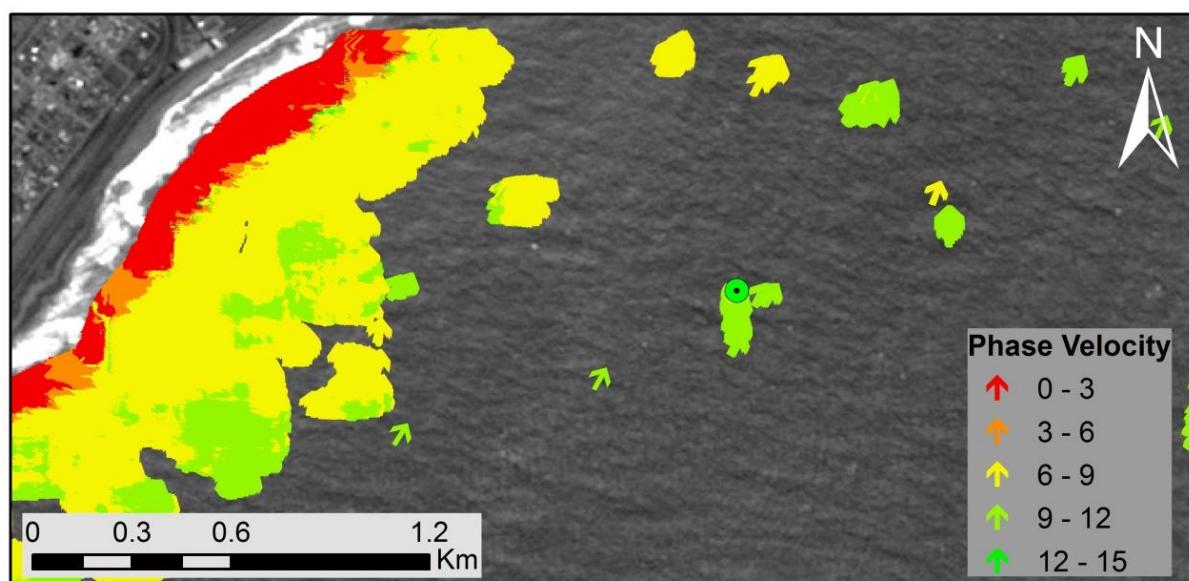
Figure 4.11 Phase velocity (m/s) for East London.
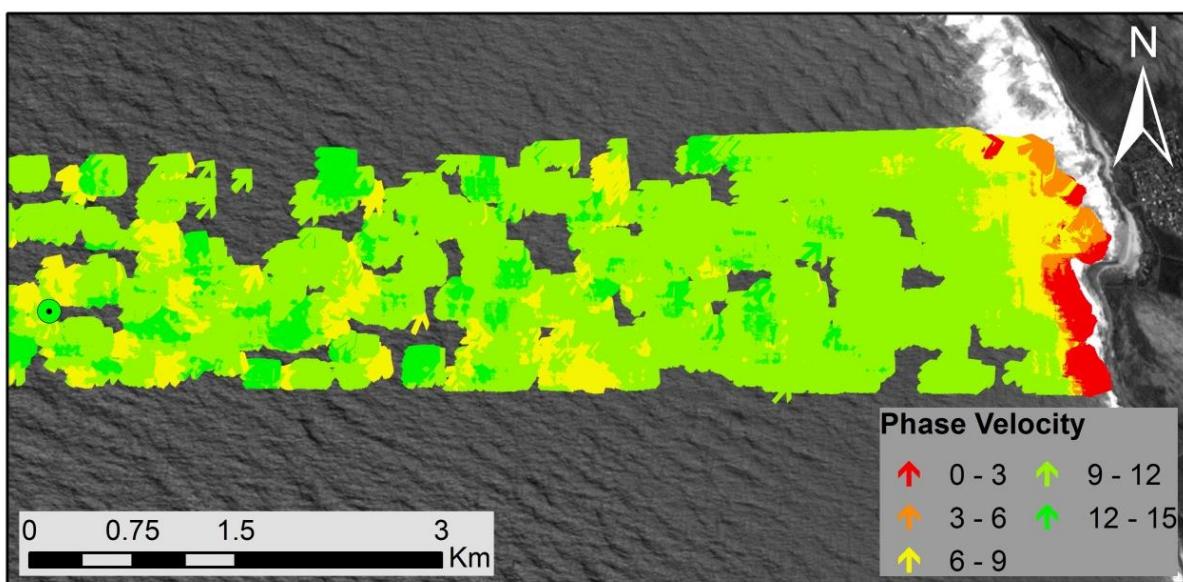
Figure 4.12 Phase velocity (m/s) for Cape Point.

4.2.2   Wave Direction

Figures 4.13-4.16 display the directional results achieved with CIAS for each study area. These figures also display the correlation coefficients calculated for each point.

A trend that is observed across all four study areas is that the correlation coefficients improve closer to the shore line. This is likely due to the near-shore wave transformation phenomenon, known as shoaling (Section 2.1.2.1), which slows the speed of waves and increases the wave heights. The increased wave height results in a higher contrast in brightness between the troughs and crests of the waves near the shore. Due to the fact that the features considered by NCC include brightness and contrast, the ability to accurately match features is these areas would improve.

This can further be supported by visual inspection of the areas that contained points with low correlation coefficients (i.e. areas where displacements have been rejected), as these areas have low levels of contrast between the crests and troughs of waves.
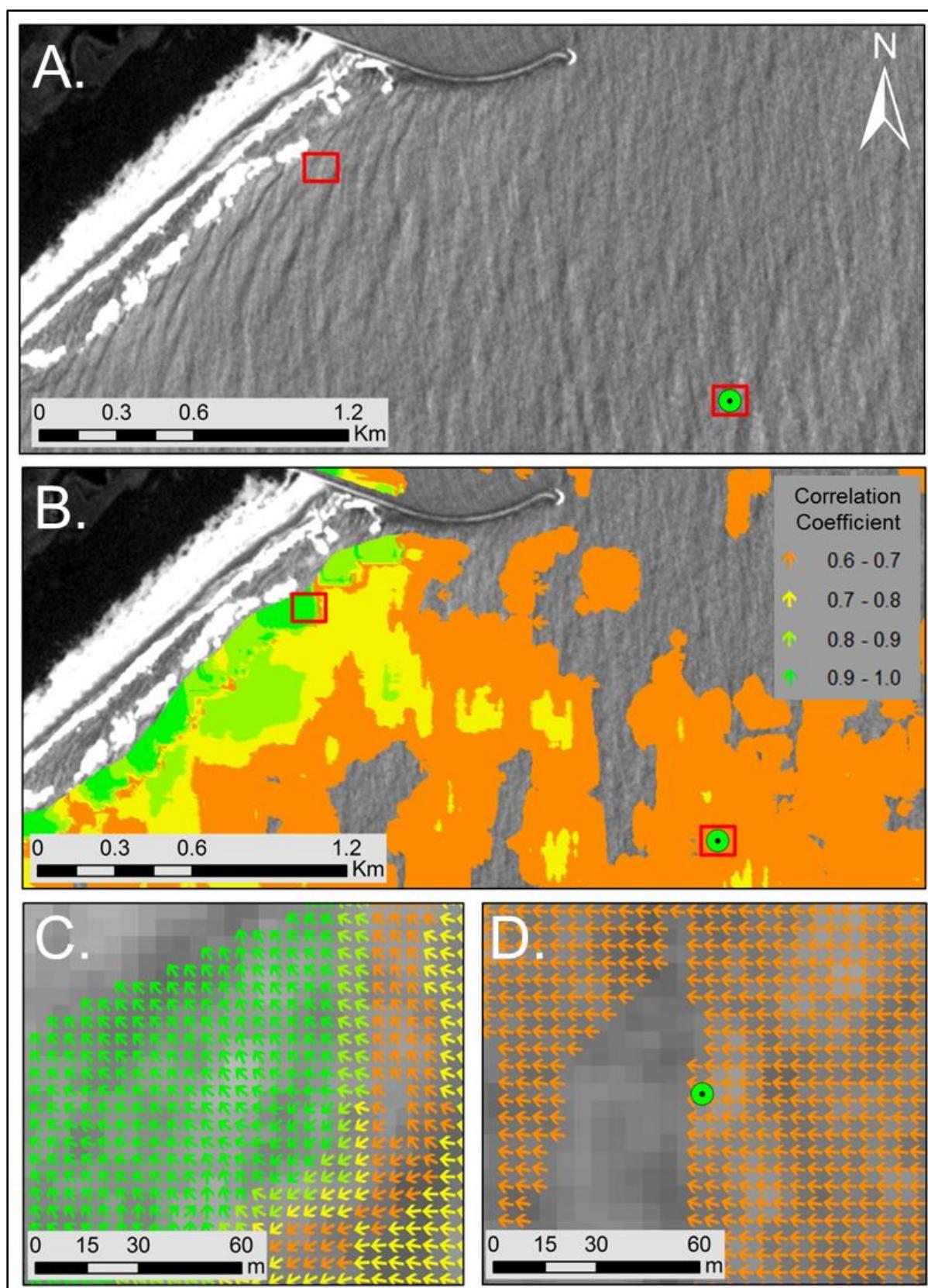
Figure 4.13 Richards Bay wave directional field. A) RapidEye blue band. The location of the wave buoy (green dot) and two subsets (red squares) are illustrated. B) Distribution of correlation coefficients. C) Subset near the shoreline. D) Subset at the wave buoy.
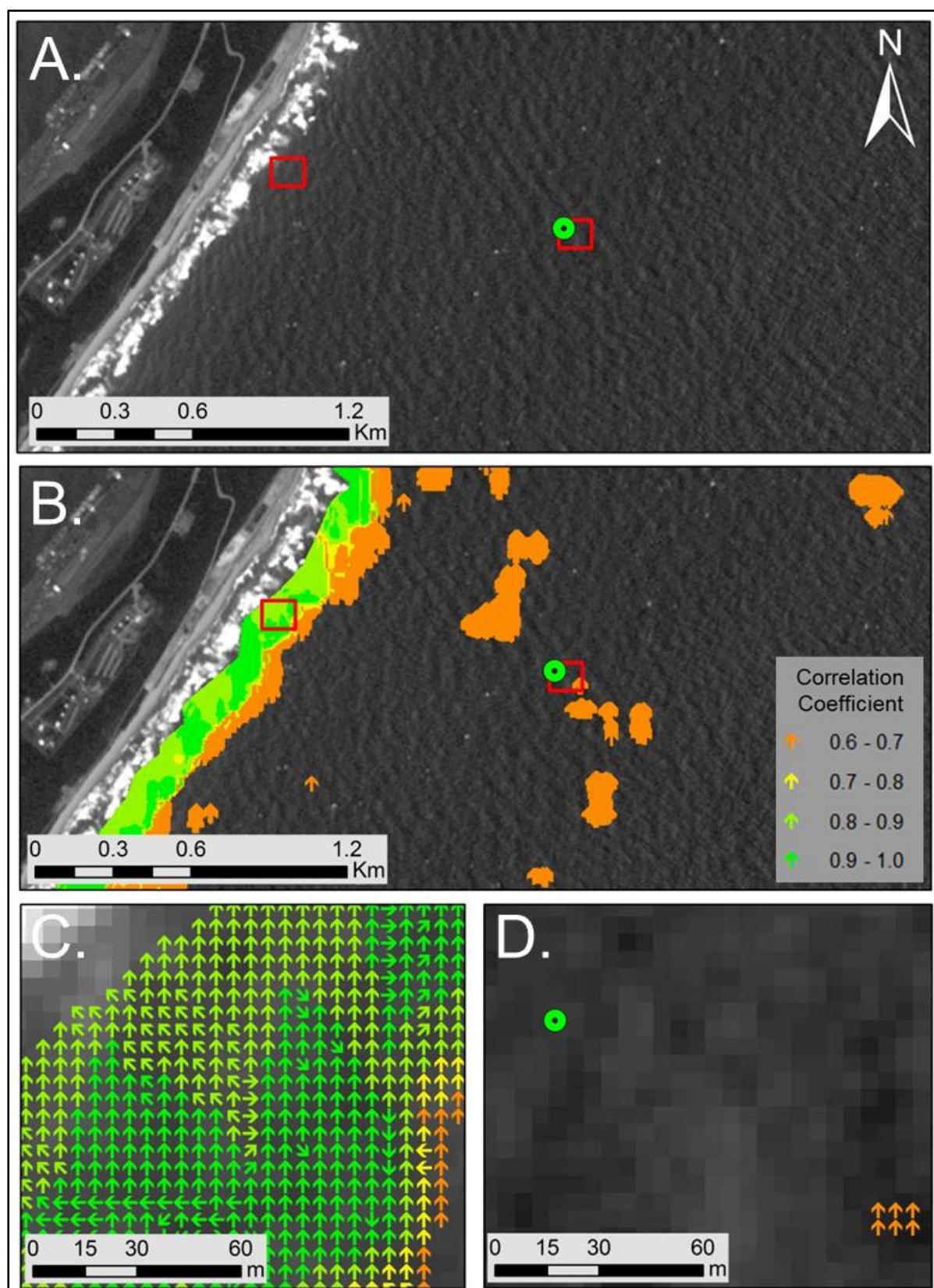
Figure 4.14 Durban wave directional field. A) RapidEye blue band. The location of the wave buoy (green dot) and two subsets (red squares) are illustrated. B) Distribution of correlation coefficients. C) Subset near the shoreline. D) Subset at the wave buoy.
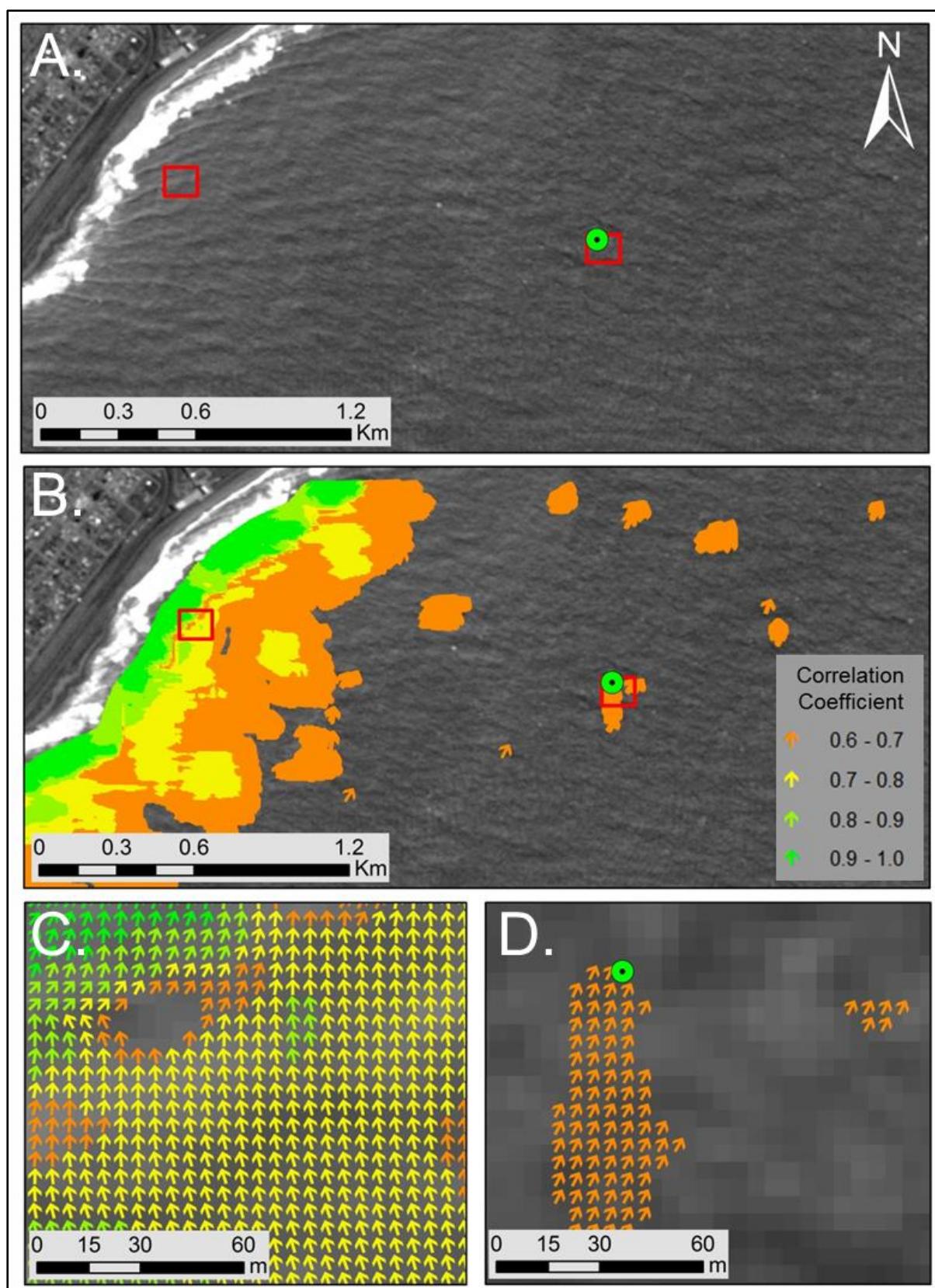
Figure 4.15 East London wave directional field. A) RapidEye blue band. The location of the wave buoy (green dot) and two subsets (red squares) are illustrated. B) Distribution of correlation coefficients. C) Subset near the shoreline. D) Subset at the wave buoy.
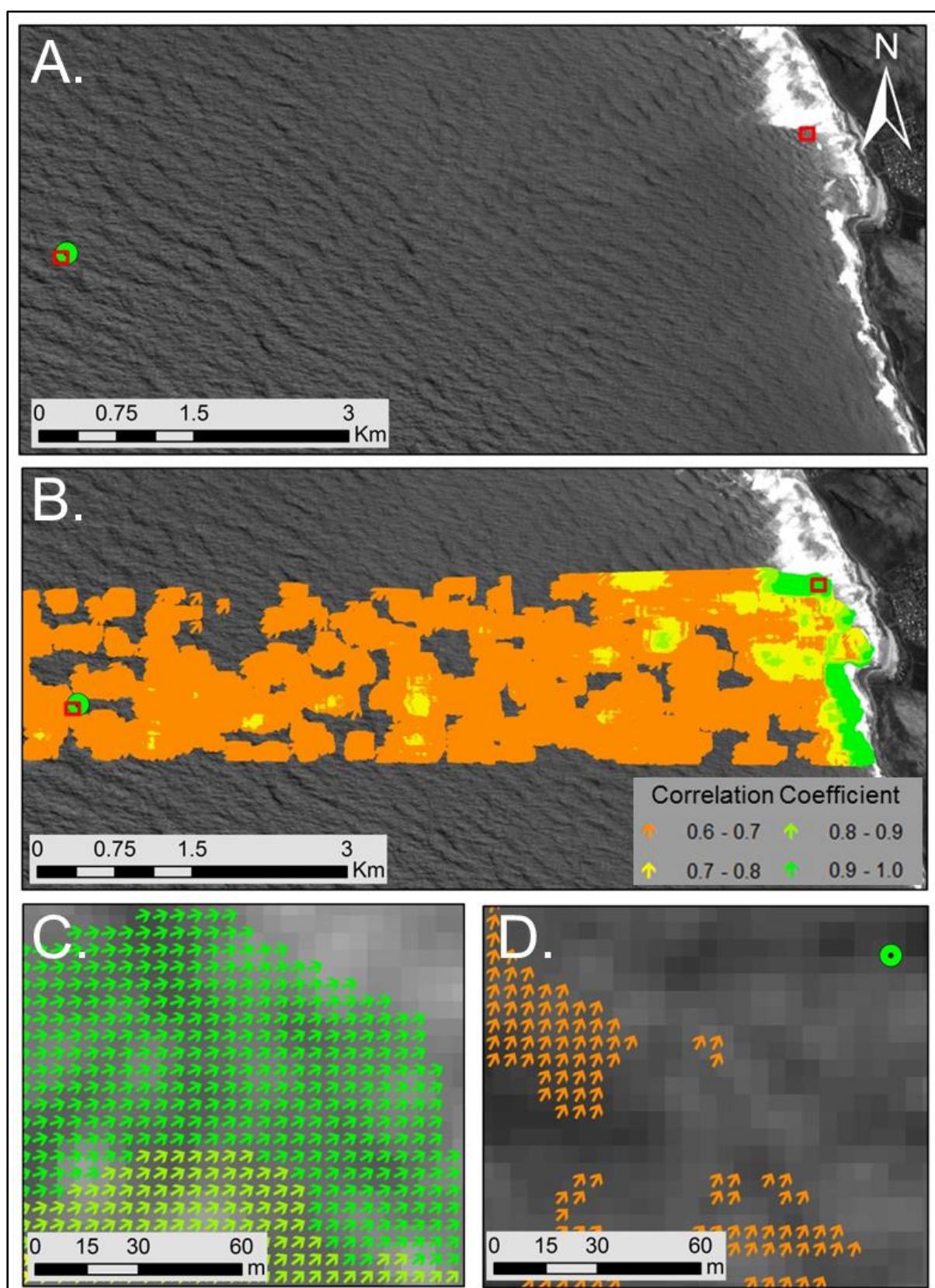
Figure 4.16 Cape Point wave directional field. A) RapidEye blue band. The location of the wave buoy (green dot) and two subsets (red squares) are illustrated. B) Distribution of correlation coefficients. C) Subset near the shoreline. D) Subset at the wave buoy.

The wave directions for the point nearest to the wave buoys were extracted from the directional wave fields and compared to the directions recorded by the wave buoys (Table 4.2). The direction recorded by the buoy is the direction of the peak wave energy for a 30 minute time interval. During this interval, waves may approach from slightly different directions. The buoy, therefore, calculates an additional parameter, known as the directional spreading. This is a measure of the variability in wave direction. The higher this value, the higher the variability of individual wave directions for the 30 minute interval.

Considering that the direction extracted using NCC is the direction of one individual wave, a direct comparison with only the wave buoy direction may be misleading. Therefore the directional spreading has been included in Table 4.2 since the direction extracted from the directional field may differ from the wave buoy but may still fall within the distribution explained by the directional spreading.

Table 4.2 Wave direction extracted from NCC results compared to the wave direction recorded by the wave buoys.

| Study Area | NCC | Wave Buoy | |
	Direction	Direction	Directional spreading
Richards Bay	103°	112°	28.7°
Durban	Rejected	94°	Not recorded
East London	208°	206°	31.8°
Cape Point	208°	227°	12.1°

Richards Bay and East London were both found to be within 10° of the direction measured by the wave buoy, even considering that the directional spreading was relatively high. Cape Point differed from the wave buoy by 19° and therefore did not fall within the directional spreading value. Durban produced the poorest results. Unfortunately, the directional spreading for Durban was not captured by the wave buoy; however, the directional spectrum extracted from the data recorded by the wave buoy (Figure 4.3C) illustrates that waves directions were recorded from 0° all the way around to 240°. This indicates that there could be a variety of wave directions present within each pixel in the RapidEye imagery and is the likely cause of the poor results achieved for Durban using this approach. Under these conditions, it would seem that the NCC approach to monitor the direction and velocity of individual waves fails.

CHAPTER 5:   CONCLUSION

5.1   SYNOPSIS

The research presented in this thesis explored whether optical RapidEye satellite imagery can be used for the retrieval of near-shore ocean wave characteristic parameters. Retrieval of spatially continuous wave characteristic parameters (in contrast to punctual wave buoy measurement points) would contribute to a better understanding of ocean waves and their impact on coastal processes, as well as for improving wave forecasting capabilities. Globally there is an urgent need for spatially continuous wave assessments for improved coastal management and coastal wave forecast capabilities. To date, the use of space-borne multispectral approaches to this end have encountered limited development. In order to overcome this research gap, in this thesis, high resolution RapidEye satellite imagery for four study areas along the coast of South Africa was used and two technical approaches were applied to test the feasibility of the RapidEye sensor for wave characterisation.

The first approach made use of Fast Fourier Transform (FFT) to extract directional wave spectra and associated characteristic parameters. The second approach included normalised cross correlation (NCC) to extract direction and phase velocity fields. Neither of these approaches have been used for this purpose on RapidEye imagery yet, and the two approaches have not been used together in a study for a more comprehensive description of waves. The four study areas included Richards Bay and Durban in the KwaZulu-Natal Province, East London in the Eastern Cape Province and Cape Point in the Western Cape Province. The results were compared to in-situ wave buoy measurements captured by the directional wave buoy located in each study area.

The FFT results reveal a strong visual similarity between the spectra derived from the RapidEye imagery and the spectra derived from the buoy. When compared to characteristic parameters recorded by the wave buoy, Richards Bay produced the most accurate results followed by Durban. In both cases, the peak wave directions were within 10° of the buoy measured direction while the peak wavelength and period were within 10% of the data captured by the wave buoy. As input for coastal wave modelling purposes this accuracy is quite satisfactory. East London produced the poorest results in terms of peak wavelength and direction, differing from the measured wavelength by 17% and the measured wave period by 11.8%. Although Cape Point produced a highly accurate wavelength (0.5% difference) and

an accurate period (3.6% difference), it also produced the poorest result in terms of direction (31° difference).

The results obtained from the NCC for all four study areas revealed similar trends in terms of phase velocities and correlation coefficients. It was observed that near-shore wave shoaling influences the ability of the approach to measure displacements and directions of the individual waves. The resulting directional measurements at the location of the wave buoy were compared with actual measurements of the wave buoys. It was found that Richards Bay and East London produced accurate results at the wave buoy. In both cases, directional differences between the NCC result and the wave buoy were less than 10°. As with the FFT approach, Cape Point produced a less satisfactory result with a directional difference of 19°. For this approach, Durban produced unsatisfactory results (i.e. low correlation coefficients for results around the wave buoy). It is believed that this is due to the fact that waves were approaching from a large variety of directions at the time of acquisition as a result of varying winds present prior to acquisition. Therefore, the NCC algorithm struggled to identify and match waves moving in the peak direction under such variable environmental conditions.

The results of this study indicate that, within a certain range of environmental conditions, characteristic wave parameters can be extracted from RapidEye imagery. The two optical remote sensing approaches implemented do provide spatially continuous wave data reaching sufficient accuracies for potential use in operational ocean state forecast modelling as their provision of spatially extensive information (i.e. measurements at each pixel as opposed to isolated wave buoys) could greatly add to the development and validation of such forecast models as currently under development for the National Oceans and Coasts Information Management System (OCIMS) (https://ocims.dhcp.meraka.csir.co.za/about).

These techniques hold potential as alternatives to existing approaches and are complimentary to other space-borne techniques such as SAR and altimetry.

5.2   LIMITATIONS AND RECOMMENDATION

The main limitation of using remote sensing approaches to derive characteristic wave parameters is associated with the validation of the results. Remote sensing approaches analyse waves in an image that is captured at a single moment in time, but covers a large spatial extent, whereas wave buoys measure waves at a single point location over a period of time. The sparse spatial distributions of the wave buoys along the South African coastline

therefore pose a challenge on the spatial validation of remote sensing results. Therefore, it is recommended that in addition to further development of remote sensing technologies to extract wave characteristic parameters from optical satellite remote sensing data, more effort needs to go into methodologies to reliably verify the derived results. Such possibilities include the deployment of additional wave buoys (or other in-situ wave measurement instruments) within the study areas, the use of study areas elsewhere in the world where ground instrumentation is dense and data sampling frequent, or the use of a computational sea state modelling tool (Chirayath 2016) which could be used to simulate coastal waves with a controlled set of parameters (such as wave height, direction, period etc.). The extraction techniques can then be run on the simulated output and compared to the known input wave parameters.

Further limitations are the presence of cloud cover during image acquisition, as the Earth's surfaces cannot be seen by optical sensors when clouds are present, and the low temporal resolution in comparison to the wave buoys. Nevertheless, the severity of these limitations can be reduced by extending the current methodology to other pushbroom sensors that have multispectral capabilities in order to increase the number of images available and reduce the revisit time (i.e. increasing the temporal resolution). Inclusion of other sensors might also help to overcome another limitation currently preventing the multi-temporal use of RapidEye data (imagery is technically available every 1-2 days) which are the high image acquisition costs.

REFERENCES

Ager TP 2013. An introduction to synthetic aperture radar imaging. *Oceanography* 26(2):20-33.

Apel JR, Byrne HM, Proni & Charnell RL 1975. Observation of oceanic internal and surface waves from the Earth Resources Technology Satellite. *Journal of Geophysical Research* 80: 865-881.

Ardhuin, F, Collard F & Chapron B 2004. *Wave spectra from ENVISAT's Synthetic Aperture Radar in coastal areas*. Proceedings of the 14th International Offshore and Polar Engineering Conference held 23-28 May 2004, Toulon, France.

Beal RC, Tilley DG & Monaldo FM 1983. Large and small scale spatial evolution of digitally processed ocean wave spectra from SEASAT Synthetic Aperture Radar. *Journal of Geophysical Research* 88: 1761–1778.

Beatley T 2009. *Planning for coastal resilience: Best practices for calamitous Times*. Washington: Island Press.

Beltaos S & Kääb A 2014. Estimating river discharge during ice breakup from near simultaneous satellite imagery. *Cold Regions Science and Technology* 98: 35-46.

Bosboom J & Stive MJF 2013. *Coastal Engineering 1*. Version 0.4. Delft: Delft Academic Press.

Brown LG 1992. A survey of image registration techniques. *Computing Surveys* 24: 325-376.

Brown E, Colling A, Park D, Phillips J, Rotherly D & Wright J 2005. *Waves, tides and shallow-water processes*. 2nd ed. Oxford: Butterworth-Heinemann.

Campbell JB 2007. *Introduction to Remote Sensing.* 4th ed. London: The Guilford Press.

Chirayath V 2016. Fluid lensing and applications to remote sensing of aquatic environments. Doctoral dissertation. Stanford: Stanford University, Department of Aeronautics and Astronautics.

CIA 2014. The world fact book: South Africa [online]. Available from: https://www.cia.gov/library/publications/the-world-factbook/geos/sf.html. [Accessed 13 April 2016].

Collard F, Ardhuin F & Chapron B 2005a. Extraction of coastal ocean wave fields from SAR images. *IEEE Journal of Oceanic Engineering* 110: 526-533.

Collard F, Ardhuin F & Chapron B 2005b. Direct measurements of ocean surface velocity from space: Interpretation and validation. *Journal of Geophysical Research* 30: C07008.

Collard F, Ardhuin F & Kerbaol V 2004. *Satellite Synthetic Aperture Radar sea surface Doppler measurements*. Proceedings of the 2nd workshop on Coastal and Marine Applications of Synthetic Aperture Radar held 8-12 September, Svalbard, Norway. Paris: European Space Agency.

COMET MetEd. 2006. Shallow water waves [online]. Available at: http://stream1.cmatc.cn/pub/comet/CoastalWeather/sww/comet/marine/SWW/print.htm#a23 [Accessed 17 May 2016].

Corbella S & Stretch DD 2012. The wave climate on the KwaZulu-Natal coast of South Africa. *Journal of the South African Institution of Civil Engineering* 54(2): 45-54.

Cox C & Munk W 1954. Measurement of the roughness of the sea surface from photographs of the Sun's glitter. *Journal of the Optical Society of America* 44: 838–850.

Crocker RI, Matthews DK, Emery WJ & Bladwin DG 2007. Computing coastal ocean surface currents from infrared and ocean colour satellite imagery. *IEEE Transactions on Geoscience and Remote sensing* 45(2): 435-447.

Danilo C & Melgani F 2016. Wave period and coastal bathymetry using wave propagation on optical images. *IEEE Transactions on Geoscience and Remote Sensing* 54: 6307-6319.

Davidson-Arnott R 2010. *Introduction to coastal processes and geomorphology*. New York: Cambridge University Press.

De Michele M, Leprince S, Thiebot J, Raucoules D & Binet R 2012. Direct measurement of ocean waves velocity field from a single SPOT-5 dataset. *Remote Sensing of Environment* 119:266-271.

Dugan JP, Suzukawa HH, Forsyth CP & Faber MS 1996. Ocean wave dispersion surface measured with airborne IR imaging systems. *IEEE Transactions on Geoscience and Remote Sensing* 14(5): 1282–1284.

Dugan JP, Piotrowski CC & Williams ZJ 2001. Water depth and surface current retrievals from airborne optical measurements of surface gravity wave dispersion. *Journal of Geophysical Research* 106: 16903–16915.

Element Consulting Engineers 2014. Mouille Point Precinct One: Upgrade of Promenade. Coastal Dynamics Assessment [online]. Cape Town: City of Cape Town. Available from: http://www.sefsa.net/wp-content/uploads/2014/07/13193-Mouille-Point-Coastal-Study_Rev1-31Jan2014.pdf [Accessed 12 April 2017].

Emery WJ, Thomas AC, Collins MJ, Crawford WR & Mackas DL 1986. An objective method for computing advective surface velocities from sequential infrared satellite images. *Journal of Geophysical Research* 91(C11): 12 865–12 878.

ESA 2017. Sentinel 3 altimetry: Coastal zones [online]. Available from: https://earth.esa.int/web/sentinel/user-guides/sentinel-3-altimetry/applications/coastal-zones [Accessed 6 June 2017].

ESA & CNES 2017. Radar altimetry: Tutorial and toolbox [online]. Available from: https://www.altimetry.info/ [Accessed 6 June 2017].

Fu LL & Cazenave A (eds) 2001. *Satellite altimetry and earth sciences: A handbook of techniques and applications*. San Diego: Academic Press.

Gabler RE, Petersen JF, Trapasso LM & Sack D 2009. *Physical Geography*. 9th ed. Belmont: Brooks Cole.

Gade M 2015. *Synthetic aperture radar applications in coastal waters.* Proceedings of the 12th International Conference on the Mediterranean Coastal Environment MEDCOAST held 6-10 October 2015, Varna, Bulgaria.

Garcia CAE & Robinson IS 1989. Sea surface velocities in shallow seas extracted from sequential coastal zone colour scanner satellite data. *Journal of Geophysical Research* 94(C9): 12 681–12 692.

Gelpi CG, Schuraytz BC & Husman ME 2001. Ocean wave height spectra computed from high-altitude, optical, infrared images. *Journal of Geophysical Research* 106: 31403-31413.

Goble BJ & Mackay CF 2013. Developing risk set-back lines for coastal protection using shoreline change and climate variability factors. (Special Issue) *Journal of Coastal Research* 65: 2125-2130.

Goda Y 2000. *Random seas and design of maritime structures*. 2nd ed. Singapore: World Scientific.

Hauser D, Kahma KK, Krogstad HE, Lehner S, Monbaliu JAJ & Wyatt LR (eds) 2005. *Measuring and Analysing the Directional Spectra of Ocean Waves*. COST Action 714. Luxembourg: EU Publications Office.

Heydorn AEF & Tinley KL 1980. *Estuaries of the Cape, part1: Synopsis of the Cape Coast-Natural features, dynamics and utilization*. Research Report No 380. Stellenbosch: Council for Scientific and Industrial Research.

Holthuijesen LH 2007. *Waves in Oceanic and Coastal waters*. New York: Cambridge University Press.

Hu C, Li X, Pichel WG & Muller-Karger FE 2009. Detection of natural oil slicks in the NW Gulf of Mexico using MODIS imagery. *Geophysical Research Letters* 36: L01604.

Jackson C 2007. Internal wave detection using the Moderate Resolution Imaging Spectroradiometer (MODIS). *Journal of Geophysical Research* 112: C11012.

Janssen P 2004. *The Interaction of Ocean Waves and Wind*. Cambridge: Cambridge University Press.

Johannessen JA 2000. Coastal observing systems: The role of synthetic aperture radar. *Johns Hopkins APL Technical Digest* 21: 41-48.

Johannessen JA, Chapron B, Collard F, Kudryavtsev V, Mouche A, Akimov D & Dagestad KF 2008. Direct ocean surface velocity measurements from space: Improved quantitative interpretation of Envisat ASAR observations. *Geophysical Research Letters* 35: L22608.

Joubert, J & van Niekerk J 2013. South African Wave Energy Resource Data [online]. Stellenbosch: Centre for Renewable and Sustainable Energy Studies. Available from: http://www.crses.sun.ac.za/files/research/publications/technical-reports/SANEDI(WaveEnergyResource)_edited_v2.pdf [Accessed 20 April 2017].

Kääb A & Prowse T 2011. Cold-regions river flow observed from space. *Geophysical Research Letters* 38: L08403.

Kääb A, Lamare M & Abrams M 2013. River ice flux and water velocities along a 600 km-long reach of Lena River, Siberia, from satellite stereo. *Hydrology and Earth System Sciences* 17: 4671-4683.

Kääb A & Vollmer M 2000. Surface geometry, thickness changes and flow fields on creeping mountain permafrost: Automatic extraction by digital image analysis. *Permafrost and Periglacial Processes* 11: 315-326.

Krauß T, Stätter R, Philipp R & Bräuninger S 2013. *Traffic flow estimation from single satellite*. Proceedings of the Sensors and Models in Photogrammetry and Remote Sensing (SMPR) conference held 5-8 October 2013, Tehran, Iran.

Kudryavtsev V, Myasoedov A, Chapron B, Johannessen J & Collard F 2012a. Joint sun-glitter and radar imagery of surface slicks. *Remote Sensing of Environment* 120: 123-132.

Kudryavtsev V, Myasoedov A, Chapron B, Johannessen J & Collard F 2012b. Imaging meso-scale upper ocean dynamics using SAR and optical data. *Journal of Geophysical Research* 117: C04029.

Kudryavtsev V, Yurovskaya M, Chapron B, Collard F & Donlon C 2017. Sun glitter imagery of ocean waves. Part 1: Directional spectrum retrieval and validation. *Journal of Geophysical Research: Oceans* 122:1369-1383.

Kulkarni SR 2002. ELE201 Introduction to electrical signals and systems. Course material. Spring semester 2002. Princeton University.

Kuo YY, Leu LG & Kao IL 1999. Directional spectrum analysis and statistics obtained from ERS-1 SAR wave images. *Ocean Engineering* 26: 1125-1144.

Lehar S 2010. An intuitive explanation of Fourier theory [online]. Available from: http://cns-alumni.bu.edu/~slehar/fourier/fourier.html [Accessed 07 February 2017].

Leprince S, Barbot S, Ayoub F & Avouac JP 2007. Automatic and precise orthorectification, co-registration, and subpixel correlation of satellite images, application to ground deformation measurements. *IEEE Transactions on Geoscience and Remote Sensing* 45 (6): 1529-1558.

Lewis JP 1995. Fast normalized cross-correlation. *Vision interface* 10: 120-123.

Lubke RA 1998. The coastal environment. In Lubke RA & De Moor I (eds) *Field guide to the eastern and southern cape coasts*, 3-9. Cape Town: University of Cape Town Press.

Luck-Vogel M 2016. Recent developments in remote sensing for coastal and marine applications. In Barthlett D & Celliers L (eds). *Geoinformatics for coastal and marine management*, 73-96. Boca Raton: CRC Press.

Lyzenga DR 1987. The physical basis for estimating wave energy spectra from SAR imagery. *Johns Hopkins Applied Physics Laboratory Technical Digest* 8:65-59.

Marchand M (ed) 2010. *Concepts and Science for Coastal Erosion Management: Concise report for policy makers*. Delft: Deltares.

Mather AA 2010. *Stormy sea ahead: Planning for sea level rise*. Proceedings of the South African planning institute conference held 18-21 April 2010, Durban, South Africa.

MATLAB 2016a. fft: Fast Fourier transform algorithm. Help menu. MATLAB version 9.0 (R2016a).

MATLAB 2016b. fft2: 2D fast Fourier transform algorithm. Help menu. MATLAB version 9.0 (R2016a).

Matthews JP & Awaji T 2010. Synoptic mapping of internal-wave motions and surface currents near the Lombok Strait using the Along-Track Stereo Sun Glitter technique. *Remote Sensing of Environment* 114: 1765-1776.

McCormick ME 2007. *Ocean wave energy conversion*. Mineola: Dover Publications.

Mobley CD 1994. Light and water: Radiative transfer in natural waters. San Diego: Academic Press.

Mouton J 2004. *How to succeed in your master's and doctoral studies: A South African guide and resource book*. 6th impression. Pretoria: Van Schaik Publishers.

Palmer BJ, van der Elst R, Mackay F, Mather AA, Smith AM, Bundy SC, Thackeray Z, Leuci R & Parak O 2011. Preliminary coastal vulnerability assessment for KwaZulu-Natal, South Africa. *Journal of Coastal Research* 64: 1390-1395.

Piotrowski CC & Dugan JP 2002. Accuracy of bathymetry and current retrieval from airborne optical time-series imaging of shoaling waves. *IEEE Transactions on Geoscience and Remote Sensing* 40: 2606-2618.

Plummer CC, McGeary D & Carlson DH 1999. *Physical Geology*. Boston: McGraw-Hill.

Populus J, Aristaghes C, Jonsson JL, Augustin JM & Pouliquen E 1991. The use of SPOT data for wave analysis. *Remote Sensing of Environment* 36: 55–65.

RapidEye 2016. RapidEye imagery product specifications [online]. Available from: https://www.planet.com/products/satellite-imagery/files/160625-RapidEye%20Image-Product-Specifications.pdf [Accessed 06 March 2016].

Rascle N, Chapron B, Ponte A, Ardhuin F & Klein P 2014. Surface roughness imaging of currents shows divergence and strain in the wind direction. *Journal of Physical Oceanography* 44: 2153–2163.

Reeve D, Chadwick A & Fleming C 2004. *Coastal Engineering: Processes, theory and design practice*. London: Spon Press.

Reinartz P, Lachaise M, Schmeer E, Krauss T & Runge H 2006. Traffic monitoring with serial images from airborne cameras. *ISPRS Journal of Photogrammetry and Remote Sensing* 61: 149-158.

Rogers WE, Hwang PA & Wang DW 2003. Investigation of wave growth and decay in the SWAN model: Three regional-scale applications. *Journal of Physical Oceanography* 33: 366–389.

Rossouw J 1984. *Review of existing wave data, wave climate and design waves for South African and South West African (Namibian) coastal waters.* Report No T/SEA 8401. Stellenbosch: CSIR.

Rossouw M & Theron AK 2009. *Aspects of potential climate change impacts on ports and maritime operations around the southern African coast*. Proceedings of the 28th Southern African Transport Conference held 6-9 July 2009, Pretoria, South Africa.

Rossouw M, Terblanche L & Moes, J 2013. General characteristics of long waves around the South African Coast [online]. Stellenbosch: CSIR. Available from: http://researchspace.csir.co.za/dspace/handle/10204/7511 [Accessed 20 April 2017].

Shao W, Zhang Z, Li X & Li H 2016. Ocean wave retrieval from Sentinel-1 SAR imagery. *Remote Sensing* 8(9): 707.

Smith AM, Mather AA, Bundy SC, Cooper JAG, Guastella LA, Ramsay PJ & Theron A. (2010). Contrasting styles of swell-driven coastal erosion: examples from KwaZulu-Natal, South Africa. *Geological Magazine* 147: 940-953.

Smith A, Guastella LA, Mather AA, Bundy SC & Haigh ID 2013. KwaZulu-Natal coastal erosion events of 2006/2007 and 2011: A predictive tool? *South African Journal of Science* 109 (3/4): 72-75.

South Africa (Republic of) 2004. *Operational policy for the disposal of land-derived water containing waste to the marine environment of South Africa*. Pretoria: Department of Water Affairs and Forestry.

Statistics South Africa 2001. *Census 2001*. Pretoria: Statistics South Africa.

Stilwell D 1969. Directional energy spectra of the sea from photographs. *Journal of Geophysical Research* 74: 1974–1986.

Stone AW, Weaver AVB & West WO 1998. Climate and weather. In Lubke RA & De Moor I (eds) *Field guide to the eastern and southern cape coasts*, 41-49. Cape Town: University of Cape Town Press.

Stopa J, Ardhuin F, Bababin A & Zieger S 2016. Comparison and validation of physical wave parameterizations in spectral wave models. *Ocean Modelling* 103: 2-17.

Sundar V 2016. *Ocean wave mechanics*. Chichester: John Wiley & Sons Ltd.

Takasaki K, Sugimura T & Tanaka S 1993. *Speed vector measurement of moving objects using JERS-1 OPS data.* Proceedings from the IEEE International Geoscience and Remote Sensing Symposium held 18-21 August 1993, Tokyo, Japan.

Theron AK 2004. Sediment Transport Regime at East London. Master's Thesis. Stellenbosch: Stellenbosch University, Department of Civil Engineering.

Theron A 2016. Methods for determination of coastal development setback lines in South Africa. Doctoral dissertation. Stellenbosch: Stellenbosch University, Department of Civil Engineering.

Tinley KL 1985. *Coastal Dunes of South Africa*. South African National Science Programme report 109. Pretoria: FRD-CSIR.

Transnet National Ports Authority 2010. TPNA: Our Ports [online]. Available from: https://www.transnetnationalportsauthority.net/OurPorts/Pages/default.aspx. [Accessed 6 July 2017].

U.S. Army Corps of Engineers 2008. Coastal engineering manual part II: Coastal Hydrodynamics [online]. Available from: http://www.marine.tmd.go.th/Part-II-Chap1.pdf [Accessed 07 March 2017].

Van der Merwe C 2017. A synthesis of the coastal geophysical characteristics of sandy beaches along the South African coastline. Master's Thesis. Stellenbosch: Stellenbosch University, Department of Civil Engineering.

Vignudelli S, Berry P & Roblou L 2008. Satellite altimetry near coasts - current practices and a look at the future. In Benveniste J & Menard Y (eds) *15 Years of Progress in Radar Altimetry*. Paris: European Space Agency.

WaveNet 2016. WaveNet: The online real time waves and weather of South Africa [online]. Available from: http://wavenet.csir.co.za/OnlineData/RealtimeData.htm [Accessed 04 April 2016].

Woodroffe CD 2003. *Coasts: Form, process and evolution*. Cambridge: Cambridge University Press.

Zitova B & Flusser J 2003. Image registration methods: a survey. *Image and Vision Computing* 21: 977-1000.

APPENDICES

APPENDIX A

MATLAB scripts used to calculate the directional spectrum from the wave buoy data, as per Section 3.4.

```matlab
%%% Read in file
dirSpec = csvread('Name.csv'); % select your input data

%%% Transpose matrix
dirSpec = dirSpec';


%%% Magnetic north correction (i.e. top rows to be shifted to bottom)
magnetic_declination = 23; % change depending on location
dirSpec(length(dirSpec(:,1))+1:length(dirSpec(:,1))+
magnetic_declination,:) = dirSpec(1: magnetic_declination,:);
dirSpec(1: magnetic_declination,:) = [];


%%% Creates an index of frequency intervals
frequency_end_value = 118*.005;
frequency_start_value = .005;
freq = linspace(frequency_start_value,frequency_end_value,118);

%%% Plot data
PolarContour(dirSpec,freq);
title('directional spectrum')
```

APPENDIX B

MATLAB script used to extract the directional spectrum, peak direction, wavelength and period from the RapidEye imagery, as per Section 3.5.1.

```matlab
%%% Read in input image
img = imread('Image.tif'); % select your input image
% img = img(:,:,1); % only include this if the input image is a .png
resizedim = 1;

% removes 1 pixel around edges as precautionary measure for noise
img = img(1+resizedim:end-resizedim,1+resizedim:end-resizedim);

% make image odd in size for computational purposes
if mod(length(img(:,1)),2) == 0
    img = img(1:end-1,:);
end

if mod(length(img(1,:)),2) == 0
    img = img(:,1:end-1);
end

xdim = length(img(1,:));
ydim = length(img(:,1));


%%% Perform 2D FFT
bright = abs(fftshift(fft2(img)));  % fft2() Fourier transforms the matrix
                                    % fftshift() centres the lowest
                                      frequency components (outside corners
                                      are flipped to centre)
                                    % abs() absolute value of the matrix
                                      (makes all values real)


%%% Normalise the 2D FFT by number of elements in array
normbright = [];

for j=1:xdim
    for i=1:ydim
        normbright(i,j) = bright(i,j)./ (numel(bright));
    end
end


%%% Define the new axis (for Fourier transform)
sample = 5; % raster pixel size in meters
makexax = linspace(-1.*pi./sample,1.*pi./sample,xdim); % wave number axes
makeyax = linspace(-1.*pi./sample,1.*pi./sample,ydim);


%%% Filter out false spectral peaks (around the centre)
for xindex= 1:xdim
    for yindex = 1:ydim
        if (makexax(xindex) <= .01) && (makexax(xindex) >= -.01) &&
(makeyax(yindex) <= .01) && (makeyax(yindex) >= -0.01)
```

```matlab
%              in centre box
            if sqrt(makexax(xindex).^2 + makeyax(yindex).^2) <= 0.01
%                disp('in here')
                normbright(yindex,xindex)=0;
            end
        end
    end
end
```

```matlab
%%% Plot directional spectrum
% set the normalised brightness spectrum colour bar
colourbaraxismax = 1; % change based on output
colourbaraxismin = 0;

figure
imagesc(makexax,makeyax,normbright)
title('normalized brightness spectrum masked')
colorbar
caxis([colourbaraxismin colourbaraxismax])
```

```matlab
%%% Locate the spectral peak
norm_bright_max=max(normbright(:));
max_location=find(normbright==norm_bright_max);
[R,C]=ind2sub(size(normbright),max_location);
kxm=makexax(C);
kym=makeyax(R);
```

```matlab
%%% Calculate peak wavelength
wavelength=(2.*pi)./(sqrt(kxm.^2+kym.^2))
```

```matlab
%%% Calculate peak direction
direction=atan((kym)./(kxm));
direction_degrees=radtodeg(direction)
```

```matlab
%%% Calculate peak period
depth = 30; % change this to the average depth (in meters) of the area or
depth of the wave buoy
k=sqrt((kym.*kym)+(kxm.*kxm));
w=sqrt(9.81.*k.*tanh(depth.*k));
Period= (2.*pi)./w
```